Coherent Synchrotron Radiation and Microwave Instability in Electron Storage Rings

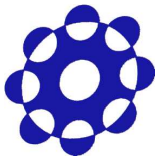

Demin Zhou

Department of Accelerator Science
School of High Energy Accelerator Science
The Graduate University for Advanced Studies

A thesis submitted for the degree of

Doctor of Philosophy

September 2011

Abstract

This thesis work was dedicated to investigating coherent synchrotron radiation (CSR) and microwave instability (MWI) in electron rings. CSR is an important issue in modern electron/positron storage rings, where short bunch length and/or low emittance are usually desired for particle physics or to produce light.

To better understand the physics of CSR, we developed a new code, CSRZ, for calculating CSR impedance for an arbitrarily curved chamber. The chamber has rectangular cross section. The CSR impedance can be calculated with boundary conditions of perfectly conducting walls or resistive walls. With low-level numerical noises and minimal numerical damping, the code is well suitable for the task of calculating CSR impedance in a series of bending magnets. With a tiny approximation on the geometry of the chamber, which was assumed to be wiggling in the code, CSRZ can also be used to calculate the longitudinal impedance due to coherent radiation in a wiggler (CWR). Therefore, CSRZ does fulfill another mission of calculating the CWR impedance in the wiggler sections of KEKB and SuperKEKB.

An analytic eigenfunction expansion method was available to calculate the longitudinal impedance due to CWR with rectangular chamber. The method used dyadic Green's functions in electromagnetic theory and was rigorous for the case of straight chamber. Substantial alterations were performed in order to make it applicable to calculate the imaginary part of CWR impedance related to the beam self-fields. Therefore we re-derived the theory and did find the full expressions for CWR impedance. With shielding of chamber, the CWR impedance indicates resonant properties which were not seen in the theory for

CWR in free space. The analytic work also provides excellent benchmarking to the CSRZ code.

The last part of this thesis addresses microwave instability (MWI) in the KEKB low energy ring (LER) and the SuperKEKB positron damping ring (DR). Code development for simulating MWI was discussed first. For the KEKB LER, the impedances of various components, including CSR, were collected and used to survey the MWI. The CSR instability in the SuperKEKB DR was studied using existing theories of instability analysis.

This thesis is dedicated to my family, especially ...

to my parents for bringing me to this world and for always encouraging me to follow my dreams,

to my wife, Mingyu Han, for her love, unlimited support and understanding.

Acknowledgements

This thesis would not have been possible without the support of many people. I would like to take this opportunity to thank all who supported, commented and encouraged me during my thesis period.

First and foremost, I would like to sincerely express my gratitude and appreciation to my thesis advisor, Prof. Kazuhito Ohmi, who has provided continuous support and guidance throughout my doctoral study. I am always indebted to his constant trust and wonderful advice with full of wisdom. It is only with his patient encouragement that I was able to enjoy carrying out investigations in the field of accelerator physics. Meanwhile, many of his values in life have influenced my ways of thinking, being and doing. His consistent help enabled me to enjoy the life in Japan as a foreigner.

I would like to thank the members of my thesis committee, Prof. Yong Ho Chin, Prof. Ryoichi Hajima, Prof. Susumu Kamada, Prof. Norio Nakamura, and Prof. Kaoru Yokoya, for their careful reviews, as well as valuable comments and suggestions for improvement of my dissertation. In particular, Yong Ho's collaboration was essential to achieving the breakthrough in the work of coherent wiggler radiation (CWR). Enlightening discussions with Kaoru have been invaluable to clarify my ideas and to improve my work on coherent synchrotron radiation (CSR).

At KEK, I have had the privilege of working with many talented professionals, who have made contributions to my research experience. My sincere thanks go to Prof. Katsunobu Oide, for his untiring support and collaboration. His visionary ideas and invaluable insights have been a constant source of inspiration to me. The help from

Tomonori Agoh is deeply appreciated. His doctoral thesis and published papers set an excellent starting point for my work on CSR. I would like to thank the members of KEKB commissioning group, Tetsuo Abe, Kazunori Akai, John Flanagan, Hitoshi Fukuma, Takao Ieiri, Naoko Iida, Hitomi Ikeda, Mitsuo Kikuchi, Haruyo Koiso, Miko Masuzawa, Toshihiro Mimashi, Yukiyoshi Ohnishi, Yuji Seimiya, Kyo Shibata, Yusuke Suetsugu, Masafumi Tawada, Makoto Tobiyama, Mitsuhiro Yoshida, and others, for their collaboration on many of my subjects and useful discussions. Also, with many of them, I have enjoyed the collaboration on badminton and ping-pong games. I am grateful to Kohji Hirata and Etienne Forest for giving lectures to me on accelerator physics. Particularly, I would like to thank Yusuke Aizawa, Shigeo Hasegawa, Misa Miyai and Noriko Omura of the SOKENDAI office at KEK for their consistent support.

My special thanks are due to Dr. Yunhai Cai, Dr. Gennady Stupakov, Prof. Alex Chao from SLAC and Dr. Mikhail Zobov from INFN. Their insightful comments at various stages of my research have been very valuable. It was Yunhai who first introduced me to study microwave instability when he visited KEK in the end of 2008. Since then, he has patiently given me innumerable hours of his time and attention, whenever we met each other, to discuss my work. He also generously hosted my several visits to SLAC. Gennady's collaboration has made it possible for me to execute my research on both CSR and CWR smoothly. I am extremely thankful to Alex for his kind help and valuable advices towards developing my scientific career. Mikhail has always been interested in my work and has been willing to lend his insight and expertise.

I could not omit to thank my master thesis advisor, Prof. Jiuqing Wang, to whom I have always been grateful for introducing me to the field of accelerator physics. He also has had a key role in shaping my own thinking about academic life. I would like to acknowledge the numerous individuals, Prof. Jie Gao, Prof. Qing Qin, Prof. Jingyu

Tang, Prof. Shuhong Wang, Prof. Guoxi Pei, Prof. Gang Xu, and others, who have also directly or indirectly affected my scientific career at IHEP, Beijing.

Many of my friends are deserving of acknowledgements for their help and encouragement: Yuan Chen, Lihong Cheng, Changdong Deng, Yuantao Ding, Xiaowei Dong, Zheqiao Geng, Qingkai Huo, Yudong Liu, Puneet Jain, Yi Jiao, Teguh Panca Putra, Yipeng Sun, Puneet Veer Tyagi, Lanfa Wang, Na Wang, Guohui Wei, Guoxing Xia, Dao Xiang, Qingjin Xu, Yuan Zhang, Wei Zheng, and many others. Many thanks to all those who have shared their lives and struggles with me, to those who stayed with me and enriched my life in so many ways: badminton, basketball, hiking, Go, and so on, during the past years.

Finally, I want to give my warmest thanks to my family for their love and endless encouragement. My love goes out to my wife Mingyu, who has been supporting me in every aspect of my life and encouraging me to be the best individual I can be.

Contents

List of Figures **ix**

List of Tables **xiii**

1 Introduction **1**

1.1 Electron storage rings 1

1.2 Electromagnetic theory of wake fields and impedance 3

1.2.1 Maxwell's equations 3

1.2.2 Wake fields and impedance 6

1.2.3 Properties of wake functions and impedance 11

1.2.4 Paraxial approximation 14

1.3 Incoherent and coherent synchrotron radiation in electron storage rings 15

1.4 Scope of this thesis 21

2 Coherent synchrotron radiation **23**

2.1 Introduction 23

2.2 Field theory 28

2.3 Formalism for numerical calculations of longitudinal CSR impedance 32

2.3.1 Parabolic differential equation 32

2.3.2 Geometry of the beam chamber 33

2.3.3 Field separation 35

2.3.4 Initial conditions 38

2.3.5 Boundary conditions 38

2.3.6 Field in the straight chamber 39

2.4 Finite difference technique 41
2.5 Numerical results 45
2.5.1 Single dipole 45
2.5.2 Interference in a series of bending magnets 53
2.5.3 Application to the compact-ERL at KEK 57
2.5.4 CSR in a wiggler 63

3 Coherent wiggler radiation 69
3.1 Introduction 69
3.2 General theorems and formulas 70
3.2.1 Eigenfunction expansion method to solve inhomogeneous differential equation 70
3.2.2 Eigenmodes of a uniform waveguide 73
3.2.3 Dyadic Green's function and vector potential 77
3.3 Fields of a point charge moving with constant velocity in a rectangular waveguide 82
3.4 Coherent wiggler radiation 88
3.4.1 Beam spectrum 88
3.4.2 Electric fields in a finite-length wiggler 92
3.4.3 Wake potential and impedance 94
3.4.4 Simplification of the solutions 99
3.4.5 CWR impedance due to imaginary frequencies 105
3.4.6 An infinite long wiggler 108

4 Microwave instability 111
4.1 Introduction 111
4.2 Deviations from steady-state models 114
4.3 Code development for simulations of microwave instability 116
4.3.1 Operator splitting 117
4.3.2 Discrete operator 118
4.4 Microwave instability in the KEKB low energy ring 119
4.4.1 Quasi Green's function of wake potential 120
4.4.2 Simulation results and comparison with measurements . . 123

4.5 Microwave instability in the SuperKEKB positron damping ring 126
4.5.1 Instability analysis based on broad-band CSR impedance 128
4.5.2 Instability analysis in the presence of narrow-band CSR impedance 129

5 Summary and outlook **133**
5.1 Summary 133
5.1.1 Coherent synchrotron radiation 133
5.1.2 Coherent wiggler radiation 134
5.1.3 Microwave instability 135
5.2 Directions for future work 135
5.2.1 Numerical method based on the parabolic equation 136
5.2.2 Analytical method of eigenfunction expansion 136

References **139**

List of Figures

1.1 Layout of KEKB low energy ring. 2
1.2 Coordinates of the point charges q_1 and q_2. 7
1.3 Beam orbit and spherical polar coordinates for a charged particle traversing a bending magnet. 18

2.1 The geometry of the curved chamber for a single bending magnet. 34
2.2 The geometry of the curved chamber for a wiggler. 34
2.3 Staggered grid definition with ghost points outside the boundary of the chamber. 42
2.4 Horizontal radiation field established by a beam in a straight chamber. 45
2.5 CSR impedance for a single bending magnet with $R = 1$ m. . . . 46
2.6 CSR impedance and wake potential for a single bending magnet with $R = 5$ m. 47
2.7 CSR reflected by the outer wall of the beam pipe. 49
2.8 Contour plots for the profiles of the radiation field with $k = 1230$ m^{-1}. 52
2.9 Contour plots for the profiles of the radiation field with $k = 4930$ m^{-1}. 52
2.10 Contour plots for the profiles of the radiation field with $k = 9100$ m^{-1}. 52
2.11 Contour plots for the field patterns of a rectangular toroidal pipe. 53
2.12 CSR impedance and wake potential for 4 bending magnets interleaved with equidistant drift chambers. 54
2.13 Layout of SuperKEKB positron damping ring. 55
2.14 Bending radius as a function of s for one arc cell of SuperKEKB positron damping ring. 56

LIST OF FIGURES

2.15 CSR impedance and wake potential of the arc section in the SuperKEKB positron damping ring. 56
2.16 CSR impedance for a single bend in the cERL return loop - Relativistic effect. 57
2.17 CSR wake potentials for a single bend in the cERL return loop - Relativistic effect. 58
2.18 CSR wake potentials for a single bend in the cERL return loop - Without drift CSR. 59
2.19 CSR impedance for a single bend in the cERL return loop - Drift effect. 60
2.20 CSR wake potentials for a single bend in the cERL return loop - Drift effect. 61
2.21 CSR wake potentials for a single bend in the cERL return loop - Drift CSR. 62
2.22 CSR impedance and wake potential of a wiggler. 63
2.23 CSR impedance and wake potential of a wiggler with various chamber heights. 64
2.24 CSR impedance and wake potential of a wiggler with various lengths. 65
2.25 Bending radius as function of s for one super-period in the wiggler section of SuperKEKB low energy ring. 67
2.26 CSR impedance and wake potential of the wiggler section in the SuperKEKB low energy ring. 67

3.1 Parabolic dispersion relation of waves propagating in a waveguide. 75
3.2 Dispersion relation of imaginary-frequency waves in a waveguide. . 76
3.3 Contour for the complex integration over β. 78
3.4 Dispersion relation for the waves excited by a point charge moving along a perfectly conducting waveguide. 85
3.5 The geometry of the straight rectangular chamber for a wiggler. . 88
3.6 The beam orbit inside a wiggler. 89
3.7 Dispersion relation for the waves excited by a point charge moving along a perfectly conducting waveguide sandwiched by a wiggler. . 93
3.8 CWR impedance of a wiggler. 104

3.9 CWR impedance of a wiggler with high order modes considered. . 105
3.10 Imaginary part of the CWR impedance. 108
3.11 Imaginary part of the CSR impedance of an infinitely long wiggler. 110

4.1 Ratio of the thresholds of coasting beam model to the bunched beam model. 113
4.2 Calculated geometrical wake potentials of 0.5 mm bunch for KEKB LER. 120
4.3 Calculated geometrical, resistive wall and CSR wake potentials of 0.5 mm bunch for KEKB LER. 121
4.4 Calculated loss factor as a function of bunch length for KEKB LER. 122
4.5 Comparison of calculated and measured loss factor as a function of bunch length for KEKB LER. 123
4.6 Bunch length as function of bunch current at KEKB LER. 125
4.7 Energy spread as function of bunch crrent at KEKB LER. 126
4.8 The CSR threshold as a function of the wavelength in SuperKEKB DR. 129
4.9 Quality factor and shunt impedance as a function of number of cells. 131

LIST OF FIGURES

List of Tables

4.1 Main parameters of KEKB LER. 124
4.2 Main parameters used in tracking simulations for the SuperKEKB DR 127
4.3 Some critical parameters related to CSR for the SuperKEKB DR 127

LIST OF TABLES

1

Introduction

1.1 Electron storage rings

In the past few decades, there have been increasing storage rings built as colliders or powerful synchrotron radiation sources which are essential research tools applied in diverse fields of science, such as physics, chemistry, biology, etc. A storage ring is a type of circular charged-particle accelerator in which charged beam may be stored for a long period of time at a constant energy. Modern electron storage rings work at ultra-relativistic energies and the electron's speed becomes extremely close to the speed of light.

The most common components in a storage ring are a circular evacuated pipe, a series of magnets, RF cavities, etc. The evacuated pipe provides the necessary vacuum to avoid beam-gas collisions which can cause gradual loss of particles. Dipole magnets are used to confine the beam in a closed orbit. As an example, Fig. 1.1 shows the layout of the KEKB low energy ring [1], where the dipoles keep the beam circulating along a closed orbit which looks like a racetrack. Interleaving the dipole magnets with an appropriate arrangement of quadrupole and sextupole magnets can give a suitable focusing system to keep small beam sizes. RF cavities are used to replace energy lost through synchrotron radiation and other processes.

When the charged beam passes through the dipole magnets, radiation is emitted in the direction tangential to the beam trajectory. In an electron or positron storage ring, the dynamics of the charged beam is significantly affected by the

radiation from the beam itself. The quality and stability of the beam in storage rings may be limited by the synchrotron radiation.

This study focuses on the beam physics involving synchrotron radiation in electron storage rings (for fundamental principles of beam physics in circular accelerators, for examples, see Refs. [2, 3, 4, 5]), where the electron beams are bunched. It is trivial to apply the same theories to positron storage rings because the only difference is the sign of charge. In storage rings of colliders or light sources, the overall machine performance essentially depends on the bunch current of the circulating beam. In addition to the single-particle beam dynamics, collective beam instability due to various sources can be essential in limiting the machine performance. The scope of the topic is narrowed and focused on the collective effects due to the beam interacting with its self-induced electromagnetic fields.

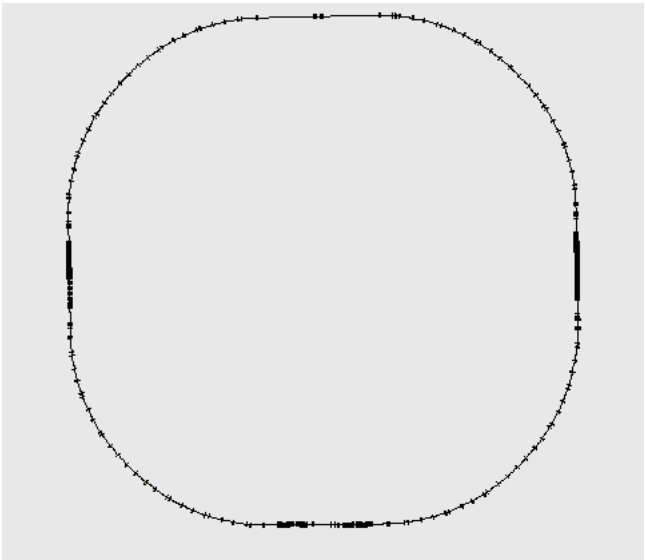

Figure 1.1: Layout of KEKB low energy ring. Only dipole magnets (main dipoles, correctors and wigglers), which form the closed orbit for the electron beam, are marked in the plot.

1.2 Electromagnetic theory of wake fields and impedance

1.2.1 Maxwell's equations

Conventionally, the interaction between the beam and the beam-induced fields is described as wake fields and coupling impedance. Therefore, it is natural to start from introducing the fundamental electromagnetic theory. This subsection follows Ref. [6] to derive the field equations based on the Maxwell's equations. These field equations will build up the basis of this thesis.

Consider a charged beam traveling with velocity $\vec{v}$ along a prescribed trajectory inside a vacuum chamber. The resulting electromagnetic fields $\vec{\mathcal{E}}$ and $\vec{\mathcal{B}}$ are governed by the Maxwell's equations. In differential form these equations are

$$\nabla \times \vec{\mathcal{E}} = -\frac{\partial \vec{\mathcal{B}}}{\partial t}, \tag{1.1a}$$

$$\nabla \times \vec{\mathcal{B}} - \mu_0 \epsilon_0 \frac{\partial \vec{\mathcal{E}}}{\partial t} = \mu_0 \vec{\mathcal{J}}, \tag{1.1b}$$

$$\nabla \cdot \vec{\mathcal{B}} = 0, \tag{1.1c}$$

$$\nabla \cdot \vec{\mathcal{E}} = \frac{\varrho}{\epsilon_0}, \tag{1.1d}$$

$$\nabla \cdot \vec{\mathcal{J}} = -\frac{\partial \varrho}{\partial t}. \tag{1.1e}$$

Here, ϱ is the charge density, and $\vec{\mathcal{J}}$ is the current density. The parameters μ_0 and ϵ_0 are the permeability and permittivity of free space, respectively. The equation of continuity Eq. (1.1e) gives $\vec{\mathcal{J}} = \varrho \vec{v}$. In the presence of boundaries, extra conditions for fields on the boundaries should be satisfied. Consider a perfectly conducting surface, in general, the boundary conditions take the form of

$$\vec{n} \times \vec{\mathcal{E}} = 0, \quad \vec{n} \cdot \vec{\mathcal{B}} = 0, \tag{1.2}$$

where $\vec{n}$ is the unit vector normal to the surface.

In the vacuum, the magnetic induction $\vec{\mathcal{B}}$ is proportional to the magnetic field $\vec{\mathcal{H}}$ with a simple relation of $\vec{\mathcal{B}} = \mu_0 \vec{\mathcal{H}}$. From Eq. (1.1c), the magnetic induction

is always solenoidal and may be expressed by the curl of a vector potential $\vec{\mathcal{A}}$ as follows

$$\vec{\mathcal{B}} = \nabla \times \vec{\mathcal{A}}. \tag{1.3}$$

Since $\nabla \cdot \nabla \times \vec{\mathcal{A}} \equiv 0$, this makes $\nabla \cdot \vec{\mathcal{B}} = 0$ as well. The vector $\vec{\mathcal{A}}$ is called the magnetic vector potential and may have both a solenoidal and a lamellar part. At this stage of the analysis the lamellar part is entirely arbitrary since $\nabla \times \vec{\mathcal{A}}_l = 0$. Substituting Eq. (1.3) into the curl equation for $\vec{\mathcal{E}}$ gives

$$\nabla \times (\vec{\mathcal{E}} + \frac{\partial \vec{\mathcal{A}}}{\partial t}) = 0, \tag{1.4}$$

where $c \equiv \frac{1}{\sqrt{\mu_0 \epsilon_0}}$ is the light speed in vacuum. Since $\nabla \times \nabla\Phi \equiv 0$, the above result may be integrated to give

$$\vec{\mathcal{E}} = -\frac{\partial \vec{\mathcal{A}}}{\partial t} - \nabla\Phi, \tag{1.5}$$

where Φ is called the electric scalar potential. So far two of Maxwell's equations are satisfied, i.e. Eqs. (1.1a) and (1.1c), and it remains to find the relation between Φ and $\vec{\mathcal{A}}$ and the condition on Φ and $\vec{\mathcal{A}}$ so that the two remaining equations (1.1b) and (1.1d) are satisfied. The curl equation for $\vec{\mathcal{B}}$ gives

$$\begin{aligned} \nabla \times \nabla \times \vec{\mathcal{A}} &= \nabla\nabla \cdot \vec{\mathcal{A}} - \nabla^2 \vec{\mathcal{A}} \\ &= \mu_0 \epsilon_0 \frac{\partial \vec{\mathcal{E}}}{\partial t} + \mu_0 \vec{\mathcal{J}} \\ &= -\frac{1}{c^2} \left(\frac{\partial^2 \vec{\mathcal{A}}}{\partial t^2} + \nabla \frac{\partial \Phi}{\partial t} \right) + \mu_0 \vec{\mathcal{J}}. \end{aligned} \tag{1.6}$$

Since Φ and the lamellar part of $\vec{\mathcal{A}}$ are as yet arbitrary, one is free to choose a relationship between them. For purpose of simplification, one can choose

$$\nabla \cdot \vec{\mathcal{A}} = -\frac{1}{c^2} \frac{\partial \Phi}{\partial t} \tag{1.7}$$

which is called the Lorentz gauge condition. Using Eq. (1.7), one finds that Eq. (1.6) reduces to

$$\nabla^2 \vec{\mathcal{A}} - \frac{1}{c^2} \frac{\partial^2 \vec{\mathcal{A}}}{\partial t^2} = -\mu_0 \vec{\mathcal{J}} \tag{1.8}$$

Using the Lorentz condition to eliminate $\nabla \cdot \vec{\mathcal{A}}$ gives the following equation to be satisfied by the scalar potential Φ:

$$\nabla^2 \Phi - \frac{1}{c^2} \frac{\partial^2 \Phi}{\partial t^2} = -\frac{\varrho}{\epsilon_0}. \tag{1.9}$$

Equations (1.8) and (1.9) are the vector and scalar inhomogeneous wave equations, respectively. Using the Lorentz condition, the field may be written in terms of the vector potential alone as follows

$$\vec{\mathcal{B}} = \nabla \times \vec{\mathcal{A}}, \tag{1.10a}$$

$$\vec{\mathcal{E}} = -\frac{\partial \vec{\mathcal{A}}}{\partial t} + c^2 \int^t \nabla \nabla \cdot \vec{\mathcal{A}}. \tag{1.10b}$$

Many times it is more convenient to work with field quantities in the frequency domain rather than in the time domain. Since any physically realizable time-varying function can be decomposed into a spectrum of waves by means of Fourier integral, there is little loss of generality [6]. The Fourier transform may be defined as

$$\mathcal{F}(t) = \frac{1}{2\pi} \int_{-\infty}^{\infty} F(\omega) e^{-i\omega t} \, d\omega, \tag{1.11}$$

and

$$F(\omega) = \int_{-\infty}^{\infty} \mathcal{F}(t) e^{i\omega t} \, dt, \tag{1.12}$$

where ω is the radian frequency. The time variation in the form of Eq. (1.11) implies that the time differentiations can be replaced by $-i\omega$. In our notation, the field quantities in the frequency domain will be denoted in roman type or tilded variables. With the time-varying factor $e^{-i\omega t}$ dropped, the wave equations for potentials change to the versions of inhomogeneous Helmholtz equations

$$\nabla^2 \vec{A} + k^2 \vec{A} = -\mu_0 \vec{J} \tag{1.13}$$

and

$$\nabla^2 \tilde{\Phi} + k^2 \tilde{\Phi} = -\frac{\rho}{\epsilon_0}, \tag{1.14}$$

where $k \equiv \omega/c$ is the wavenumber. The Lorentz gauge condition Eq. (1.7) reads

$$\tilde{\Phi} = \frac{c^2}{i\omega} \nabla \cdot \vec{A}. \tag{1.15}$$

The magnetic induction and electric field are given by

$$\vec{B} = \nabla \times \vec{A}, \tag{1.16a}$$

$$\vec{E} = i\omega\vec{A} - \nabla\tilde{\Phi} = i\omega\vec{A} - \frac{c^2}{i\omega}\nabla\nabla\cdot\vec{A}. \tag{1.16b}$$

One can also derive the wave equations of electric fields and magnetic induction directly from the time-domain Maxwell's equations. The equations are

$$\nabla^2\vec{\mathcal{E}} - \frac{1}{c^2}\frac{\partial^2\vec{\mathcal{E}}}{\partial t^2} = \frac{1}{\epsilon_0}\nabla\varrho + \mu_0\frac{\partial\vec{\mathcal{J}}}{\partial t}, \tag{1.17}$$

and

$$\nabla^2\vec{\mathcal{B}} - \frac{1}{c^2}\frac{\partial^2\vec{\mathcal{B}}}{\partial t^2} = -\mu_0\nabla\times\vec{\mathcal{J}}. \tag{1.18}$$

The corresponding equations in the frequency domain are

$$\nabla^2\vec{E} + k^2\vec{E} = \frac{1}{\epsilon_0}\nabla\rho - i\mu_0 kc\vec{J}, \tag{1.19}$$

and

$$\nabla^2\vec{B} + k^2\vec{B} = -\mu_0\nabla\times\vec{J}. \tag{1.20}$$

The flux density of electromagnetic energy, i.e. Poynting vector, is defined as

$$\vec{\mathcal{S}} = \frac{1}{\mu_0}\vec{\mathcal{E}}\times\vec{\mathcal{B}}. \tag{1.21}$$

1.2.2 Wake fields and impedance

In particle accelerators, the charged beam generates electromagnetic fields when traveling inside the vacuum chamber. The beam-induced fields are usually referred to as wake fields in the literature because they mainly remain behind the source charge at high beam energy. This terminology is followed in this thesis, but one should note that wake fields can also overtake the source beam in the cases of a beam moving at the velocity of $v < c$, or along a curved trajectory.

A general description of wake fields and impedance theory by Palumbo, *et al.* [7] is followed here. The generality lies in no assumption of cylindrical symmetry for the vacuum chamber. It will be more convenient for discussing the wake

fields and impedance due to coherent synchrotron radiation (CSR) in a rectangular vacuum chamber as to be shown in next chapters. Consider a point charge q_1 traveling with constant velocity v inside a region with prescribed trajectory (see Fig. 1.2). The region can be a vacuum chamber and is considered to be passive. That is, the vacuum chamber can only absorb energy from, not generate energy to, the charged particle. The particle trajectory is usually a straight line parallel to the axis of the vacuum chamber. The Cartesian coordinate system of (x, y, s) is chosen tentatively, while s-axis denotes the direction of beam motion. Let $\vec{r}_1 = (x_1, y_1, s_1)$ be the position of q_1. Due to constant velocity, the longitudinal position can be defined as $s_1 = vt$. It is assumed that the transverse coordinates (x_1, y_1) will not vary with time. The corresponding charge and current densities are described by the Dirac delta function, i.e.

$$\varrho_1(\vec{r}, t) = q_1 \delta(\vec{r} - \vec{r}_1), \tag{1.22}$$

and

$$\vec{\jmath}_1(\vec{r}, t) = \varrho_1(\vec{r}, t)\vec{v}. \tag{1.23}$$

Applying Eqs. (1.22) and (1.23) to the Maxwell's equations, i.e. Eqs. (1.1), one can obtain the time-varying electromagnetic fields $\vec{\mathcal{E}}$ and $\vec{\mathcal{B}}$ generated by q_1.

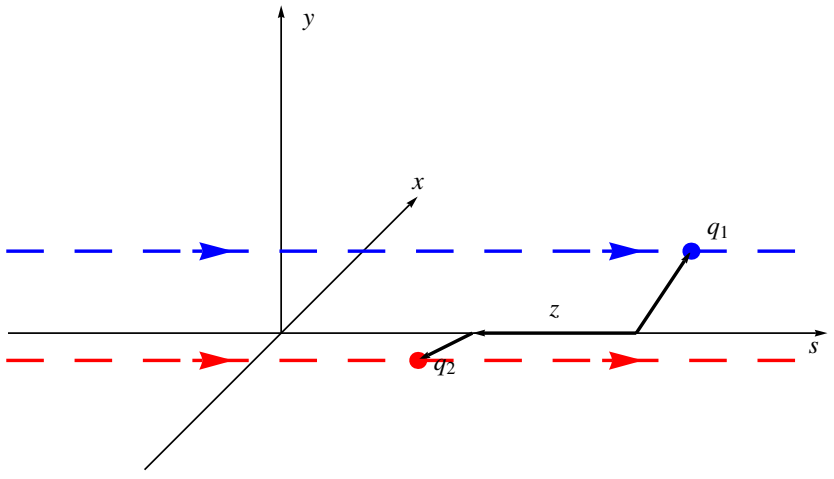

Figure 1.2: Coordinates of the point charges q_1 and q_2. The charge q_2 follows q_1 for $z > 0$ and vice versa for $z < 0$.

Imagine that a virtual point charge q_2 has coordinates $\vec{r}_2 = (x_2, y_2, s_2)$. The charge q_2 follows q_1 entering the same region with the same velocity but at a time delay of $\tau = z/v$, which implies that $s_2 = v(t - \tau)$ (see Fig. 1.2). The electromagnetic fields generated by q_1 exerts Lorentz force on q_2 by

$$\vec{\mathcal{F}}(\vec{r}_2, \vec{r}_1; t) = q_2 \left[\vec{\mathcal{E}}(\vec{r}_2, \vec{r}_1; t) + \vec{v} \times \vec{\mathcal{B}}(\vec{r}_2, \vec{r}_1; t) \right]. \tag{1.24}$$

To formulate the theory of wake fields and impedance, two approximations are introduced as a basis by following Ref. [8]:

1. **The rigid-beam approximation:** This approximation defines the status of the charged beam when it traverses the region considered. It says that the beam is rigid and its motion will not be affected by the wake fields during the traversal of the region. Namely, the motions of q_1 and q_2 in our model will not be affected by the wake fields.

2. **The impulse approximation:** This approximation defines the effect of the wake fields. It says that the wake effect is only considered as an impulse perturbation applied to the test particle when it completes the traversal; during traversing the region, the wake force will not change the motion of the test particle (rigid-beam approximation). The impulse is defined as the integral of the wake force with respect to time.

With the above approximations, one can calculate the impulse kick applied to q_2 by integrating the Lorentz force along the region

$$\overline{\vec{\mathcal{F}}}(\vec{r}_{2\perp}, \vec{r}_{1\perp}; \tau) = \int_{\tau}^{\tau + \frac{L}{v}} dt \; v\vec{\mathcal{F}}(\vec{r}_2, \vec{r}_1; t), \quad \text{with } s_1 = vt \text{ and } s_2 = v(t - \tau). \tag{1.25}$$

The subscripts $\perp$ in Eq. (1.25) represent the transverse coordinates, i.e. $\vec{r}_{2\perp} = (x_2, y_2)$ and $\vec{r}_{1\perp} = (x_1, y_1)$. The integration interval $(\tau, \tau + \frac{L}{v})$ indicates the range of the region along s-axis. Sometimes the interval can be replaced by $(-\infty, \infty)$ without ambiguity if the region considered extends to infinite length. The quantity $\overline{\vec{\mathcal{F}}}$ is called the wake potential, which is a function of τ and the transverse coordinates of source and test particles. When writing down Eq. (1.25), the rigid-beam and impulse approximations have already been used. And one notices that $\vec{r}_{2\perp}$ and $\vec{r}_{1\perp}$ are independent of time.

The wake potential $\overline{\vec{\mathcal{F}}}$ can be decomposed into two parts: the longitudinal component $\overline{\vec{\mathcal{F}}}_\parallel$ which is parallel to the beam trajectory and the transverse component $\overline{\vec{\mathcal{F}}}_\perp$ which is perpendicular to the beam trajectory. Correspondingly, the longitudinal and transverse wake functions $W_\parallel(\vec{r}_{2\perp}, \vec{r}_{1\perp}; \tau)$ and $\vec{W}_\perp(\vec{r}_{2\perp}, \vec{r}_{1\perp}; \tau)$ are defined as follows

$$W_\parallel(\vec{r}_{2\perp}, \vec{r}_{1\perp}; \tau) = -\frac{1}{q_1 q_2} \overline{\mathcal{F}}_\parallel(\vec{r}_{2\perp}, \vec{r}_{1\perp}; \tau), \tag{1.26a}$$

$$\vec{W}_\perp(\vec{r}_{2\perp}, \vec{r}_{1\perp}; \tau) = \frac{1}{q_1 q_2} \overline{\vec{\mathcal{F}}}_\perp(\vec{r}_{2\perp}, \vec{r}_{1\perp}; \tau). \tag{1.26b}$$

Note that here the longitudinal and transverse wake functions are defined as scalar and vector functions respectively. The longitudinal wake function indicates the energy loss of the test particle per unit of both charges q_1 and q_2. The transverse wake function indicates the transverse momentum kick acted on the test particle per unit of both charges q_1 and q_2.

Using Fourier transform, one can calculate the spectrum of the wake functions, so called impedance, as

$$Z_\parallel(\vec{r}_{2\perp}, \vec{r}_{1\perp}; \omega) = \int_{-\infty}^{\infty} d\tau \; W_\parallel(\vec{r}_{2\perp}, \vec{r}_{1\perp}; \tau) e^{i\omega\tau}, \tag{1.27a}$$

$$Z_\perp(\vec{r}_{2\perp}, \vec{r}_{1\perp}; \omega) = \frac{i}{v/c} \int_{-\infty}^{\infty} d\tau \; W_\perp(\vec{r}_{2\perp}, \vec{r}_{1\perp}; \tau) e^{i\omega\tau}. \tag{1.27b}$$

Then the wake functions expressed by inverting the above Fourier transforms are

$$W_\parallel(\vec{r}_{2\perp}, \vec{r}_{1\perp}; \tau) = \frac{1}{2\pi} \int_{-\infty}^{\infty} d\omega \; Z_\parallel(\vec{r}_{2\perp}, \vec{r}_{1\perp}; \omega) e^{-i\omega\tau}, \tag{1.28a}$$

$$W_\perp(\vec{r}_{2\perp}, \vec{r}_{1\perp}; \tau) = \frac{i}{2\pi} \int_{-\infty}^{\infty} d\omega \; Z_\perp(\vec{r}_{2\perp}, \vec{r}_{1\perp}; \omega) e^{-i\omega\tau}. \tag{1.28b}$$

The imaginary constant i appears in Eqs. (1.27b) and (1.28b) due to a historical convention. There is a monograph by Zotter and Kheifets [9] on calculations of wakes and impedances from various sources in high-energy particle accelerators.

Assume that the test particle q_2 has a distribution with charge density $\varrho_2(\vec{r}, \vec{r}_2, t-\tau)$, and the Lorentz force Eq. (1.24) can be equivalently written as

$$\vec{\mathcal{F}}(\vec{r}_2, \vec{r}_1; t) = \int\int\int dV \; \varrho_2(\vec{r}, \vec{r}_2, t-\tau) \left[\vec{\mathcal{E}}(\vec{r}, \vec{r}_1; t) + \vec{v} \times \vec{\mathcal{B}}(\vec{r}, \vec{r}_1; t) \right], \tag{1.29}$$

where $\vec{r}_2$ denotes the center of the distribution of q_2. It is more appropriate to formulate the longitudinal wake potential as

$$\overline{\mathcal{F}}_{\parallel}(\vec{r}_{2\perp}, \vec{r}_{1\perp}; \tau) = \int_{\tau}^{\tau+\frac{L}{v}} dt \ \vec{v} \cdot \vec{\mathcal{F}}(\vec{r}_2, \vec{r}_1; t). \tag{1.30}$$

Substituting Eq. (1.29) into Eq. (1.30), one gets

$$\overline{\mathcal{F}}_{\parallel}(\vec{r}_{2\perp}, \vec{r}_{1\perp}; \tau) = \int_{\tau}^{\tau+\frac{L}{v}} dt \ \int\int\int dV \ \varrho_2(\vec{r}, \vec{r}_2, t-\tau)\vec{v} \cdot \vec{\mathcal{E}}(\vec{r}, \vec{r}_1; t). \tag{1.31}$$

The term of $\varrho_2(\vec{r}, \vec{r}_2, t-\tau)\vec{v} = \vec{\mathcal{J}}_2(\vec{r}, \vec{r}_2, t-\tau)$ is recognized to be the current density. Therefore, the longitudinal wake potential can be expresses by

$$\begin{aligned}\overline{\mathcal{F}}_{\parallel}(\vec{r}_{2\perp}, \vec{r}_{1\perp}; \tau) &= \int_{\tau}^{\tau+\frac{L}{v}} dt \ \int\int\int dV \ \vec{\mathcal{J}}_2(\vec{r}, \vec{r}_2, t-\tau) \cdot \vec{\mathcal{E}}(\vec{r}, \vec{r}_1; t) \\ &= \int_{0}^{\frac{L}{v}} dt \ \int\int\int dV \ \vec{\mathcal{J}}_2(\vec{r}, \vec{r}_2, t) \cdot \vec{\mathcal{E}}(\vec{r}, \vec{r}_1; t+\tau). \end{aligned} \tag{1.32}$$

The second equality is justified by changing the integration variable $t \to t + \tau$. Then, the longitudinal wake function reads

$$W_{\parallel}(\vec{r}_{2\perp}, \vec{r}_{1\perp}; \tau) = -\frac{1}{q_1 q_2} \int_{0}^{\frac{L}{v}} dt \ \int\int\int dV \ \vec{\mathcal{J}}_2(\vec{r}, \vec{r}_2, t) \cdot \vec{\mathcal{E}}(\vec{r}, \vec{r}_1; t+\tau). \tag{1.33}$$

Substituting the Fourier transform of the electric field into the above equation, one can find the longitudinal impedance as follows by comparing it with Eq. (1.28a):

$$Z_{\parallel}(\vec{r}_{2\perp}, \vec{r}_{1\perp}; \omega) = -\frac{1}{q_1 q_2} \int_{0}^{\frac{L}{v}} dt \ \int\int\int dV \ \vec{\mathcal{J}}_2(\vec{r}, \vec{r}_2, t) \cdot \vec{E}(\vec{r}, \vec{r}_{1\perp}; \omega) e^{-i\omega t}. \tag{1.34}$$

The above equation tells that the longitudinal impedance is obtained once the electric field generated by a beam was found by solving Maxwell's equations in the frequency domain. In particular, for a point charge with constant velocity, i.e. $\vec{\mathcal{J}}_2(\vec{r}, \vec{r}_2, t) = q_2 \delta(\vec{r} - \vec{r}_2)\vec{v}$, one has [10]

$$Z_{\parallel}(\vec{r}_{2\perp}, \vec{r}_{1\perp}; \omega) = -\frac{1}{q_1} \int_{0}^{\frac{L}{v}} dt \ \vec{v} \cdot \vec{E}(\vec{r}_2, \vec{r}_{1\perp}; \omega) e^{-i\omega t}, \quad \text{with } s_2 = vt. \tag{1.35}$$

If one is only interested in the monopole impedance (or wake function), which is usually the dominant term, both the source and test charges can be put on the axis, i.e. $\vec{r}_{2\perp} = \vec{r}_{1\perp} = 0$.

The theory discussed so far about wake fields and impedance is general and is applicable to the cases of vacuum chambers with arbitrary shapes. If the chamber considered is cylindrically symmetric, the whole theory can be discussed under the framework of cylindrical coordinate system. The relevant detailed discussions can be found in Ref. [11].

In the above discussions, it has been assumed that the beam trajectory is along a straight line. Thus the point charges are in rectilinear motion. In practice, the direction of beam motion may vary with time. The region considered can also be free space instead of vacuum chamber. For instance, in some cases one must consider a curved trajectory due to external fields inside components such as bending magnets or separators. Then the above discussions have to be extended in proper ways. One possibility is to choose the local curvilinear coordinate system, and this case will be discussed in Chapter 2. If one adopts Cartesian coordinate system for a curved beam trajectory, both coordinates and velocity of the beam will vary with time. This case will be studied in detail in Chapter 3.

Once the longitudinal impedance of a structure is determined, one can use it to calculate the energy change of a bunched beam of charge q by

$$\Delta U = -\kappa_{\parallel} q^2, \tag{1.36}$$

where $\kappa_{\parallel}$ is the loss factor defined by

$$\kappa_{\parallel} = \frac{c}{\pi} \int_0^{\infty} \mathrm{Re} Z_{\parallel}(k) \left| \tilde{\lambda}(k) \right|^2 \, dk, \tag{1.37}$$

with $\tilde{\lambda}(k)$ the spectral density of the bunch. The symbol Re denotes taking the real part of the quantity concerned. On the other hand, if the spectral density of the energy loss is readily known, one can use Eq. (1.37) to calculate the real part of the longitudinal impedance, i.e.

$$\mathrm{Re} Z_{\parallel}(k) = -\frac{\pi}{q^2 c \left| \tilde{\lambda}(k) \right|^2} \frac{dU(k)}{dk}. \tag{1.38}$$

1.2.3 Properties of wake functions and impedance

The wake functions and impedance reflect the fundamental properties of a system and are independent of the charged beam, though they are derived from the

response of the system to a point-charge excitation. From the fact that the wake functions are always real, it can be concluded that $Z_{\parallel}(-\omega) = Z_{\parallel}^{*}(\omega)$ and $Z_{\perp}(-\omega) = -Z_{\perp}^{*}(\omega)$. Here the superscript * denotes taking the conjugate of a complex number. In many cases, the test particle moving ahead of the source particle does not feel forces, therefore the wake functions are causal, i.e. $W(\tau) = 0$ if $\tau < 0$. This is always true when the charged particle is moving along a straight line with the velocity $v = c$, because relativistic causality requires that no signal can propagate faster than the speed of light in vacuum. Causality is a fundamental principle in the physical world. Basically, it states that the effect cannot precede the cause. Here the causality is introduced in a mathematical way. And it is only for purpose of convenience in discussing the properties of wake functions. The reader may find that it is not connected to the causality which appears in physical phenomena. There exist various definitions of causality, an interesting discussion can be found in Ref. [12].

For the causal wake functions, the real and imaginary parts of their impedance are intimately related to each other. The relation can be described based on Titchmarsh theorem in mathematics (for instance, see Ref. [12]), which says that the three statements as follows are mathematically equivalent:

1. $W(\tau) = 0$ if $\tau < 0$ and $W(\tau)$ is a function belonging to the space of the square-integral functions $\mathbf{L^2}$.

2. Let $Z(\omega) \in \mathbf{L^2}$ be the Fourier transform of $W(\tau)$, if ω is real and if

$$Z(\omega) = \lim_{\omega' \to 0} Z(\omega + i\omega'), \tag{1.39}$$

   then $Z(\omega + i\omega')$ is holomorphic in the upper half-plane where $\omega' > 0$.

3. Hilbert transforms [13] connect the real and imaginary part of $Z(\omega)$ as follows:

$$\mathrm{Re}\{Z(\omega)\} = \frac{1}{\pi}\mathrm{P.V.}\int_{-\infty}^{\infty} \frac{\mathrm{Im}\{Z(\omega')\}}{\omega' - \omega} d\omega', \tag{1.40a}$$

$$\mathrm{Im}\{Z(\omega)\} = -\frac{1}{\pi}\mathrm{P.V.}\int_{-\infty}^{\infty} \frac{\mathrm{Re}\{Z(\omega')\}}{\omega' - \omega} d\omega', \tag{1.40b}$$

   where the symbol P.V. indicates taking the principal value of the relevant integral.

The causality of $W(\tau)$ implies that its Fourier transform $Z(\omega)$ is analytic in the upper complex ω-plane. The real and imaginary parts of $Z(\omega)$ are correlated via the Hilbert transforms. In the literature, Eqs. (1.40) are also called the Kramers-Kronig (K-K) relations [14, 15]. Alternative forms of K-K relations may be useful for practical calculations. Using the property of the impedance $Z(-\omega) = Z^*(\omega)$, one alternative by eliminating the negative frequency parts can be derived as follows

$$\mathrm{Re}\{Z(\omega)\} = \frac{2}{\pi}\mathrm{P.V.}\int_0^\infty \frac{\omega'\mathrm{Im}\{Z(\omega')\}}{\omega'^2-\omega^2}d\omega', \tag{1.41a}$$

$$\mathrm{Im}\{Z(\omega)\} = -\frac{2\omega}{\pi}\mathrm{P.V.}\int_0^\infty \frac{\mathrm{Re}\{Z(\omega')\}}{\omega'^2-\omega^2}d\omega'. \tag{1.41b}$$

It is possible to remove the trouble of divergence at $\omega' = \omega$ and improve the convergence of Eqs. (1.40) and (1.41). This results in another alternative as follows

$$\mathrm{Re}\{Z(\omega)\} = -\frac{2}{\pi}\int_0^\infty \frac{\omega'\left(\mathrm{Im}\{Z(\omega')\} - \mathrm{Im}\{Z(\omega)\}\right)}{\omega'^2-\omega^2}d\omega', \tag{1.42a}$$

$$\mathrm{Im}\{Z(\omega)\} = -\frac{2\omega}{\pi}\int_0^\infty \frac{\mathrm{Re}\{Z(\omega')\} - \mathrm{Re}\{Z(\omega)\}}{\omega'^2-\omega^2}d\omega'. \tag{1.42b}$$

It is noteworthy that there is no need to take the principal values of the relevant integrals in the above equations. The K-K relations provide the convenience of determining the imaginary part impedance from the real part, or vice versa. For example, they are very useful when the impedance is calculated using power spectrum method in the electromagnetic theory. In this case, one always calculates real functions of the electromagnetic fields, thus only real part impedance could be found, according to Eq. (1.38).

It should be emphasized that the previous discussions only apply for causal wake functions. For non-causal wake functions, such as those of the space charge and coherent synchrotron radiation, the above theories have to be extended. A simple application of K-K relations may fail to determine the correct answer. The readers will see that most of this thesis is dedicated to the study of non-causal wake functions and impedance.

1.2.4 Paraxial approximation

In many cases, the paraxial approximation of the full Maxwell's equations can be used for field calculations. In the optics theory, it is valid in the limit of small angles from the optical axis. It is also very useful for calculations of high-frequency coupling impedance in accelerators. This subsection is to illustrate the paraxial approximation of the wave equations obtained previously. Suppose that the source charge density has the form of

$$\varrho_1(\vec{r},t) = q_1\sigma(\vec{r}_\perp,\vec{r}_{1\perp})\delta(s-vt), \tag{1.43}$$

where $\sigma(\vec{r}_\perp,\vec{r}_{1\perp})$ is the distribution in the $x-y$ plane in a general form. $\vec{r}_{1\perp}$ denotes the center of the distribution. The quantities $\vec{r}_\perp$ and $\vec{r}_{1\perp}$ are assumed to be independent of time. Thus the corresponding spectra of charge and current densities are

$$\rho_1(\vec{r},\omega) = \int_{-\infty}^{\infty} dt\ \varrho_1(\vec{r},t)e^{i\omega t} = \frac{q_1}{v}\sigma(\vec{r}_\perp,\vec{r}_{1\perp})e^{i\omega s/v}, \tag{1.44}$$

and

$$J_1(\vec{r},\omega) = \frac{q_1\vec{v}}{v}\sigma(\vec{r}_\perp,\vec{r}_{1\perp})e^{i\omega s/v}. \tag{1.45}$$

Applying Eqs. (1.44) and (1.45) to Eq. (1.19), one has the equations for the Cartesian components of electric field in the frequency domain

$$\nabla^2 E_x + k^2 E_x = \frac{q_1}{\epsilon_0 v}e^{i\omega s/v}\frac{\partial\sigma(\vec{r}_\perp,\vec{r}_{1\perp})}{\partial x}, \tag{1.46a}$$

$$\nabla^2 E_y + k^2 E_y = \frac{q_1}{\epsilon_0 v}e^{i\omega s/v}\frac{\partial\sigma(\vec{r}_\perp,\vec{r}_{1\perp})}{\partial y}, \tag{1.46b}$$

$$\nabla^2 E_s + k^2 E_s = \frac{iq_1 k\sigma(\vec{r}_\perp,\vec{r}_{1\perp})}{\epsilon_0 c\beta^2\gamma^2}e^{i\omega s/v}, \tag{1.46c}$$

where $\beta \equiv v/c$ is the relative velocity and $\gamma \equiv 1/\sqrt{1-\beta^2}$ is the Lorentz factor. And it is assumed that the current density only has longitudinal component, i.e. $\vec{v} = (0,0,v)$. Notice that there is a common phase factor of $e^{i\omega s/v}$ on the right hand sides of the above equations. One can replace the electric field by $\vec{E} \equiv \vec{\mathbb{E}}e^{i\omega s/v}$ where $\vec{\mathbb{E}}$ represents the amplitude of the electric field, which modulates

the sinusoidal wave represented by the exponential factor. Then a new set of equations derived from Eqs. (1.46) can be obtained as follows

$$\nabla^2\mathbb{E}_x + \frac{2ik}{\beta}\frac{\partial\mathbb{E}_x}{\partial s} - \frac{k^2}{\beta^2\gamma^2}\mathbb{E}_x = \frac{q_1}{\epsilon_0 v}\frac{\partial\sigma(\vec{r}_\perp,\vec{r}_{1\perp})}{\partial x}, \tag{1.47a}$$

$$\nabla^2\mathbb{E}_y + \frac{2ik}{\beta}\frac{\partial\mathbb{E}_y}{\partial s} - \frac{k^2}{\beta^2\gamma^2}\mathbb{E}_y = \frac{q_1}{\epsilon_0 v}\frac{\partial\sigma(\vec{r}_\perp,\vec{r}_{1\perp})}{\partial y}, \tag{1.47b}$$

$$\nabla^2\mathbb{E}_s + \frac{2ik}{\beta}\frac{\partial\mathbb{E}_s}{\partial s} - \frac{k^2}{\beta^2\gamma^2}\mathbb{E}_s = \frac{iq_1 k\sigma(\vec{r}_\perp,\vec{r}_{1\perp})}{\epsilon_0 c\beta^2\gamma^2}. \tag{1.47c}$$

Assume that the amplitude function $\vec{\mathbb{E}}$ varies very slowly on the scale of a wavelength of $2\pi\beta/k$, then the paraxial approximation can be adopted. In our notation, the paraxial approximation requires that

$$\left|\frac{\partial^2\mathbb{E}_\nu}{\partial s^2}\right| \ll \left|k\frac{\partial\mathbb{E}_\nu}{\partial s}\right| \ll \left|k^2\mathbb{E}_\nu\right|, \quad \text{with } \nu = x,\ y,\ \text{or } s. \tag{1.48}$$

Because of the inequalities stated above, the term of $\frac{\partial^2\mathbb{E}_\nu}{\partial s^2}$ is negligible in comparison with the term of $\frac{\partial\mathbb{E}_\nu}{\partial s}$. Then the paraxial approximation of Eqs. (1.47) reads

$$\nabla_\perp^2\mathbb{E}_x + \frac{2ik}{\beta}\frac{\partial\mathbb{E}_x}{\partial s} - \frac{k^2}{\beta^2\gamma^2}\mathbb{E}_x = \frac{q_1}{\epsilon_0 v}\frac{\partial\sigma(\vec{r}_\perp,\vec{r}_{1\perp})}{\partial x}, \tag{1.49a}$$

$$\nabla_\perp^2\mathbb{E}_y + \frac{2ik}{\beta}\frac{\partial\mathbb{E}_y}{\partial s} - \frac{k^2}{\beta^2\gamma^2}\mathbb{E}_y = \frac{q_1}{\epsilon_0 v}\frac{\partial\sigma(\vec{r}_\perp,\vec{r}_{1\perp})}{\partial y}, \tag{1.49b}$$

$$\nabla_\perp^2\mathbb{E}_s + \frac{2ik}{\beta}\frac{\partial\mathbb{E}_s}{\partial s} - \frac{k^2}{\beta^2\gamma^2}\mathbb{E}_s = \frac{iq_1 k\sigma(\vec{r}_\perp,\vec{r}_{1\perp})}{\epsilon_0 c\beta^2\gamma^2}, \tag{1.49c}$$

where $\nabla_\perp^2$ stands for the transverse Laplacian. Once the solution of Eqs. (1.47) or (1.49) was found, one can derive another formula from Eq. (1.35) to calculate the longitudinal impedance:

$$Z_\parallel(\vec{r}_{2\perp},\vec{r}_{1\perp};\omega) = -\frac{1}{q_1}\int_0^L d\vec{s}_2\cdot\vec{\mathbb{E}}(\vec{r}_2,\vec{r}_{1\perp};\omega). \tag{1.50}$$

1.3 Incoherent and coherent synchrotron radiation in electron storage rings

In a storage ring, the charged beam is guided by the dipole magnets to achieve a closed orbit, and acceleration happens when the beam orbit is bent. The

radiation emitted from the accelerated beam in a storage ring is usually called synchrotron radiation after its discovery in a synchrotron accelerator [16]. Since then, synchrotron radiation has become a very powerful tool due to its amazing spectral brightness or brilliance. Various applications of probing the structure of matter have been investigated in the fields such as materials science, biology and medicine. Several monographs are dedicated to this topic (for examples, see Refs. [5, 17]), here only a brief overview of synchrotron radiation theory is given. A comprehensive review of its physics is available in Ref. [18]

In the case that there are no boundaries in the considered region, the retarded solutions of Eqs. (1.8) and (1.9) are given in the integral form of

$$\vec{\mathcal{A}}(\vec{r},t) = \frac{\mu_0}{4\pi}\int \vec{\mathcal{J}}\left(\vec{r}',t-\frac{|\vec{r}-\vec{r}'|}{c}\right)\frac{d\vec{r}'}{|\vec{r}-\vec{r}'|}, \tag{1.51}$$

$$\Phi(\vec{r},t) = \frac{1}{4\pi\epsilon_0}\int \varrho\left(\vec{r}',t-\frac{|\vec{r}-\vec{r}'|}{c}\right)\frac{d\vec{r}'}{|\vec{r}-\vec{r}'|}. \tag{1.52}$$

For a point charge e moving with velocity $\vec{v}$, the above solutions are reduced to the well-known Liénard-Wiechert potentials [19], i.e.

$$\vec{\mathcal{A}}(\vec{r},t) = \frac{\mu_0}{4\pi}\left[\frac{e\vec{v}}{|\vec{r}-\vec{r}'|\left(1-\vec{n}\cdot\vec{\beta}\right)}\right]_{ret}, \tag{1.53}$$

$$\Phi(\vec{r},t) = \frac{1}{4\pi\epsilon_0}\left[\frac{e}{|\vec{r}-\vec{r}'|\left(1-\vec{n}\cdot\vec{\beta}\right)}\right]_{ret}, \tag{1.54}$$

where $\vec{n} = (\vec{r}-\vec{r}')/|\vec{r}-\vec{r}'|$ is defined as a unite vector and $\vec{\beta} \equiv \vec{v}/c$. The subscript *ret* indicates that all quantities inside the symbol [ ] are evaluated at the retarded time $t' = t - |\vec{r}(t)-\vec{r}'(t')|/c$. Using the definitions of Eqs. (1.3) and (1.5), one can calculate the electric and magnetic fields from Eqs. (1.53) and (1.54). The results are

$$\vec{\mathcal{E}} = \frac{e}{4\pi\epsilon_0}\left\{\frac{\vec{n}-\vec{\beta}}{\gamma^2 K^3|\vec{r}-\vec{r}'|^2} + \frac{\vec{n}\times\left[(\vec{n}-\vec{\beta})\times\dot{\vec{\beta}}\right]}{cK^3|\vec{r}-\vec{r}'|}\right\}_{ret}, \tag{1.55}$$

$$\begin{aligned}\vec{\mathcal{B}} &= \frac{1}{c}\left[\vec{n}\times\vec{\mathcal{E}}\right]_{ret} \\ &= -\frac{\mu_0 e}{4\pi}\left\{\frac{\vec{n}\times\vec{\beta}c}{\gamma^2 K^3\left|\vec{r}-\vec{r}'\right|^2}+\frac{\vec{n}\times\left[\dot{\vec{\beta}}+\vec{n}\times\left(\vec{\beta}\times\dot{\vec{\beta}}\right)\right]}{K^3\left|\vec{r}-\vec{r}'\right|}\right\}_{ret},\end{aligned} \tag{1.56}$$

where $K = 1-\vec{n}\cdot\vec{\beta}$ and $\dot{\vec{\beta}} = d\vec{\beta}/dt'$.

The first term in the curly brackets of Eq. (1.55) is proportional to $1/\left|\vec{r}-\vec{r}'\right|^2$, where $\left|\vec{r}-\vec{r}'\right|$ indicates the distance from the point of observation to the source. Thus it is a generalized form of the Coulomb field. This term is also called "velocity field" because it only contains $\vec{\beta}$. Similar to the space-charge effect, the velocity field exchanges energy between the leading and trailing particles in a bunched beam. The second term is proportional to $1/\left|\vec{r}-\vec{r}'\right|$ and is only non-zero when $\dot{\vec{\beta}}\neq 0$. Thus this term is also called "radiation field". The straightforward implication is that a charged particle emits radiation when it is accelerated. As a total effect, the radiation field causes energy loss from the accelerated charged beam but the velocity field does not.

Suppose that the typical variation scale of the source charge and current is d. The field region can be divided into two parts: the near field region $\left|\vec{r}-\vec{r}'\right| = c(t-t') \ll d$ and the far field region $\left|\vec{r}-\vec{r}'\right| = c(t-t') \gg d$. The field properties of these two regions are quite different. In general, the velocity field dominates in the near field region and the radiation field dominates in the far field region. In the transition zone $\left|\vec{r}-\vec{r}'\right| = c(t-t') \sim d$, the strengths of these two types of field are comparable to each other.

The radiation power can be calculated using the Poynting vector Eq. (1.21). It is written as

$$\vec{\mathcal{S}}(t) = \frac{1}{\mu_0 c}\left[K\left|\vec{\mathcal{E}}\right|^2\vec{n}\right]_{ret}. \tag{1.57}$$

The instantaneous power radiated into per solid angle at the observation point is

$$\begin{aligned}\frac{dP(t')}{d\Omega} &= \left[\left|\vec{r}-\vec{r}'\right|^2\left(\vec{\mathcal{S}}\cdot\vec{n}\right)\right]_{ret} \\ &= \frac{e^2}{16\pi^2\epsilon_0 c}\frac{\left|\vec{n}(t')\times\left[\left(\vec{n}(t')-\vec{\beta}(t')\right)\times\dot{\vec{\beta}}(t')\right]\right|^2}{\left[1-\vec{n}(t')\cdot\vec{\beta}(t')\right]^5},\end{aligned} \tag{1.58}$$

with the velocity field ignored. In a storage ring, the charged particle traverses a bending magnet with its acceleration $\dot{\vec{\beta}}$ perpendicular to its velocity $\vec{\beta}$. Defining a

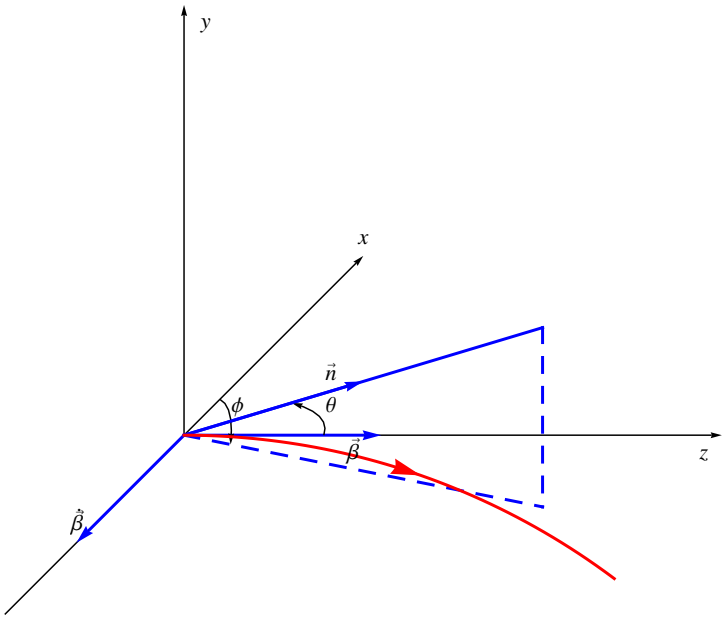

Figure 1.3: Beam orbit and spherical polar coordinates for a charged particle traversing a bending magnet. The red arrowed line indicates the beam orbit.

spherical polar coordinate system as shown in Fig. 1.3, Eq. (1.58) can be expressed in terms of polar angles θ and ϕ as following [20]

$$\frac{dP(t')}{d\Omega} = P_0 \frac{1}{(1-\beta\cos\theta)^3}\left[1 - \frac{\sin^2\theta\cos^2\phi}{\gamma^2(1-\beta\cos\theta)^2}\right], \tag{1.59}$$

where $P_0 = e^2\dot{\vec{\beta}}^2/(16\pi^2\epsilon_0 c)$. The angular distribution is mainly featured by the factor $1-\beta\cos\theta$ appearing in the denominators of Eq. (1.59). It suggests that the radiation is concentrated within a narrow cone in the forward direction of $\theta = 0$. In the relativistic limit of $\gamma \gg 1$, which is usually true in electron storage rings, the opening angle of the cone is estimated by $\Delta\theta = 2\cos^{-1}\beta \approx 2/\gamma$. In particular, the amplitude of the backward radiation with $\theta = \pi$ is proportional to $1/(1+\beta)^3$. This value is rather small comparing with that of the forward radiation with $\theta = 0$. One is thus led to conclude that the backward radiation is fairly negligible in the relativistic limit.

By applying the Fourier transform, the angular and spectral distribution of the radiation energy received by the observer is calculated as [19]

$$\begin{aligned}\frac{d^2U}{d\Omega dk} &= \frac{d}{dk}\int \frac{dP}{d\Omega}dt = \frac{2}{\mu_0}\left|\vec{r}-\vec{r}'\right|^2\left|\vec{E}(k)\right|^2 \\ &= \frac{e^2}{4\pi\epsilon_0}\frac{1}{4\pi^2}\left|\int_{-\infty}^{\infty}\frac{\vec{n}\times\left[\left(\vec{n}-\vec{\beta}\right)\times\dot{\vec{\beta}}\right]}{\left(1-\vec{n}\cdot\vec{\beta}\right)^2}e^{ik(ct-\vec{n}\cdot\vec{r}(t))}dt\right|^2 \\ &= \frac{e^2}{4\pi\epsilon_0}\frac{k^2c^2}{4\pi^2}\left|\int_{-\infty}^{\infty}\vec{n}\times\left(\vec{n}\times\vec{\beta}\right)e^{ik(ct-\vec{n}\cdot\vec{r}(t))}dt\right|^2. \end{aligned} \tag{1.60}$$

After tedious calculations, the above equation can be computed in the limit of small deflection angles and $\beta \to 1$. The result is [19]

$$\frac{d^2U}{d\Omega dk} = \frac{e^2}{4\pi\epsilon_0}\frac{3\gamma^2}{4\pi^2}\left(\frac{k}{k_C}\right)^2(1+\gamma^2\theta^2)^2\left[K_{2/3}^2(\xi)+\frac{\gamma^2\theta^2}{1+\gamma^2\theta^2}K_{1/3}^2(\xi)\right], \tag{1.61}$$

where $k_C = 3\gamma^3/(2R)$ is the critical wavenumber with the constant bending radius R. The quantity $K_{n/3}(x)$ is the modified Bessel functions of order $n/3$ and is related to the Airy functions [21] by

$$\mathrm{Ai}(x) = \frac{1}{\pi}\sqrt{x/3}K_{1/3}(2x^{3/2}/3), \quad \mathrm{Ai}'(x) = -\frac{1}{\pi}\frac{x}{\sqrt{3}}K_{2/3}(2x^{3/2}/3). \tag{1.62}$$

The parameter ξ is a dimensionless parameter defined by

$$\xi = \frac{k}{2k_C}\left(1+\gamma^2\theta^2\right)^{3/2}. \tag{1.63}$$

The spectral distribution of the total radiation energy emitted by a single particle can be obtained by a proper integration of Eq. (1.61) over angles; the result is [22]

$$\frac{dU}{dk} = \frac{e^2}{4\pi\epsilon_0}\sqrt{3}\gamma\frac{k}{k_C}\int_{k/k_C}^{\infty}K_{5/3}(x)dx. \tag{1.64}$$

In the limit of $k \ll k_C$, the above result reduces to a simple form of

$$\frac{dU}{dk} = \frac{e^2}{2\pi\epsilon_0}3^{1/6}\Gamma\left(2/3\right)(kR)^{1/3}, \tag{1.65}$$

where $\Gamma(x)$ is the gamma function. At this point one can find that, from the above equation, the real part of the longitudinal impedance per unit length due to synchrotron radiation can be determined using Eq. (1.38), i.e.

$$\frac{\mathrm{Re}Z_{\parallel SR}(k)}{L} = \frac{1}{2\pi R}\frac{\pi}{e^2 c}\frac{dU(k)}{dk} = \frac{Z_0}{4\pi}3^{1/6}\Gamma(2/3)\left(\frac{k}{R^2}\right)^{1/3}, \tag{1.66}$$

where $Z_0 = \sqrt{\mu_0/\epsilon_0}$. The above equation is exactly the well known formula for steady-state CSR impedance in free space [23], and it is valid for $k \ll k_C$.

For a bunched beam with current density $\vec{\mathcal{J}}(\vec{r},t)$, the angular and spectral distribution of the radiation energy can be calculated by slightly modifying Eq. (1.60), i.e.

$$\frac{d^2U}{d\Omega dk} = \frac{e^2}{4\pi\epsilon_0}\frac{k^2}{4\pi^2}\left|\int dt \int d\vec{r}\,\vec{n}\times\left(\vec{n}\times\vec{\mathcal{J}}(\vec{r},t)\right)e^{ik(ct-\vec{n}\cdot\vec{r}(t))}\right|^2. \tag{1.67}$$

At low frequencies, the wavelength of the synchrotron radiation fields may be comparable to or longer than the bunch length. The radiation fields emitted by different particles in a bunch may interfere with each other and become coherent. Consequently, the radiation power of the bunch at low frequency can be proportional to the square of the number of particles in the bunch. In modern electron storage rings, a single bunch may contains electrons in the order of $N = 10^9$ or higher. In this case, the coherence may lead to a very large enhancement factor in the radiation power spectrum. The coherence of the synchrotron radiation is intimately linked to the spatial distribution of the particles in a bunch. The longitudinal and transverse distributions are related to the temporal and spatial coherence, respectively. Usually, in an electron storage ring the transverse emittance of the beam is very small. Therefore assuming full transverse coherence is usually accepted for purpose of studying CSR induced beam instabilities. With non-rigorous calculations, the energetic spectrum of the total radiation is given by [20]

$$\left.\frac{dU}{dk}\right|_{bunch} = \left[N + N(N-1)\left|\tilde{\lambda}(k)\right|^2\right]\frac{dU}{dk}. \tag{1.68}$$

The first term in the above equation is the incoherent spectrum, while the second represents the coherent spectrum. For a Gaussian bunch of length σ_z,

$$\tilde{\lambda}(k) = e^{-k^2\sigma_z^2/2}. \tag{1.69}$$

It is easy to see that at wavenumber of $k \ll 1/\sigma_z$, $\tilde{\lambda}(k) \sim 1$ and the radiation spectrum is approximately proportional to N^2.

The interests on CSR have been growing since the late 1980s when numerous dedicated synchrotron light sources were built and operated. It was first observed in a linac at the Tohoku University [24]. Soon later it was found to be a potential candidate for a bright light source in terahertz region. A comprehensive historical review on CSR in storage rings has been readily in hand in Ref. [25]. On the other hand, CSR can be a primary obstacle to achieving ultra-short bunch length, ultra-low emittance, or ultra-high luminosity in modern storage rings. During the design of the SuperKEKB, it was found that the beam instability caused by CSR was so significant in the high-current option [26, 27], that it accounted for one of the important factors to changing to the present nano-beam scheme [28].

The importance of CSR has been increasingly recognized by the community of free electron lasers (FELs) and energy recovery linacs (ERLs) in recent years. Growing efforts have been directed to better understand the field dynamics of CSR, the CSR related effects in accelerator projects with ultra-low emittance and ultra-short beam bunches, schemes of suppressing unwanted CSR for FELs and ERLs, schemes of generating wanted CSR for THz light sources, etc. Usually people calculate the CSR wake fields in the time domain or impedance in the frequency domain and then evaluate its effects on the single-bunch beam dynamics. Historically, the space charge effect, Touschek effect and CSR have been treated independently. But all these effects are due the same Coulomb interaction among charged particles in a bunch. Theories for these topics can be put on the same basis as stated in Ref. [29].

1.4 Scope of this thesis

As mentioned previously in Section 1.1, this thesis is focused on the beam-induced electromagnetic fields and their effects on the beam dynamics in electron storage rings. The scope of this thesis was defined as understanding the coupling impedance due to coherent radiations and its effects on the single-bunch beam instability. Since the analytical solution is hard to derive, we first developed a numerical code for calculation of the coherent synchrotron radiation impedance.

Based on this numerical code, the longitudinal impedance due to CSR and coherent wiggler radiation (CWR) will be intensively investigated. Concerns on field dynamics of CSR and CWR will be addressed. For CWR, an exact solution is possibly to obtain based on a general eigenfunction expansion method. With the longitudinal impedance in hand, we will present results of estimating microwave instability for the storage rings at KEK.

The rest of this thesis is organized as follows. Chapter 2 introduces the code developments for CSR calculation, and many numerical examples of CSR and CWR will also be presented. In Chapter 3, the eigenfunction method is applied to calculate the CWR impedance. In an effort to verify the validity of the analytical model, an example of a weak wiggler was studied for purpose of benchmark against a simple model available in the literature and also numerical results using the newly developed code. Microwave instability in the KEKB low energy ring and SuperKEKB positron damping ring will be addressed in Chapter 4. A peculiar instability due to multi-bend CSR interference in the SuperKEKB positron damping ring is demonstrated based a simple instability analysis. The structure of each chapter listed above will start with a brief overview of the background and an introduction of the general theory of the relevant subject. Finally, summary of this thesis and outlook of future works are given in Chapter 5.

MKSA units are used throughout this thesis.

2

Coherent synchrotron radiation

2.1 Introduction

Since the concept of the impedance was introduced to describe CSR effects [30, 31], there have been tremendous efforts in calculating the CSR wake fields and impedance analytically. A comprehensive review of early efforts is available in Ref. [32]. In parallel to developments in analytical theories, various codes have also been developed to calculate the CSR wake fields and impedance (for examples, see Refs. [26, 33]), to study the CSR field dynamics [34], or to perform self-consistent macro-particle tracking simulations in storage rings or linacs. A comprehensive overview of CSR codes is available in Ref. [35]. Since then, tremendous efforts have been expended in developing new codes as well as investigating new numerical techniques. The new CSR codes are classified into 1D approach [33, 36, 37, 38, 39, 40], Newton-Maxwell approach [34, 41, 42], approach with paraxial approximation [26, 27, 43, 44], Vlasov-Maxwell approach [45, 46, 47] and Particle-In-Cell (PIC) approach [48, 49, 50, 51]. This classification is based on the numerical methods adopted by the CSR codes [52]. Another scheme is to classify the CSR codes into 1D, 2D, or 3D based on the simulated dimensions of CSR fields in real space. The discussions on simulations of beam dynamics with CSR involved are postponed to Chapter 4. The topic is narrowed to calculating CSR impedance in this chapter.

For a point charge moving in free space on a circle of radius R, in the limit of

$k \ll k_C = 3\gamma^3/(2R)$, the longitudinal impedance per unit length of path is [31]

$$\left.\frac{Z_\parallel(k)}{L}\right|_{FS} = \frac{Z_0}{2\pi}\Gamma\left(\frac{2}{3}\right)\left(\frac{ik}{3R^2}\right)^{1/3}. \tag{2.1}$$

From Eq. (1.28a), the wake function corresponding to the above impedance is [53]

$$\left.\frac{W_\parallel(z)}{L}\right|_{FS} = \frac{Z_0 c}{2\pi}\frac{1}{(9R)^{2/3}}\frac{1}{(-z)^{4/3}} \quad \text{for} \quad z<0. \tag{2.2}$$

The above equation is valid for $1/k_C \ll -z \ll R$. It indicates that only test particles ahead of the source particle feel CSR forces. The validity conditions are easily satisfied in the ultra-relativistic limit of $\gamma \to \infty$ and for short bunches in electron storage rings. Equations (2.1) and (2.2) represent the most popular one-dimensional (1D) steady-state model of CSR.

The shielding effects were first studied by placing two perfectly conducting plates in the horizontal plane [54]. This simple model allows one to replace the plates by mirror charges and reproduce the fields exactly in terms of summation over the mirror charges. The resulting formulae are expressed in terms of Bessel functions [53]. A simplified version of impedance in terms of Airy functions was found [26]

$$\begin{aligned}\left.\frac{Z_\parallel(k)}{L}\right|_{PP} =& \frac{2\pi Z_0}{b}\left(\frac{2}{kR}\right)^{1/3}\sum_{p=0}^{\infty}\Big\{\mathrm{Ai}'(X_p^2)\left[\mathrm{Ai}'(X_p^2) - i\mathrm{Bi}'(X_p^2)\right] \\ &+ X_p^2\mathrm{Ai}(X_p^2)\left[\mathrm{Ai}(X_p^2) - i\mathrm{Bi}(X_p^2)\right]\Big\},\end{aligned} \tag{2.3}$$

where b is the distance between the plates and

$$X_p = \frac{(2p+1)\pi}{b}\left(\frac{R}{2k^2}\right)^{1/3} \quad \text{for} \quad p = 0,\ 1,\ 2,\ .... \tag{2.4}$$

The steady-state CSR in a rectangular toroidal chamber has also been intensively studied [55, 56, 57, 58], resulting in more complicated formulas.

The above equations are valid only when the magnets are long enough, i.e. $L_b \gg (R^2/k)^{1/3}$. In this case, the transient effects at the entrance and exit of the magnets are negligible [59]. For magnets with finite length, studies showed that the transient effect can be significant [60, 61].

For a three-dimensional (3D) bunched beam, in principle both transverse and longitudinal wake forces depend on the spatial distribution of the charged particles. The transverse effects were studied in Refs. [62, 63]. If the bunch is thin enough and the typical transverse beam size $\sigma_\perp$ satisfies the condition as follows

$$\sigma_\perp \ll \left(R\sigma_z^2\right)^{1/3}, \tag{2.5}$$

the bunch can be assumed to have line charge distribution along the longitudinal direction. Consequently, the effect of transverse beam size on the longitudinal wake fields is negligible [64].

In linac based X-ray Free Electron Lasers (FELs), the CSR forces can be very strong at very short bunch lengths. Extremely short bunches are usually achieved by passing them through magnet chicanes. The principle behind it is that particles with different energies have different path lengths when their orbits are bended. Then a bunch with energy distribution correlated to longitudinal positions can be compressed. The longitudinal CSR forces can lead to significant energy modulations along the bunch and consequently cause transverse emittance growth. In the case of low beam energy, space-charge forces also play a significant role. One usually starts from the retarded potentials Eqs. (1.51) and (1.52) to calculate the self-interaction of bunched particles along a curved orbit [65, 66, 67]. In the ultra-relativistic limit, the most popular 1D model for the CSR wake potential per unit length in a bending magnet is [60]

$$\frac{\partial W_{\parallel b}(z,s)}{\partial s} = T_1(z,R,s) + T_2(z,R,s), \tag{2.6}$$

where R is the bending radius, s is the orbit distance from the entrance of the magnet and z is the position within the bunch. The form of the above equation has been modified according to the notations of this thesis. The quantities T_1 and T_2 represent the main part of CSR fields and the transient part at the entrance, respectively. They are defined by

$$T_1(z,R,s) = K\int_{z-z_L}^{z} \frac{d\lambda(z')}{dz'}\left(\frac{1}{z-z'}\right)^{1/3} dz', \tag{2.7a}$$

$$T_2(z,R,s) = K\frac{\lambda(z-z_L)-\lambda(z-4z_L)}{z_L^{1/3}}, \tag{2.7b}$$

where $\lambda(z')$ is the linear charge density, $z_L(R,s) = s^3/(24R^2)$ is the slippage length and the parameter K is defined as follows

$$K(R) = -\frac{1}{4\pi\epsilon_0}\frac{2}{(3R^2)^{1/3}}. \tag{2.8}$$

The CSR fields in the drift space was recognized to be as important as that inside the magnet, especially in cases of short magnet [36]. One model for the drift CSR is given by [61]

$$\frac{\partial W_{\|d}(z,s)}{\partial s} = T_3(z,R,s) + T_4(z,R,s), \tag{2.9}$$

with s defined as the distance from the witness point to the exit of the magnet along the beam orbit. The quantities T_3 and T_4 are defined as follows

$$T_3(z,R,s) = -\frac{1}{\pi\epsilon_0}\frac{1}{L_b+2s}\lambda\left(z - \frac{L_b^2}{6R^2}(L_b+3s)\right), \tag{2.10a}$$

$$T_4(z,R,s) = \frac{1}{\pi\epsilon_0}\left[\frac{\lambda(z-\Delta z_{max})}{L_b+2s} + \int_{z-\Delta z_{max}}^{z}\frac{1}{s'+2s}\frac{d\lambda(z')}{dz'}dz'\right], \tag{2.10b}$$

where L_b is the magnet length measured along the beam orbit. The quantity s' is determined by the relation of

$$z - z' = \frac{1}{24R^2}s'^3\frac{s'+4s}{s'+s}, \tag{2.11}$$

with the explicit solution of

$$\begin{aligned} s' = &-s + \frac{1}{2}\sqrt{4s^2 + Y^{1/3}(Y-16s^3)^{1/3}} \\ &+ \frac{1}{2}\sqrt{8s^2 - Y^{1/3}(Y-16s^3)^{1/3} + \frac{2Y-16s^3}{\sqrt{4s^2+Y^{1/3}(Y-16s^3)^{1/3}}}} \end{aligned} \tag{2.12}$$

and $Y = 24R^2(z-z')$. The quantity Δz_{max} is defined by

$$\Delta z_{max} = \frac{L_b^3}{24R^2}\frac{L_b+4s}{L_b+s} \tag{2.13}$$

due to the restriction of $s' \le L_b$.

CSR fields may interfere with each other along a series of bending magnets. In such cases, one-dimensional time-domain method has also been investigated effectively in the linacs [36, 39, 40]. But due to the difficulties in modeling the full

chamber, usually parallel-plates model was used to address the shielding effect of the chamber walls.

In electron storage rings, the bunch length is usually in the order of a few millimeters, or down to sub-millimeters for dedicated THz radiation sources. In this case, impedance is good enough for studying single bunch instabilities. For a single bending magnet with beam chamber, up to now only numerical methods are available [26, 27, 43, 44]. Stupakov and Agoh have developed two different frequency-domain methods to calculate the CSR impedance of a single magnet [44, 58]. They studied the features of CSR wakes, rather than impedance, by changing the profile of the chamber. Starting with the same wave equation, a time-domain integration method was developed in Ref. [43] to calculate CSR wake fields with space-charge included. Unlike treatments in linacs, interference effects are usually neglected in studying CSR induced instabilities in storage rings.

There exists another kind of multi-bunch interference in CSR fields generated by a train of bunches. The bunch train pass through a bending magnet following the same trajectory, and was first observed in Ref. [68]. This kind of interference will not cause single-bunch instability and is beyond the scope of this thesis.

This chapter follows the method described in Ref. [26] to calculate CSR generated by a beam moving along an arbitrary trajectory. The beam trajectory can be generated by a single bending magnet (see Fig. 2.1), a series of bending magnets, or by an undulator or a wiggler (see Fig. 2.2). At present, the chamber is assumed to have uniform rectangular cross-section along the beam trajectory. To close the problem, two long straight sections are added before the entrance and after the exit of the chamber. Investigations to be done are as follows: 1) the features of CSR impedance and profiles of the radiation fields; 2) the CSR impedance of several bending magnets; 3) the CSR impedance of a wiggler.

First the field equations of CSR are formulated in Section 2.2. In Section 2.3, it is the problem statement to be solved in numerical calculations: parabolic equations with variant bending radius, including boundary conditions. The numerical schemes are described in Section 2.4. Numerous examples of CSR impedance calculations are presented in Section 2.5.

2.2 Field theory

In Chapter 1, the discussions are almost based on Cartesian coordinate systems. Unfortunately, the CSR problem is not well adapted to a solution in Cartesian coordinates because of the curved beam trajectory. To study CSR, it is convenient to move to the Frenet-Serret (F-S) coordinate system which is popular in accelerator physics. The F-S frame sets up an orthogonal coordinate system in the neighborhood of the beam trajectory. The field theory for CSR will be derived first based on the general theory introduced in Chapter 1.

In F-S system, the three curvilinear coordinates are (x, y, s), where s is the length measured along the beam trajectory from a reference initial point. Assuming that the beam trajectory is curved in the horizontal plane, the beam trajectory can be defined by a factor as follows

$$g(x, s) = 1 + \frac{x}{R(s)}, \tag{2.14}$$

where $R(s)$ defines the radius of the curvature and x denotes the displacement from the center of beam trajectory. Note that $R(s)$ is an arbitrary function of s in our framework.

It is natural to start from the Maxwell's equations in the frequency domain with charge and current sources included

$$\nabla \times \vec{E} = i\omega \vec{B}, \tag{2.15a}$$

$$\nabla \times \vec{B} + \frac{i\omega}{c^2}\vec{E} = \mu_0 \vec{J}, \tag{2.15b}$$

$$\nabla \cdot \vec{B} = 0, \tag{2.15c}$$

$$\nabla \cdot \vec{E} = \frac{\rho}{\epsilon_0}, \tag{2.15d}$$

$$\nabla \cdot \vec{J} = i\omega\rho. \tag{2.15e}$$

If there is no sources, i.e. $\rho = 0$ and $\vec{J} = 0$, the above equations describe the electromagnetic waves propagating in the region to be examined. There is a monograph by Lewin, Chang and Kuester [69] on the theories of electromagnetic waves in curved structures.

The first price to be paid for using F-S system is that the expressions for gradient, divergence, or curl exhibit not as simple forms as those in Cartesian coordinate systems (for instance, see Chapter 1 of Ref. [70]). It follows from Eq. (2.15a) that

$$\frac{1}{g}\left(g\frac{\partial E_s}{\partial y}-\frac{\partial E_y}{\partial s}\right)-i\omega B_x=0, \tag{2.16a}$$

$$\frac{1}{g}\left[\frac{\partial E_x}{\partial s}-\frac{\partial}{\partial x}(gE_s)\right]-i\omega B_y=0, \tag{2.16b}$$

$$\frac{\partial E_y}{\partial x}-\frac{\partial E_x}{\partial y}-i\omega B_s=0, \tag{2.16c}$$

and from Eq. (2.15b) that

$$\frac{1}{g}\left(g\frac{\partial B_s}{\partial y}-\frac{\partial B_y}{\partial s}\right)+\frac{i\omega}{c^2}E_x=0, \tag{2.17a}$$

$$\frac{1}{g}\left[\frac{\partial B_x}{\partial s}-\frac{\partial}{\partial x}(gB_s)\right]+\frac{i\omega}{c^2}E_y=0, \tag{2.17b}$$

$$\frac{\partial B_y}{\partial x}-\frac{\partial B_x}{\partial y}+\frac{i\omega}{c^2}E_s=\mu_0 J_s. \tag{2.17c}$$

As derived in Eq. (1.45), it has been assumed that the source current takes the form of

$$\vec{J}(\vec{r},\omega)=\vec{i}_s J_s(\vec{r},\omega)=\vec{i}_s q\sigma(x,y)e^{i\omega s/v}, \tag{2.18}$$

where $\vec{i}_s$ denotes the unit vector tangent to the beam trajectory. Namely, the current density only have component in the s-direction. It is noteworthy that the rigid-beam approximation has also been applied in the present discussions. From Eq. (2.15e), the charge density is calculated as follows

$$\rho(\vec{r},\omega)=\frac{q}{gv}\sigma(x,y)e^{i\omega s/v}. \tag{2.19}$$

The factor of $1/g$ appears in the above equation due to the choice of F-S coordinate system, and it makes the form of charge density to slightly differ from Eq. (1.44).

The fields of $(\vec{E},\vec{B})$ can be replaced by $(\vec{\mathbb{E}},\vec{\mathbb{B}})e^{i\omega s/v}$ as what is done in subsection 1.2.4. Then a new set of equations is obtained as follows

$$\frac{1}{g}\left(g\frac{\partial \mathbb{E}_s}{\partial y}-\frac{\partial \mathbb{E}_y}{\partial s}-\frac{i\omega}{v}\mathbb{E}_y\right)-i\omega\mathbb{B}_x=0, \tag{2.20a}$$

$$\frac{1}{g}\left[\frac{\partial \mathbb{E}_x}{\partial s}+\frac{i\omega}{v}\mathbb{E}_x-\frac{\partial}{\partial x}(g\mathbb{E}_s)\right]-i\omega\mathbb{B}_y=0, \tag{2.20b}$$

$$\frac{\partial \mathbb{E}_y}{\partial x}-\frac{\partial \mathbb{E}_x}{\partial y}-i\omega\mathbb{B}_s=0, \tag{2.20c}$$

and

$$\frac{1}{g}\left(g\frac{\partial \mathbb{B}_s}{\partial y}-\frac{\partial \mathbb{B}_y}{\partial s}-\frac{i\omega}{v}\mathbb{B}_y\right)+\frac{i\omega}{c^2}\mathbb{E}_x=0, \tag{2.21a}$$

$$\frac{1}{g}\left[\frac{\partial \mathbb{B}_x}{\partial s}+\frac{i\omega}{v}\mathbb{B}_x-\frac{\partial}{\partial x}(g\mathbb{B}_s)\right]+\frac{i\omega}{c^2}\mathbb{E}_y=0, \tag{2.21b}$$

$$\frac{\partial \mathbb{B}_y}{\partial x}-\frac{\partial \mathbb{B}_x}{\partial y}+\frac{i\omega}{c^2}\mathbb{E}_s=\mu_0 q\sigma. \tag{2.21c}$$

It is obvious that Eqs. (2.20) and (2.21) give a set of first order, coupled partial differential equations for $\vec{\mathbb{E}}$ and $\vec{\mathbb{B}}$

$$\frac{\partial \mathbb{E}_y}{\partial s}=g\frac{\partial \mathbb{E}_s}{\partial y}-\frac{i\omega}{v}\mathbb{E}_y-i\omega g\mathbb{B}_x, \tag{2.22a}$$

$$\frac{\partial \mathbb{E}_x}{\partial s}=-\frac{i\omega}{v}\mathbb{E}_x+\frac{\partial}{\partial x}(g\mathbb{E}_s)+i\omega g\mathbb{B}_y, \tag{2.22b}$$

$$\mathbb{B}_s=\frac{1}{i\omega}\left(\frac{\partial \mathbb{E}_y}{\partial x}-\frac{\partial \mathbb{E}_x}{\partial y}\right), \tag{2.22c}$$

and

$$\frac{\partial \mathbb{B}_y}{\partial s}=g\frac{\partial \mathbb{B}_s}{\partial y}-\frac{i\omega}{v}\mathbb{B}_y+\frac{i\omega g}{c^2}\mathbb{E}_x, \tag{2.23a}$$

$$\frac{\partial \mathbb{B}_x}{\partial s}=-\frac{i\omega}{v}\mathbb{B}_x+\frac{\partial}{\partial x}(g\mathbb{B}_s)-\frac{i\omega g}{c^2}\mathbb{E}_y, \tag{2.23b}$$

$$\mathbb{E}_s=-\frac{c^2}{i\omega}\left(\frac{\partial \mathbb{B}_y}{\partial x}-\frac{\partial \mathbb{B}_x}{\partial y}-\mu_0 q\sigma\right). \tag{2.23c}$$

It would be interesting if the above equations are numerically soluble. But practically, there are challenges associated with decreasing the mesh sizes required by numerical stability conditions, which demands that the mesh sizes should be inversely proportional to the frequency [26]. Efforts have been made to simplify the Maxwell's equations and hence reduce the complexity of solving field equations. The most significant of these is the paraxial approximation of Maxwell's equations which has been proved to be very successful in CSR theory [26, 71]. The parabolic equations of CSR theory resulted from paraxial approximation are re-derived using our notations in the followings.

Firstly, the Maxwell's equations can be uncoupled and it reduces the equations to second-order partial differential equations of electric fields. With $k = \omega/c$, the results are

$$\frac{\partial^2 \mathbb{E}_x}{\partial x^2} + \frac{\partial^2 \mathbb{E}_x}{\partial y^2} + \frac{1}{g^2}\frac{\partial^2 \mathbb{E}_x}{\partial s^2} + \left[(1 - \frac{1}{\beta^2 g^2})k^2 - \frac{1}{R^2 g^2} - \frac{ik}{\beta g^3}\frac{\partial g}{\partial s}\right]\mathbb{E}_x + \frac{1}{Rg}\frac{\partial \mathbb{E}_x}{\partial x} + \left[\frac{2ik}{\beta g^2} - \frac{1}{g^3}\frac{\partial g}{\partial s}\right]\frac{\partial \mathbb{E}_x}{\partial s} - \frac{2}{Rg^2}\frac{\partial \mathbb{E}_s}{\partial s} + \left[\frac{1}{Rg^3}\frac{\partial g}{\partial s} - \frac{1}{g}\frac{d}{ds}\left(\frac{1}{R}\right) - \frac{2ik}{\beta Rg^2}\right]\mathbb{E}_s = \frac{q}{\epsilon_0 v}\frac{\partial}{\partial x}\left(\frac{\sigma}{g}\right), \tag{2.24a}$$

$$\frac{\partial^2 \mathbb{E}_y}{\partial x^2} + \frac{\partial^2 \mathbb{E}_y}{\partial y^2} + \frac{1}{g^2}\frac{\partial^2 \mathbb{E}_y}{\partial s^2} + \left[(1 - \frac{1}{\beta^2 g^2})k^2 - \frac{ik}{\beta g^3}\frac{\partial g}{\partial s}\right]\mathbb{E}_y + \frac{1}{Rg}\frac{\partial \mathbb{E}_y}{\partial x} + \left[\frac{2ik}{\beta g^2} - \frac{1}{g^3}\frac{\partial g}{\partial s}\right]\frac{\partial \mathbb{E}_y}{\partial s} = \frac{q}{\epsilon_0 v}\frac{\partial}{\partial y}\left(\frac{\sigma}{g}\right), \tag{2.24b}$$

$$\frac{\partial^2 \mathbb{E}_s}{\partial x^2} + \frac{\partial^2 \mathbb{E}_s}{\partial y^2} + \frac{1}{g^2}\frac{\partial^2 \mathbb{E}_s}{\partial s^2} + \left[(1 - \frac{1}{\beta^2 g^2})k^2 - \frac{1}{R^2 g^2} - \frac{ik}{\beta g^3}\frac{\partial g}{\partial s}\right]\mathbb{E}_s + \frac{1}{Rg}\frac{\partial \mathbb{E}_s}{\partial x} + \left[\frac{2ik}{\beta g^2} - \frac{1}{g^3}\frac{\partial g}{\partial s}\right]\frac{\partial \mathbb{E}_s}{\partial s} + \frac{2}{Rg^2}\frac{\partial \mathbb{E}_x}{\partial s} + \left[-\frac{1}{Rg^3}\frac{\partial g}{\partial s} + \frac{1}{g^2}\frac{d}{ds}\left(\frac{1}{R}\right) + \frac{2ik}{\beta Rg^2}\right]\mathbb{E}_x = \frac{ikq\sigma}{\epsilon_0 c}\left(\frac{1}{\beta^2 g^2} - 1\right) + \frac{q\sigma}{\epsilon_0 \beta g c}\frac{\partial}{\partial s}\left(\frac{1}{g}\right). \tag{2.24c}$$

The above equations exactly describe the CSR field evolutions with relativistic effect taken into account. It is interesting that $\mathbb{E}_y$ does not enter Eqs. (2.24a) and (2.24c) explicitly. But $\mathbb{E}_y$ does couple with $\mathbb{E}_x$ and $\mathbb{E}_s$ through the boundary conditions. As discussed in Ref. [26], when paraxial approximation is applied to Eqs. (2.24), the terms of second-order derivative over s are dropped and then a set of first-order field evolution equations is deduced. This set of equations is soluble and has been studied by Oide [72, 73]. If only the dominant terms due to curvature and space-charge effect are considered, one can obtain a much simpler parabolic equation as follows

$$\frac{\partial \vec{\mathbb{E}}_\perp}{\partial s} = \frac{i}{2k}\left[\nabla_\perp^2 \vec{\mathbb{E}}_\perp - \frac{q}{\epsilon_0 c}\nabla_\perp \sigma + 2k^2\left(\frac{x}{R(s)} - \frac{1}{2\gamma^2}\right)\vec{\mathbb{E}}_\perp\right]. \tag{2.25}$$

In the above equation, the term including x/R represents the dominant effect of the curved orbit, and the term with $1/\gamma^2$ involved denotes the dominant part

of space-charge effects. And the transverse distribution $\sigma(x, y)$ is assumed to concentrate on a small area around the origin of the coordinate system.

The parabolic equation simplified from the wave equations has tremendous applications in various areas. In cases of only fields in the paraxial direction are interesting, the parabolic approximation can be introduced to simplify the wave propagation problems. There is a monograph by Levy [74] on its applications for electromagnetic wave propagations. Equation (2.25) is one form of parabolic equation suitable for calculating CSR. Applying the parabolic equation to calculation of high-frequency beam impedance was reviewed in Ref. [75].

2.3 Formalism for numerical calculations of longitudinal CSR impedance

Starting from this section, Roman letters will be used in notations of field and beam quantities for sake of convenience, instead of blackboard bold letters used in the previous sections. The readers can refer to the fundamental theories described in Chapter 1 and find the original definitions of the quantities concerned.

2.3.1 Parabolic differential equation

Taking ultra-relativistic limit in Eq. (2.25), the parabolic equation is reduced to

$$\frac{\partial \vec{E}_\perp}{\partial s} = \frac{i}{2k}\left(\nabla_\perp^2 \vec{E}_\perp - \frac{1}{\epsilon_0}\nabla_\perp \rho_0 + \frac{2k^2 x}{R(s)}\vec{E}_\perp\right), \tag{2.26}$$

where $\vec{E}_\perp$ is the complex amplitude of the transverse electric field, and $R(s)$ is the s-dependent bending radius along the beam orbit. The origin of the coordinate system is located on the beam trajectory. Regarding to the beam, the charge density $\rho_0 = q\sigma/c$ is assumed to be rigid, i.e. ρ_0 does not vary along s.

With paraxial approximation, the complex amplitude of longitudinal electric field is a byproduct of the transverse fields and approximated as,

$$E_s = \frac{i}{k}\left(\nabla_\perp \cdot \vec{E}_\perp - \mu_0 c J_s\right), \tag{2.27}$$

where μ_0 is the vacuum permeability, c is the speed of light in vacuum, and $J_s = \rho_0 c$ is the current density. The detailed derivation of the above equations can be found in Refs. [26, 71]. The validity of these equations will not be discussed because it has been well addressed in Refs. [44, 58].

Equation (2.26) also describes the evolution of the fields in a straight chamber where the inverse bending radius is zero

$$\frac{\partial \vec{E}_\perp}{\partial s} = \frac{i}{2k}\left(\nabla_\perp^2 \vec{E}_\perp - \frac{1}{\epsilon_0}\nabla_\perp \rho_0\right). \tag{2.28}$$

In our calculations, the beam has a form of point charge in the longitudinal direction and Gaussian distribution in the transverse directions. Then the longitudinal impedance is calculated by directly integrating E_s over s

$$Z(k) = -\frac{1}{q}\int_0^\infty E_s(x_c, y_c) ds \tag{2.29}$$

where (x_c, y_c) denotes the center of the beam in the transverse $x-y$ plane. The appearance of the minus sign in Eq. (2.29) is due to the convention of the beam instability formalism.

2.3.2 Geometry of the beam chamber

The geometry of the problem is illustrated in Figs. 2.1 and 2.2. A ultra-relativistic beam traverses an infinitely long straight chamber, which is not plotted in the figures, and then enters a section of curved chamber. After passing a finite distance, the beam exits the curved chamber and enters another infinite long straight one. All these chambers are under vacuum and have rectangular and uniform cross-section along the beam orbit. Meanwhile, the walls of the chambers are perfectly conducting and are always parallel to the beam orbit. This is quite essential in simplifying the boundary conditions for the field equations and consequently reduces the problem to a 2D one when the equation is solved numerically.

The curved chamber can occur in a single dipole magnet (see Fig. 2.1), or in a series of bending magnets with straight drift chambers between them. A wiggler is equivalent to a series of bending magnets with a sinusoidal field profile. Usually the chamber for a wiggler is flat and straight along the beam orbit. But for the

case of a weak wiggler with a small wiggler parameter $K/\gamma \ll 1$, the chamber can be approximated by a curved one (see Fig. 2.2). Thus a weak wiggler can also be the subject of our study.

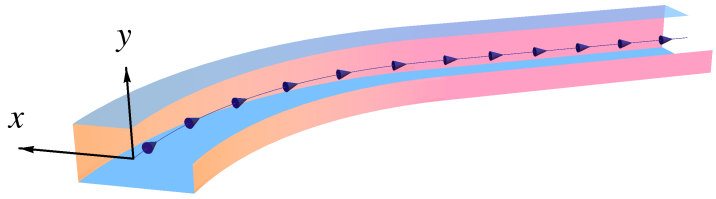

Figure 2.1: The geometry of the curved chamber for a single bending magnet. An infinitely long straight chamber is connected after the exit of the curved chamber. The beam moves along the curved line with arrows. The origin of the coordinate system coincides with the beam orbit.

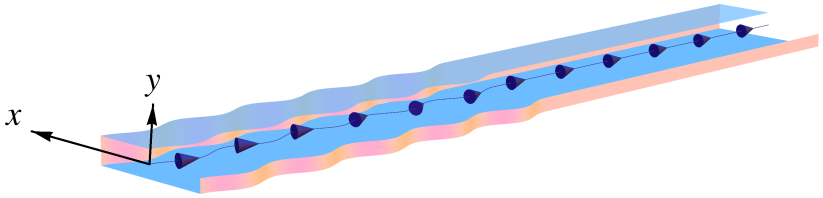

Figure 2.2: The geometry of the curved chamber for a wiggler. An infinitely long straight chamber is connected after the exit of the curved chamber. The beam moves along the curved line with arrows. The origin of the coordinate system coincides with the beam orbit.

In our framework, the origin of the curvilinear coordinate system x, y and s coincides with the beam orbit and the beam position in $x-y$ plane (x_c, y_c) does not vary with s. The curvature of the beam orbit $R^{-1}(s)$ can be an arbitrarily real function of s. Though this assumption has already been included in Agoh and Yokoya's method [26], its effect has not been well investigated yet. Furthermore, $R(s)$ does not depend on x or y and it is no matter for $R(s)$ to be positive or

negative. For a single bending magnet or a series of bending magnets with hard-edge field profile, $R^{-1}(s)$ can be represented by a step function. For a wiggler, $R^{-1}(s)$ can be expressed as a cosine function

$$R^{-1}(s) = R_0^{-1}\cos(k_w s), \tag{2.30}$$

where R_0^{-1} is the maximum curvature and k_w is the wavenumber of the wiggler field.

2.3.3 Field separation

For a point charge the term of ρ_0 on the right hand side (RHS) of Eq. (2.26) is singular. The approach of field separation, which has been used in Refs. [26, 60], was adopted to remove this singularity in numerical solution. The total field is separated into two parts: the beam field in free space $\vec{E}_\perp^b$ and the radiation field $\vec{E}_\perp^r$. For an ultra-relativistic beam, the beam field is transverse to the beam orbit and is independent of s. $E_\perp^b$ satisfies Poisson's equation

$$\nabla_\perp^2 \vec{E}_\perp^b = \frac{1}{\epsilon_0}\nabla_\perp \rho_0. \tag{2.31}$$

Then the evolution equation for the radiation field can be written in the form of

$$\frac{\partial \vec{E}_\perp^r}{\partial s} = \frac{i}{2k}\left[\nabla_\perp^2 \vec{E}_\perp^r + \frac{2k^2 x}{R(s)}\left(\vec{E}_\perp^r + \vec{E}_\perp^b\right)\right]. \tag{2.32}$$

Similarly, for the field in the straight chamber, there is

$$\frac{\partial \vec{E}_\perp^r}{\partial s} = \frac{i}{2k}\nabla_\perp^2 \vec{E}_\perp^r. \tag{2.33}$$

In the following of this chapter, the quantity $\vec{E}_\perp^r$ is always taken as radiation field and no difference is identified between the fields in the straight section and in the curved section. With assumption of ultra-relativistic beam, the beam field in free space does not contribute to E_s, so Eq. (2.27) is equivalent to [26]

$$E_s = \frac{i}{k}\nabla_\perp \cdot \vec{E}_\perp^r. \tag{2.34}$$

In our calculations, the beam is assumed to have a small transverse size with rms values σ_x and σ_y in horizontal and vertical directions, respectively. The distribution function is bi-Gaussian as follows

$$\rho_0(x,y,k) = \frac{q\lambda(k)}{2\pi c\sigma_x\sigma_y} e^{-\frac{x^2}{2\sigma_x^2}-\frac{y^2}{2\sigma_y^2}}, \tag{2.35}$$

where q is the total charge of the beam and $\lambda(k)$ indicates the beam spectrum in the longitudinal direction. In practical calculations, it is assumed that $\lambda(k) = 1$ and $q = 1C$. The typical values of σ_x and σ_y are set to be 0.1 mm and 0.01 mm. With such small beam sizes, the beam field is still well concentrated in the vicinity of beam center. But it will not cause problem in numerical calculations, because the sharp peak of $E_\perp^b$ will be smoothed out by multiplying a small value of x in Eq. (2.32).

It is obvious that if the beam moves along a straight orbit in the free space with constant velocity, there would be no radiation field, i.e. $E_\perp^r = 0$. So $E_\perp^r$ quite depends on the shielding of the chamber and also on the curvature of the beam orbit. Thus, separating the beam field in free space from the total field provides us the convenience of examining the properties of the radiation field $E_\perp^r$ in a chamber. On the other hand, $E_\perp^r$ can be expanded into the sum of the eigenmodes of the beam chamber [44, 71]. If any mode is excited and dominates the CSR field, it should be reflected in the profile of $E_\perp^r$. This will be addressed again in Section 2.5.

The electric field and electric potential generated by a bi-Gaussian beam can be analytically obtained or calculated using numerical integrations. With bi-Gaussian distribution and assumed $\sigma_x > \sigma_y$, the solution of Eq. (2.31) in free space can be expressed using Bassetti-Erskine formula [76]

$$E_x^b(x,y) = \frac{q\lambda(k)}{2c\epsilon_0\sqrt{2\pi(\sigma_x^2-\sigma_y^2)}}\text{Im.}\left[\Lambda(x,y)\right], \tag{2.36a}$$

$$E_y^b(x,y) = \frac{q\lambda(k)}{2c\epsilon_0\sqrt{2\pi(\sigma_x^2-\sigma_y^2)}}\text{Re.}\left[\Lambda(x,y)\right], \tag{2.36b}$$

where

$$\Lambda(x,y) = w\left(\frac{x+iy}{\sqrt{2(\sigma_x^2-\sigma_y^2)}}\right) - e^{-\frac{x^2}{2\sigma_x^2}-\frac{y^2}{2\sigma_y^2}} w\left(\frac{\frac{\sigma_y}{\sigma_x}x + i\frac{\sigma_x}{\sigma_y}y}{\sqrt{2(\sigma_x^2-\sigma_y^2)}}\right), \tag{2.37a}$$

$$w(z) = e^{-z^2}\left(1 + \frac{2i}{\sqrt{\pi}}\int_0^z e^{t^2}dt\right), \tag{2.37b}$$

where $w(z)$ is so-called the complex error function. There is subtlety of numerical evaluations of $w(z)$ [77]. For large values of imaginary part of z, $w(z)$ grows exponentially. This problem can be resolved by rewriting the expression of $\Lambda(x, y)$ as

$$\Lambda(x, -y) = -\Lambda^*(x, y), \tag{2.38}$$

where the superscript * indicates taking the complex conjugate of the quantity considered. In the case of $\sigma_x = \sigma_y = \sigma$, the field distribution is much simplified [78]

$$E_x^b(x, y) = \frac{q\lambda(k)}{2\pi c\epsilon_0}\frac{x}{x^2 + y^2}\left(1 - e^{-\frac{x^2+y^2}{2\sigma^2}}\right), \tag{2.39}$$

$$E_y^b(x, y) = \frac{q\lambda(k)}{2\pi c\epsilon_0}\frac{y}{x^2 + y^2}\left(1 - e^{-\frac{x^2+y^2}{2\sigma^2}}\right). \tag{2.40}$$

The electric potential of elliptic bi-Gaussian beam in free space can be also calculated by [79]

$$\phi^b(x, y) = \frac{\lambda(k)}{2\pi c\epsilon_0}\int_r^1 \frac{e^{-(1-t^2)(A+\frac{B}{t^2})} - 1}{1 - t^2}dt, \tag{2.41}$$

where it is assumed that $\sigma_x > \sigma_y$ and

$$A(x) = \frac{x^2}{2(\sigma_x^2 - \sigma_y^2)}, \tag{2.42a}$$

$$B(y) = \frac{y^2}{2(\sigma_x^2 - \sigma_y^2)}, \tag{2.42b}$$

$$r = \frac{\sigma_y}{\sigma_x}. \tag{2.42c}$$

When $\sigma_x = \sigma_y = \sigma$, the electric potential is given by [79]

$$\phi^b(x, y) = \frac{\lambda(k)}{4\pi c\epsilon_0}\int_0^{\frac{1}{2\sigma^2}} \frac{e^{-(x^2+y^2)t} - 1}{t}\, dt. \tag{2.43}$$

2.3.4 Initial conditions

The fields before the entrance of the curved chamber, which is denoted as $s = 0$, are given by the steady-state Coulomb field of the relativistic beam established in the straight chamber and provide the initial conditions for Eq. (2.26).

The Poisson's equation of electric field is not easy to solve in a discretized version. By defining $\vec{E}_\perp = -\nabla\phi$, Equation (2.28) can be transferred to the Poisson's equation of the electric potential

$$\nabla^2\phi = -\frac{\rho_0}{\epsilon_0}. \tag{2.44}$$

Again, the electric potential is splitted into two parts:

$$\phi = \phi^r + \phi^b, \tag{2.45}$$

where ϕ^b denotes the electric potential of the beam in free space. The part ϕ^r is the remaining potential caused by the boundaries and satisfies the Laplace's equation

$$\nabla^2\phi^r = 0. \tag{2.46}$$

The total electric potential on the perfect conducting walls is equal to zero, i.e. $\phi|_s = 0$. It results in the boundary condition for ϕ^r

$$\phi^r|_s = -\phi^b|_s, \tag{2.47}$$

where $\phi^b|_s$ is given by Eq. (2.41). The system of Eq. (2.46) with boundary condtion Eq. (2.47) can be solved using standard iterative methods [80].

2.3.5 Boundary conditions

The boundary conditions appropriate for a perfectly conducting surface is that the tangential components of the electric fields vanish. In our problem, the boundary conditions are

$$\vec{n} \times \vec{E}_\perp|_s = 0, \tag{2.48a}$$

$$E_s|_s = 0, \tag{2.48b}$$

where $\vec{n}$ is the unit vector normal to the chamber wall surface. And Eq. (2.48) is valid for both curved part and straight parts of the beam chamber.

With the rectangular cross-section, the explicit forms of Eq. (2.48a), for the south and north walls in the $x-y$ plane (see Fig. 2.3), are written as

$$E_x^r|_s = -E_x^b|_s, \tag{2.49}$$

and for the east and west walls

$$E_y^r|_r = -E_y^b|_s. \tag{2.50}$$

The explicit form of Eq. (2.48b) can be derived from Eqs. (2.34), (2.49), and (2.50). The results are for the south and north walls

$$\left.\frac{\partial E_y^r}{\partial y}\right|_s = \left.\frac{\partial E_x^b}{\partial x}\right|_s, \tag{2.51}$$

and for the east and west walls

$$\left.\frac{\partial E_x^r}{\partial x}\right|_s = \left.\frac{\partial E_y^b}{\partial y}\right|_s, \tag{2.52}$$

respectively. It is noteworthy that the paraxial approximation has been utilized in obtaining Eqs. (2.51) and (2.52). Though the free-space beam field vanishes in the vicinity of the chamber walls, the RHS of Eqs. (2.51) and (2.52) are not necessarily to be zero. It needs to be emphasized that the above boundary conditions are Maxwellian and are important in preserving the field and avoiding numerical damping when solving the discretized version of Eq. (2.32).

2.3.6 Field in the straight chamber

The evolution equation of the radiation field in the straight chamber is Eq. (2.33). It is easy to solve it using mode expansion method [44, 78]. The results are

$$E_x^r(x,y,s,k) = \sum_{m=0}^{\infty}\sum_{p=1}^{\infty} A_{mp}\cos\left(k_x(x+x_c)\right)\sin\left(k_y(y+y_c)\right)e^{-\Gamma_{mp}(s-s_0)}, \tag{2.53a}$$

$$E_y^r(x,y,s,k) = \sum_{m=1}^{\infty}\sum_{p=0}^{\infty} B_{mp}\sin\left(k_x(x+x_c)\right)\cos\left(k_y(y+y_c)\right)e^{-\Gamma_{mp}(s-s_0)}, \tag{2.53b}$$

where $k_x = \frac{m\pi}{a}$ and $k_y = \frac{p\pi}{b}$. In this case, even the finite conductivity of the chamber wall can be considered and it results in an additional attenuation constant in the formulations. The propagation constant is defined as

$$\Gamma_{mp} = \alpha_{mp} + i\beta_{mp}, \tag{2.54}$$

where the attenuation constant α_{mp} and the phase constant β_{mp} are real values. With perfectly conducting walls, $\alpha_{mp} = 0$ and

$$\beta_{mp} = \frac{k_c^2}{2k}, \tag{2.55}$$

where k_c is the cutoff frequency of the waveguide

$$k_c = \sqrt{k_x^2 + k_y^2}. \tag{2.56}$$

When considering the finite conductivity of the guide walls and assuming $k \gg k_c$, α_{mp} can be approximated by [6]

$$\alpha_{mp} = \frac{2R_n}{bZ_0} \frac{m^2b^3 + p^2a^3}{m^2b^2a + p^2a^3}, \tag{2.57}$$

where $Z_0 = 376.7\ \Omega$ is the impedance of free space and

$$R_n = \sqrt{\frac{kc\mu_0}{2\sigma_c}} \tag{2.58}$$

is the skin-effect surface resistance of the metal with conductivity σ_c. The quantities A_{mp} and B_{mp} denote the amplitudes which can be determined by the initial conditions. Suppose at $s = s_0$, for instance at the exit of the curved chamber, the field is known. Then the amplitude parameters can be calculated as follows

$$A_{mp} = \frac{4}{ab(1+\delta_{m0})} \int_0^a dx \int_0^b dy E_x^r(x, y, s_0, k) \cos\left(k_x(x + x_c)\right) \sin\left(k_y(y + y_c)\right), \tag{2.59a}$$

$$B_{mp} = \frac{4}{ab(1+\delta_{n0})} \int_0^a dx \int_0^b dy E_y^r(x, y, s_0, k) \sin\left(k_x(x + x_c)\right) \cos\left(k_y(y + y_c)\right), \tag{2.59b}$$

where δ_{m0} is the Kronecker delta function. With A_{mp} and B_{mp} known, one can apply Eq. (2.53) to Eq. (2.34) and get

$$E_s(x, y, s, k) = -\frac{i}{k} \sum_{m=1}^{\infty} \sum_{p=1}^{\infty} C_{mp} \sin\left(k_x(x + x_c)\right) \sin\left(k_y(y + y_c)\right) e^{-\Gamma_{mp}(s-s_0)}, \tag{2.60}$$

where

$$C_{mp} = A_{mp}k_x + B_{mp}k_y. \tag{2.61}$$

Integrating E_s over s is straightforward

$$\int_{s_0}^{s_1} E_s(x, y, s, k)ds = \frac{i}{k}\sum_{m=1}^{\infty}\sum_{p=1}^{\infty} D_{mp}\sin\left(k_x(x + x_c)\right)\sin\left(k_y(y + y_c)\right), \tag{2.62}$$

where

$$D_{mp} = \frac{C_{mp}}{\Gamma_{mp}}\left(e^{-\Gamma_{mp}(s_1 - s_0)} - 1\right). \tag{2.63}$$

To integrate the field along an infinitely long chamber, it is necessary to set $s_1 = \infty$. Then D_{mp} converges to

$$D_{mp}|_{s_1\to\infty} = -\frac{C_{mp}}{\Gamma_{mp}}. \tag{2.64}$$

The attenuation length of a specific mode is equal to $1/\alpha_{mp}$. It is necessary to emphasize that the attenuation length of a propagating mode which is well above cutoff (i.e. $k \gg k_c$) is usually very long. Suppose the material is copper with electrical conductivity $\sigma_c = 5.8 \times 10^7$ S/m. The attenuation length of a mode in a square chamber can be estimated using Eq. (2.57):

$$\frac{1}{\alpha_{mp}} \approx \frac{bZ_0}{2R_n}. \tag{2.65}$$

Suppose that the interested highest wavenumber is $k = 10$ mm^{-1} and the chamber dimensions are $a = b = 2$ cm, Equation (2.65) gives an attenuation length of around 21 meters. Thus it can be fairly concluded that the field attenuation between two consecutive bending magnets is negligible, as far as length of the straight pipe between them is much smaller than the attenuation length.

In order to close the problem completely, the integration of the radiation field in the limit $s \to \infty$, i.e. Eq. (2.29) must be done properly, and this is shown in Eq. (2.62).

2.4 Finite difference technique

The numerical algorithms adopted here are adapted from the mesh methods originally proposed in Ref. [26]. For completeness, they are discussed in more detail

in this section. Of particular emphasis are some aspects which were not well discussed in Refs. [26, 78].

We start by dividing the rectangular domain in the $x-y$ plane into an equidistant $M \times N$ mesh with step sizes $\Delta x = a/M$ and $\Delta y = b/N$ in the x and y directions, respectively. The grid is shown in the solid lines of Fig. 2.3. The grid points in the $x-y$ plane are given by

$$(i, j) = (i\Delta x - x_c, j\Delta y - y_c). \tag{2.66}$$

For any function of space and s, its value on the grid point of (i, j) is sampled as follows

$$F^n(i, j) = F(i\Delta x - x_c, j\Delta y - y_c, n\Delta s), \tag{2.67}$$

where Δs indicates the step size along s.

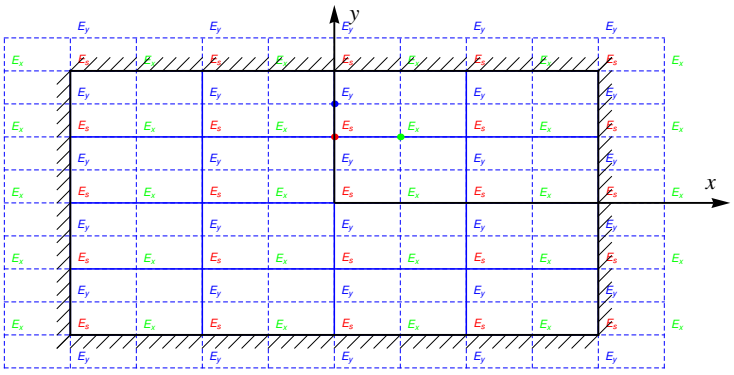

Figure 2.3: Staggered grid definition with ghost points outside the boundary of the chamber. The positions of various field components are shown. Constant spacing in the x and y directions is assumed.

The transverse electric fields are sampled by staggering the grid in half a cell in both x and y directions (see Fig. 2.3). The grid staggering provides the convenience of discretizing the field evolution equations [26]. Furthermore, it is also essential in removing the computational high-frequency modes in the finite difference formulation. The second-order derivative is approximated by central finite difference and the derivative with respect to s is approximated by the leapfrog difference. The leapfrog algorithm is fully explicit and conditionally stable. Though unconditionally stable implicit schemes are available (for instances,

see Refs. [81, 82, 83]) and allow for large step size Δs, they usually are more complex to program and require more computational efforts involved with matrix inversions in each solution step.

The grid in the $x-y$ plane, as shown in Fig. 2.3, does not vary along s because the chamber cross-section is uniform. The second-order central finite difference requires additional ghost points which are half cell outside the chamber wall surfaces.

A set of finite difference equations for Eq. (2.32) that will be found convenient for perfectly conducting boundary conditions is constructed as follows [26]. For E_x^r the discretized equation is

$$\begin{aligned}&\frac{E_x^{r,n+1}(i+\frac{1}{2},j)-E_x^{r,n-1}(i+\frac{1}{2},j)}{2\Delta s}\\&=\frac{i}{2k}\left(G_x^n(i+\frac{1}{2},j)+H_x^n(i+\frac{1}{2},j)+I_x^n(i+\frac{1}{2},j)\right),\end{aligned}\tag{2.68}$$

where

$$G_x^n(i+\frac{1}{2},j)=\frac{E_x^{r,n}(i+\frac{3}{2},j)-2E_x^{r,n}(i+\frac{1}{2},j)+E_x^{r,n}(i-\frac{1}{2},j)}{\Delta x^2},\tag{2.69}$$

$$H_x^n(i+\frac{1}{2},j)=\frac{E_x^{r,n}(i+\frac{1}{2},j+1)-2E_x^{r,n}(i+\frac{1}{2},j)+E_x^{r,n}(i+\frac{1}{2},j-1)}{\Delta y^2},\tag{2.70}$$

$$I_x^n(i+\frac{1}{2},j)=\frac{2k^2x(i+\frac{1}{2})}{R(n)}\left(E_x^{r,n}(i+\frac{1}{2},j)+E_x^{b,n}(i+\frac{1}{2},j)\right),\tag{2.71}$$

where $R(n)$ is the bending radius at $s=n\Delta s$.

For E_y^r, the discretized equation is

$$\begin{aligned}&\frac{E_y^{r,n+1}(i,j+\frac{1}{2})-E_y^{r,n-1}(i,j+\frac{1}{2})}{2\Delta s}\\&=\frac{i}{2k}\left(G_y^n(i,j+\frac{1}{2})+H_y^n(i,j+\frac{1}{2})+I_y^n(i,j+\frac{1}{2})\right),\end{aligned}\tag{2.72}$$

where

$$G_y^n(i,j+\frac{1}{2})=\frac{E_y^{r,n}(i+1,j+\frac{1}{2})-2E_y^{r,n}(i,j+\frac{1}{2})+E_y^{r,n}(i-1,j+\frac{1}{2})}{\Delta x^2},\tag{2.73}$$

$$H_y^n(i,j+\frac{1}{2})=\frac{E_y^{r,n}(i,j+\frac{3}{2})-2E_y^{r,n}(i,j+\frac{1}{2})+E_y^{r,n}(i,j-\frac{1}{2})}{\Delta y^2},\tag{2.74}$$

$$I_y^n(i,j+\frac{1}{2}) = \frac{2k^2x(i)}{R(n)}\left(E_y^{r,n}(i,j+\frac{1}{2}) + E_y^{b,n}(i,j+\frac{1}{2})\right). \tag{2.75}$$

It is noticed that the transverse fields are sampled by staggering the grid in half a cell in both x and y directions.

The boundary conditions on each wall surface are

$$E_y^r(j,N) = -E_y^b(j,N) \quad \text{for} \quad 0 \le j \le N, \tag{2.76a}$$

$$E_y^r(j,0) = -E_y^b(j,0) \quad \text{for} \quad 0 \le j \le N, \tag{2.76b}$$

$$E_x^r(i,0) = -E_x^b(i,0) \quad \text{for} \quad 0 \le i \le M, \tag{2.76c}$$

$$E_x^r(i,N) = -E_x^b(i,N) \quad \text{for} \quad 0 \le i \le M. \tag{2.76d}$$

Due to grid staggering, the central difference requires sampling the fields which are located a half grid outside from the walls. To resolve this problem, a set of virtual ghost points are defined at points with indices of $(-1/2, j)$ and $(M+1/2, j)$ for horizontal fields and $(i, -1/2)$ and $(i, N+1/2)$ for vertical fields. Each ghost point can be updated independently of all the other ghost points. On each ghost line, the field values are

$$E_x^r(M+\frac{1}{2},j) = E_x^r(M-\frac{1}{2},j) - \frac{\Delta x}{\Delta y}\left(E_y^r(M,j+\frac{1}{2}) - E_y^r(M,j-\frac{1}{2})\right), \tag{2.77a}$$

$$E_x^r(-\frac{1}{2},j) = E_x^r(\frac{1}{2},j) + \frac{\Delta x}{\Delta y}\left(E_y^r(M,j+\frac{1}{2}) - E_y^r(M,j-\frac{1}{2})\right), \tag{2.77b}$$

$$E_y^r(i,-\frac{1}{2}) = E_y^r(i,\frac{1}{2}) + \frac{\Delta y}{\Delta x}\left(E_x^r(i+\frac{1}{2},0) - E_x^r(i-\frac{1}{2},0)\right), \tag{2.77c}$$

$$E_y^r(i,N+\frac{1}{2}) = E_y^r(i,N-\frac{1}{2}) - \frac{\Delta y}{\Delta x}\left(E_x^r(i+\frac{1}{2},N) - E_x^r(i-\frac{1}{2},N)\right). \tag{2.77d}$$

Once the transverse fields were updated, the longitudinal field can be calculated by

$$E_s^n(i,j) = \frac{i}{k}\left(\frac{E_x^{r,n}(i+\frac{1}{2},j) - E_x^{r,n}(i-\frac{1}{2},j)}{\Delta x} + \frac{E_y^{r,n}(i,j+\frac{1}{2}) - E_y^{r,n}(i,j-\frac{1}{2})}{\Delta y}\right). \tag{2.78}$$

If it is only interesting to calculate the longitudinal impedance, it is no need to calculate E_s at every grid point. Thus only field values at the center of the beam (x_c, y_c) are to be evaluated.

The conditions for grid size and stability criterion will be mentioned in the next section but no details will be provided. The reader is referred to Refs. [26, 78] for this issue.

2.5 Numerical results

The algorithms discussed in Sections 2.3 and 2.4 are implemented in the programming language FORTRAN 90 on a workstation. A code named CSRZ was developed. In this section, a few examples are to be presented to illustrate the applications using this code. Throughout this section, the beam is always located at the center of the chamber in the $x-y$ plane, i.e. $(x_c, y_c) = (a/2, b/2)$.

Besides calculating the CSR impedance, the code provides the convenience of storing data of the field profiles. As a first example, in Fig. 2.4 the steady-state horizontal radiation field of the ultra-relativistic beam established in the straight chamber is plotted. By taking a look back at the boundary conditions of Eqs. (2.49-2.52), it is confirmed that the derivative of the radiation field has finite values on the relevant boundary.

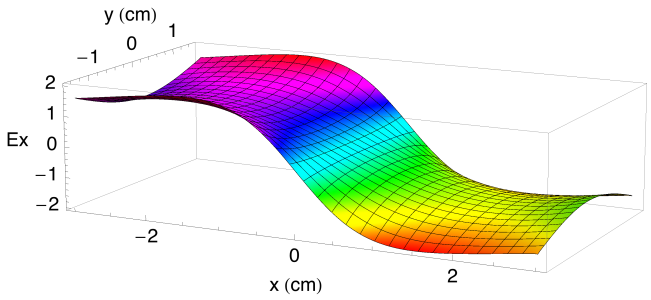

Figure 2.4: Horizontal radiation field established by a beam in a straight chamber. The unit of the electric field is kV·s/m.

2.5.1 Single dipole

The first test is to calculate the CSR impedance generated by a single short bending magnet with constant bending radius in the curved chamber. In this test, the same parameters as Fig. 9 in Ref. [44] are used for the magnet: the

bending radius $R = 1$ m, and the length of the curved chamber $L_b = 0.2$ m. The horizontal and vertical dimensions of the chamber cross-section are $a = 6$ cm and $b = 2$ cm, respectively. The calculation results are compared with those given by Stupakov's code [44] as shown in Figs. 2.5(a) and 2.5(b). The comparison shows good agreement in general. The tiny discrepancy in the high frequency impedance is due to the mesh sizes chosen in calculation. Decreasing the mesh sizes, resulting in longer computer time, can give better results which are converged to those given by the mode expansion method [44]. Thus, the benchmark between two independent methods confirms the capability of CSRZ code.

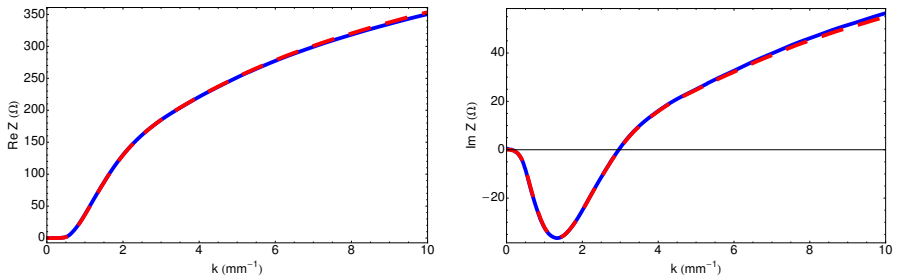

(a) Real part (b) Imaginary part

Figure 2.5: CSR impedance for a single bending magnet with $R = 1$ m and $L_b = 0.2$ m. The dimensions of the chamber cross-section are $a = 6$ cm, and $b = 2$ cm. The blue and dashed red lines are given by Stupakov's code and our code, respectively.

The previous example shows smooth CSR impedance for a short magnet. The next example is to investigate the influence of the length of the curved chamber on the CSR impedance. At this time, parameters are set as $R = 5$ m, $a = 6$ cm, and $b = 3$ cm and the toroidal chamber length is varied as $L_b = 0.5, 2, 8$ m. The impedance results are shown in Figs. 2.6(a) and 2.6(b). In the same figures, the results given by the parallel plates model [26] are also plotted in solid black lines. And the corresponding wake potentials with a short bunch of rms length $\sigma_z = 0.5$ mm are given in Fig. 2.6(c). When $L_b = 0.5$ m, which indicates a short curved chamber, the impedance is very smooth. When the curved chamber gets longer, the impedance becomes fluctuating with an interval of around 1.3 mm^{-1} in wavenumber and eventually results in a series of resonant peaks. This observation

clearly indicates that the CSR impedance is actually related to the eigenmodes of the curved chamber [71]. When the curved chamber is long enough, some specific modes which fulfill the phase matching condition can be strongly excited by the beam and become dominant in the radiation fields.

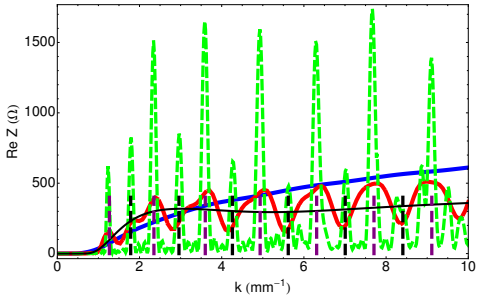

(a) Real part (The purple and black dashed lines denote E_x and E_y modes with $p = 1$, respectively.)

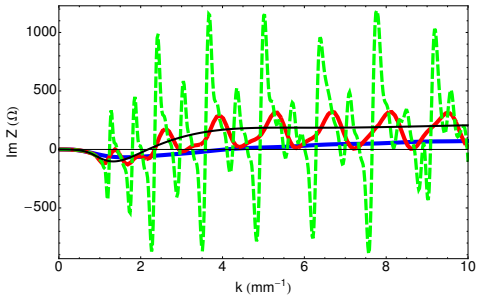

(b) Imaginary part

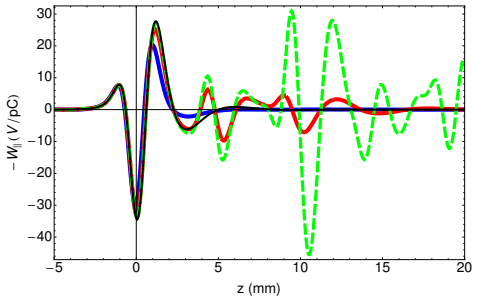

(c) Wake potential

Figure 2.6: CSR impedance and wake potential for a single bending magnet with $R = 5$ m and varied length of the curved chamber $L_b = 0.5,\ 2,\ 8$ m. The dimensions of the chamber cross-section are $a = 6$ cm, and $b = 3$ cm. The gaussian bunch length $\sigma_z = 0.5$ mm with bunch head to the left side. The impedances and wake potential have been normalized by the length of the curved chamber. Blue solid lines: $L_b = 0.5$ m; red solid lines: $L_b = 2$ m; green dashed lines: $L_b = 8$ m; black solid lines: parallel plates model.

One can compare the wavenumbers at the resonant peaks in Fig. 2.6(a) with the analytical predictions which are available in Refs. [57, 58, 71]. According to

Ref. [58], the resonance peaks should appear at wavenumbers of

$$k_{mp} = \frac{p\pi}{b}\sqrt{\frac{R}{x_o}}\Upsilon\left(\frac{b(m \pm 0.25)}{px_o}\right), \tag{2.79}$$

where the integer indices m and p denote the individual mode of the curved chamber and x_o is the distance from the beam orbit to the outer wall in the horizontal plane. The plus sign in Eq. (2.79) indicates E_x modes in which $E_y = 0$ and $m = 0, 1, 2, 3, ...$; the minus sign indicates E_y modes in which $E_x = 0$ and $m = 1, 2, 3, ...$ According to Ref. [58], p must be odd and $p = 1, 3, 5, ...$ Finally, $\Upsilon(r)$ is defined by

$$\Upsilon(r) = \left[\left(\sqrt{1 + r^2/3} + 1\right)^{1/3} - \left(\sqrt{1 + r^2/3} - 1\right)^{1/3}\right]^{-3/2}. \tag{2.80}$$

When r is large, $\Upsilon(r)$ can be approximated by $3r/2^{3/2}$ [58]. It implies that the resonance peaks in the CSR impedance are almost equally spaced along the wavenumber axis. The resonances are indicated by vertical dashed lines in Fig. 2.6(a). It turns out that they agree well with the observed peaks from numerical calculations.

The wavenumber k_{01} with $m = 0$ and $p = 1$ indicates the lowest mode in the toroidal chamber. At frequencies well below k_{01}, i.e. $k \ll k_{01}$, CSR fields are highly suppressed. In this frequency region, analytical calculations showed that the real part impedance is very small and the imaginary part impedance is well represented as a quadratic function of frequency [55]. These properties are generally observed in the numerical calculations.

As stated in Refs. [44, 58], when the aspect ratio of the curved chamber a/b is larger than 2, the shielding of the side walls can be neglected and the parallel plates model is a good approximation for a long bending magnet. This criterion works well in the low frequency region with $k < k_{th}$ which was proved in Ref. [58]. Here k_{th} is the shield threshold defined by [58]

$$k_{th} = \pi\sqrt{\frac{R}{b^3}}. \tag{2.81}$$

The numerical calculations do agree with this criterion. On the contrary, in the high frequency region, the CSR impedance may significantly differ from the

parallel plates model and exhibit fluctuations and even narrow resonance peaks for a long curved chamber. A geometrical explanation [40, 64, 73, 84] for this observation can be illustrated as in Fig. 2.7. The CSR field is radiated in the direction tangent to the beam trajectory when a beam enters the curved chamber. The outer wall plays a role of mirror and reflects the field back to the beam. If the curved chamber is long enough, the reflected field can accumulate and become significant. The geometrical picture of CSR suggests a critical length of

$$L_o = 2R\theta_o \approx 2\sqrt{2Rx_o}, \tag{2.82}$$

for the curved chamber. Here $\theta_o = \text{ArcCos}\,(R/(R+x_o)) \approx \sqrt{2x_o/R}$, and the approximation is justified when the chamber dimension is much smaller than the bending radius, i.e. $x_o \ll R$. If $L_b \gg L_o$, some specific modes can be strongly excited, resulting in the fluctuations or resonant peaks in the CSR impedance. If $L_b \leq L_o$, such fluctuations will be negligible. But if $L_b \ll L_o$, transient effect will also become important. The critical length indicates a length when the reflection of the outer wall becomes important. But L_o does not depends on the aspect ratio of the pipe cross-section. Therefore, the condition of neglecting side-wall shielding, i.e. $L_b \leq L_o$, can be a supplement to the criteria of $a/b \geq 2$ which only applies at low frequency limit, i.e. $k < k_{th}$.

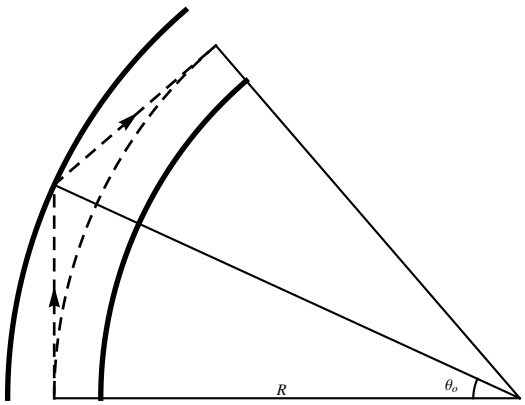

Figure 2.7: CSR reflected by the outer wall of the beam pipe. The beam starts to radiate fields at the entrance of the curved chamber. The dashed curve without arrows on it denotes the beam orbit. The arrowed dashed lines represent the direction of the radiation fields.

Similar to the optical approximation in the theory of geometric impedance [85], the critical length L_o defined by Eq. (2.82) can also be interpreted as a catch-up distance over which the CSR, generated by the head of a beam, reflects from the outer wall and reaches the beam tail at length Δs_o behind the head. It is easy to calculate Δs_o from the geometry shown in Fig. 2.7, and the result is [73]

$$\Delta s_o = 2R(\mathrm{Tan}(\theta_o) - \theta_o) \approx \frac{4}{3}\sqrt{\frac{2x_o^3}{R}}. \tag{2.83}$$

The quantity Δs_o corresponds to a modulation wavenumber of [73]

$$\Delta k = \frac{2\pi}{\Delta s} \approx \frac{3\pi}{2}\sqrt{\frac{R}{2x_b^3}}. \tag{2.84}$$

It turns out that $\Delta k = k_{(m+1)p} - k_{mp}$ is exactly the distance between adjacent resonances for the same vertical index p and large argument r in Eq. (2.80). When comparing Δs_o with the bunch length σ_z, one can find another condition of neglecting outer-wall shielding effect in evaluating CSR induced instability, i.e. $\Delta s_o \gg \sigma_z$. Namely, this condition says that the reflected CSR fields from the outer wall can never catch up with the beam tail and thus has no influence on the beam in total.

One can check Eqs. (2.83) and (2.84) by applying them to the examples depicted in Fig. 2.6(a). The value $\Delta k = 1.4$ mm^{-1} is close to the observed value of 1.3 mm^{-1}. $\Delta s_o = 4.4$ mm^{-1} is roughly the distance at which the first peak appears in the tail part of the wake potential in Fig. 2.6(c). Since the bunch length $\sigma_z = 0.5$ mm is much smaller than Δs_o, the amplitude of the wake potential in the vicinity of the beam is almost independent of magnet length. Thus, it can be concluded that the outer-wall shielding mainly impose effects in the tail part of CSR wake.

As depicted in Fig. 2.7, the radiation fields take a longer path than the beam. Thus, the previous discussions on outer-wall shielding holds for the trailing fields. A similar geometric interpretation holds for the shielding of overtaking fields due to the inner chamber wall. Detailed discussions are given in Ref. [64]. The relevant critical length of the curved chamber is

$$L_i = 2R\theta_i \approx 2\sqrt{2Rx_i}, \tag{2.85}$$

with $\theta_i = \mathrm{ArcCos}\left((R - x_i)/R\right) \approx \sqrt{2x_i/R}$. The quantity x_i is the distance from the beam to the inner wall in the horizontal plane, and the approximations are justified if $x_i \ll R$. When the beam travels the distance of L_i, the radiation fields will overtake the head of the beam at

$$\Delta s_i = 2R(\theta_i - \mathrm{Sin}(\theta_i)) \approx \frac{2}{3}\sqrt{\frac{2x_i^3}{R}}. \tag{2.86}$$

If $\Delta s_i \gg \sigma_z$, one can expect that the overtaking fields will reach the bunch head without seeing the inner chamber wall. Thus, the shielding due to the inner wall will be negligible. On the other hand, if $\Delta s_i < \sigma_z$, the inner-wall shielding should be taken into account.

In summary, the shielding effects of the outer and inner walls can be treated separately: the trailing fields reflect at the outer wall, resulting in a head-to-tail interaction; the overtaking fields may be shielded by the inner wall, affecting the well-known tail-to-head interaction. In a storage ring, it is usually true that the beam centroid coincides with the center of the vacuum chamber. In this case, there exist $x_o = x_i = a/2$, $L_o = L_i$, and $\Delta s_i = \Delta s_o/2$. It turns out that the condition of neglecting chamber-wall shielding can be approximated as $\sigma_z \ll \sqrt{a^3/R}$. This is exactly the condition found in Ref. [64].

It is also interesting to plot the profiles of the radiation field on the resonances, and then to compare them with the field patterns of individual modes. The field patterns of E_x modes are described by [71]

$$E_x(x, y) = \mathrm{Ai}\left(k_y^2\kappa_{mp}^2 - x/\kappa_{mp}\right)\sin\left(k_y(y + y_c)\right), \tag{2.87}$$

where $\mathrm{Ai}(z)$ is Airy function of the first kind and

$$\kappa_{mp} = \left(\frac{R}{2k_{mp}^2}\right)^{1/3}. \tag{2.88}$$

The field patterns of E_y modes are described by [71]

$$E_y(x, y) = \mathrm{Ai}\left(k_y^2\kappa_{mp}^2 - x/\kappa_{mp}\right)\cos\left(k_y(y + y_c)\right). \tag{2.89}$$

For examples, the modes with indices (m, p) of $(0, 1)$, $(3, 1)$ and $(6, 1)$ correspond to wavenumbers of $k_{mp} = 1230,\ 4930,\ 9100\ \mathrm{m}^{-1}$. The contour plots of

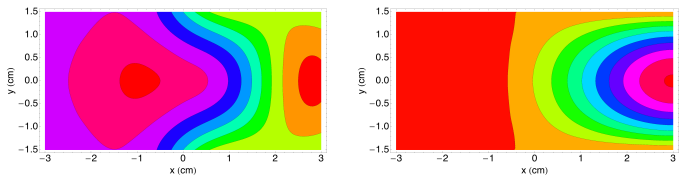

(a) Real part (b) Imaginary part

Figure 2.8: Contour plots for the profiles of the radiation field E_x^r at the exit of the curved chamber with $k = 1230$ m^{-1} and $L_b = 8$ m. The outer wall of the chamber is to the right side.

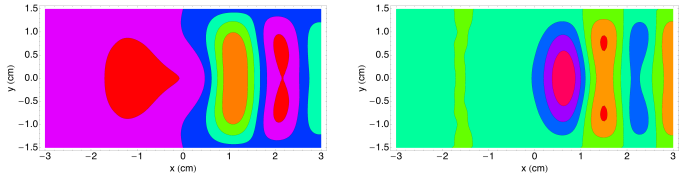

(a) Real part (b) Imaginary part

Figure 2.9: Contour plots for the profiles of the radiation field E_x^r at the exit of the curved chamber with $k = 4930$ m^{-1} and $L_b = 8$ m. The outer wall of the chamber is to the right side.

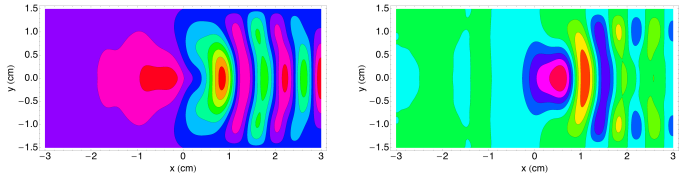

(a) Real part (b) Imaginary part

Figure 2.10: Contour plots for the profiles of the radiation field E_x^r at the exit of the curved chamber with $k = 9100$ m^{-1} and $L_b = 8$ m. The outer wall of the chamber is to the right side.

the real parts of E_x^r at the exit of the curved chamber with $L_b = 8$ m are shown in Figs. 2.8(a), 2.9(a) and 2.10(a). The imaginary parts are shown in Figs. 2.8(b), 2.9(b) and 2.10(b).By comparing the field profiles with field patterns of a single mode (see Figs. 2.11(a), 2.11(b), and 2.11(c)), it is clearly seen that only one mode is dominant near the resonance peaks. The radiation fields are mostly con-

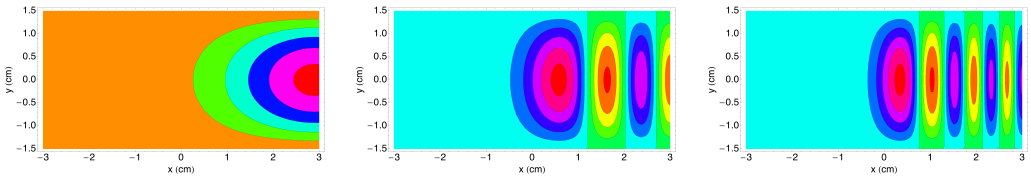

(a) $(m, p) = (0, 1)$ (b) $(m, p) = (3, 1)$ (c) $(m, p) = (6, 1)$

Figure 2.11: Contour plots of the field patterns of E_x modes of a rectangular toroidal pipe with indices (m, p).

centrated on the right side of the beam, close to the outer wall. It is also worthy to note that there is another kind of fields on the left side of the beam (see real parts of E_x^r in Figs. 2.8(a), 2.9(a) and 2.10(a)). This field does not have the normal features of an eigenmode in a curved chamber. A hypothesis is that it is related to the fields due to the imaginary frequency poles as discussed in Ref. [58]. This field has the features of near-field which clings to the source beam [58]. It is also observed that when the wavenumber k goes higher, the near-field shrinks to smaller area and becomes closer to the beam.

2.5.2 Interference in a series of bending magnets

In a realistic storage ring, the bending magnets are arranged consecutively along the beam orbit. There is a concern that interference may enhance the CSR generated in a series of bending magnets. The CSRZ code can treat this case straightforwardly. As an example, 4 identical hard-edge magnets are placed along s. The drift chambers between the 4 magnets are also identical. In this case, $R^{-1}(s)$ can be described by a step function. The parameters for the magnets and chamber are $R = 5$ m, $L_b = 2$ m, $a = 6$ cm and $b = 3$ cm. The length of the drift chambers is $L_d = 2$ m. The impedance is plotted in Figs. 2.12(a) and 2.12(b) and

compared with that of single magnets. The corresponding wake potentials with a short bunch of rms length $\sigma_z = 0.5$ mm are given in Fig. 2.12(c). Again it is seen that many narrow spikes which indicate that specific eigenmodes can satisfy the phase matching conditions and will be excited by the beam. The impedance of a single magnet looks to be broad-band approximation of that of a series of magnets. The narrow spikes in the impedance lead to long-range wake fields as seen in the wake potential.

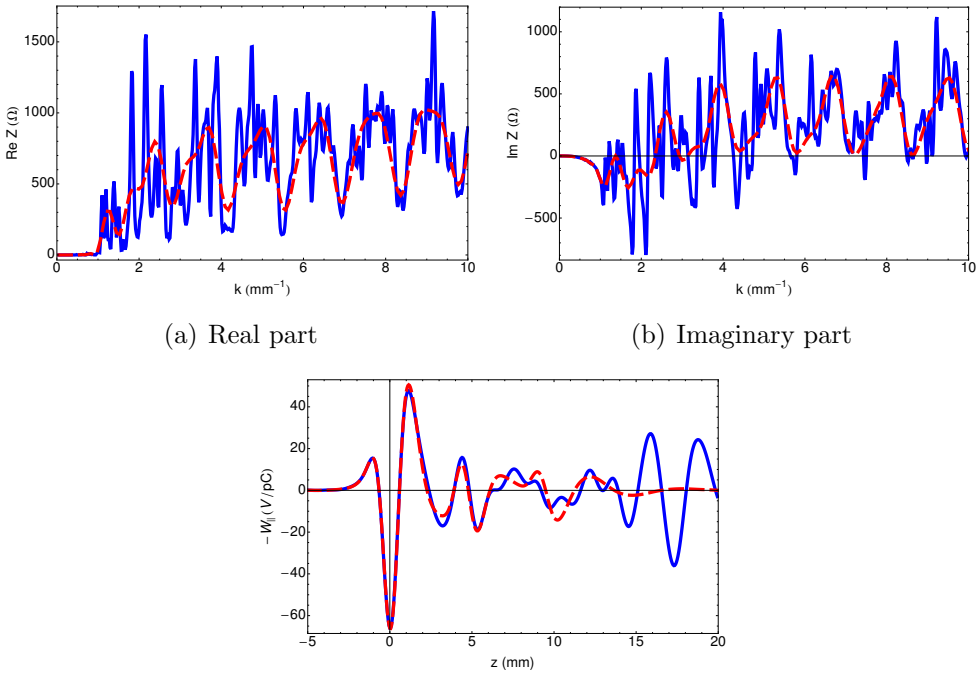

(a) Real part

(b) Imaginary part

(c) Wake potential

Figure 2.12: CSR impedance and wake potential for 4 bending magnets interleaved with equidistant drift chambers. The magnet parameters: $R = 5$ m, L_b=2 m. The length of drift chamber: $L_d = 2$ m. The dimensions of the chamber cross-section: $a = 6$ cm, $b = 3$ cm. The gaussian bunch length $\sigma_z = 0.5$ mm with bunch head to the left side. The wake potentials have been normalized by the number of magnets. The blue and dashed red lines are the impedances with and without considering interference, respectively.

Naturally one can suspect that if there are many bending magnets placed in a long curved chamber, more high peaks should be observed in the CSR impedance.

This is proved by a more practical case of the SuperKEKB positron damping ring [86]. As shown in Fig. 2.13, the layout of this damping ring contains two arc sections. In each section, there are in total 16 cells. Each cell contains two reverse bending magnets [87], of which the bending radius as a function of s is shown in Fig. 2.14. The drift between consecutive cells is around 1 m. The vacuum chamber cross-section is approximated by a square with $a = b = 3.4$ cm. The CSR impedances of one arc section (in total 16 cells), of 6 consecutive cells, and of 1 cell are calculated. The results are compared with that of single-bend model as shown in Figs. 2.15(a) and 2.15(b). It is not surprising that many narrow and high peaks appear in the impedance spectrum when the number of cells grows. And the CSR impedance calculated using single magnet model again provides a broad-band approximation. The wake potentials with rms bunch length of

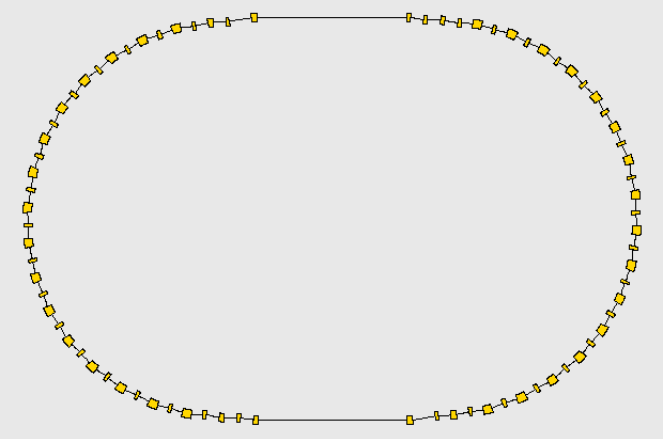

Figure 2.13: Layout of SuperKEKB positron damping ring. Only dipole magnets are marked in the plot.

0.5 mm corresponding to the previous impedances are plotted in Fig. 2.15(c). The figure clearly shows that the tail parts are strongly modulated due to interference effect. It is also observed that the shape of wake potential due to 6 cells is already close to that of 16 cells at the distance less than 20 mm to the beam center. This is because that the CSR fields generated at the first cells keep far behind the beam and almost die out in the range considered after the beam traverses several arc cells.

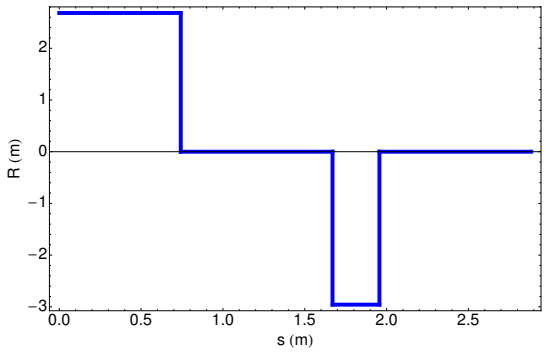

Figure 2.14: Bending radius as a function of s for one arc cell of SuperKEKB positron damping ring.

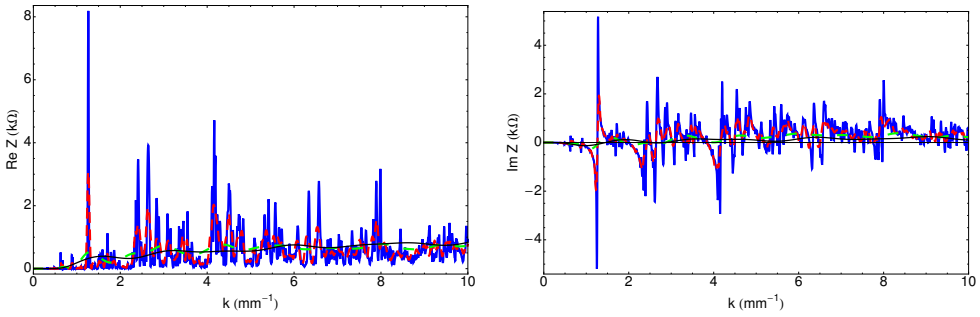

(a) Real part (b) Imaginary part

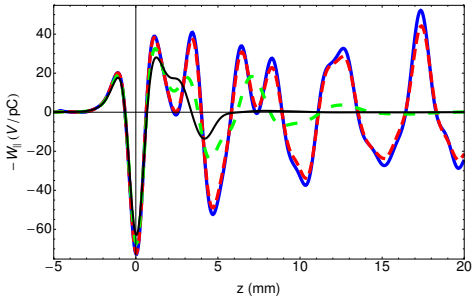

(c) Wake potential

Figure 2.15: CSR impedance and wake potential of the arc section in the SuperKEKB positron damping ring. The impedances and wake potentials have been normalized by the number of cells. The gaussian bunch length $\sigma_z = 0.5$ mm with bunch head to the left side. Blue solid line: 16 cells; red dashed line: 6 cells; Green dashed line: 1 cell; Black solid line: single-bend model.

2.5.3 Application to the compact-ERL at KEK

The cERL is a test facility under construction at KEK for demonstrating key technologies of GeV-class ERLs. The beam energy with one acceleration is 35 MeV in the first commissioning and will be 125 MeV finally [88]. The rms bunch length is 1-3 ps for normal operation and 0.1 ps or less for bunch compression mode. The bunch charge is 7.7 to 77 pC for normal operation and 77pC or more for bunch compression. The vacuum chamber of the cERL loop basically has a round shape with diameter of 50 mm.

The CSR impedance for a single bend is calculated at different beam energy based on Eq. (2.25), as depicted in Fig. 2.16. The vacuum chamber cross-section

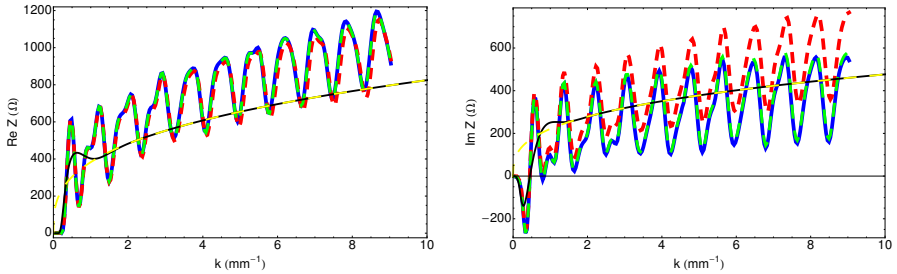

(a) Real part (b) Imaginary part

Figure 2.16: CSR impedance for a single bend in the cERL return loop. The CSR in the drift chamber after the exit of the bend is taken into account. Blue solid lines: γ=∞; red dashed lines: γ=68.5 (E = 35 MeV); green dashed lines: γ=244.6 (E = 125 MeV); black solid lines: steady-state parallel plates model; yellow dashed lines: steady-state free space model.

is approximated by a square with full size of 50 mm. The bending radius and bending angle for one bend are 1 m and $\pi/4$, respectively. The beam is assumed to be located at the center of the chamber, with transverse beam sizes of σ_x = 0.2 mm and σ_y = 0.1 mm. The numerical results are compared with steady-state models in free space [31] and with parallel-plates shielding [26]. From the figures, both numerical and analytical results show that at frequencies lower than $k_{th} = \pi\sqrt{R/b^3}$ [58], the CSR waves are strongly shielded, mainly due to the existence of the upper and lower chamber walls. The outer-wall of the chamber reflects the trailing radiation fields back to the beam and causes fluctuations

in the impedance. The inner-wall of the chamber shields the overtaking fields and changes the slope of the imaginary part of the impedance. The imaginary impedances show remarkable difference in the slope at beam energies of E = 35 MeV and E = 125 MeV. This difference is due to the normal space-charge effect related to the $1/\gamma^2$ term. It suggests that normal space-charge effects can be comparable to CSR effects at the beam energy of 35 MeV. At beam energy of 125 MeV or higher, normal space-charge effects are fairly negligible.

The longitudinal wake potential, indicating energy kick along a beam bunch, can be calculated from impedance with specified bunch profile. As shown in

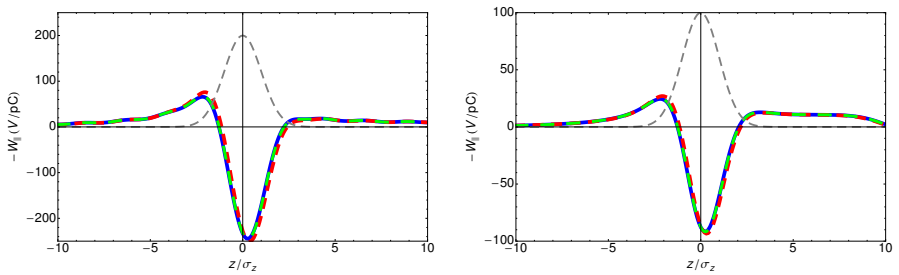

(a) $\sigma_t = 1$ ps

(b) $\sigma_t = 2$ ps

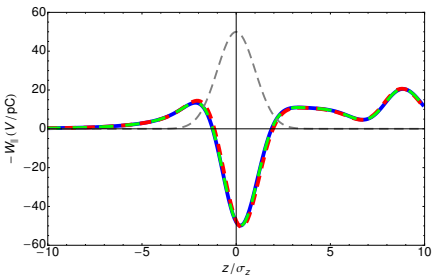

(c) $\sigma_t = 3$ ps

Figure 2.17: CSR wake potentials for a single bend in the cERL return loop with Gaussian bunch lengths of $\sigma_t = 1, 2, 3$ ps. The drift CSR is taken into account. Blue solid lines: $\gamma=\infty$; red dashed lines: γ=68.5 (E=35 MeV); green dashed lines: γ=244.6 (E=125 MeV); gray dashed lines: Gaussian bunch profile.

Fig. 2.17, with Gaussian bunch lengths of $\sigma_t = 1, 2, 3$ ps the CSR wake potentials are calculated from the impedances shown in Fig. 2.16. Because only the normal space-charge fields are considered in a chamber length of $L_b = 0.7854$ m, the space-charge effect is almost invisible from the wake potentials. If taking into

account the space-charge fields distributed around the whole loop, space-charge effect can become remarkable at short bunch length of $\sigma_t = 1$ ps in the low beam energy of 35 MeV.

In Fig. 2.18, the numerical results are compared with the 1D model of Eq. (2.6),

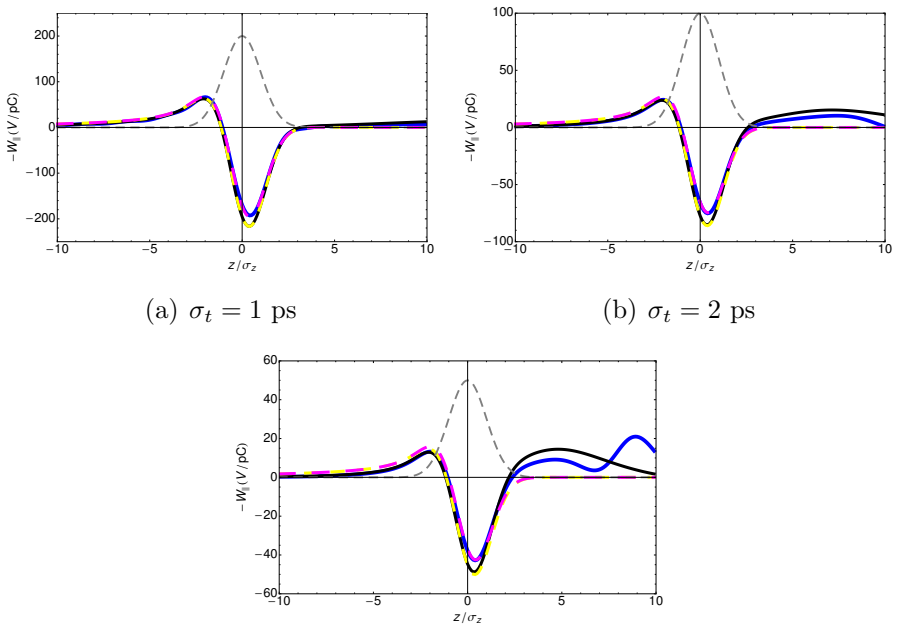

(a) $\sigma_t = 1$ ps

(b) $\sigma_t = 2$ ps

(c) $\sigma_t = 3$ ps

Figure 2.18: CSR wake potentials for a single bend in the cERL return loop with Gaussian bunch lengths of $\sigma_t = 1, 2, 3$ ps and $\gamma = \infty$. The drift CSR is not taken into account. Blue solid lines: by CSRZ; magenta dashed lines: 1D model; black solid lines: steady-state parallel plates model; yellow dashed lines: steady-state free space model; gray dashed lines: Gaussian bunch profile.

which is adopted in ELEGANT code [33]. At this point, the drift CSR, which will be checked in next paragraphs, is ignored tentatively. One observes that in general CSRZ agrees with the 1D model from Saldin *et al.* in predictions of wake fields in the vicinity of bunch center. Meanwhile, the discrepancy of amplitudes in the same area between CSRZ and steady-state models is attributed to entrance transient. Chamber shielding slightly suppresses the CSR wake fields at the bunch head part but enhances the wake fields at the bunch tail part. That is, the particles at the bunch tail part gain energy due to chamber shielding.

Only when the bunch length is short enough, i.e. much less than $1/k_{th}$, chamber shielding is negligible.

The effect of CSR in the drift chamber after the exit of the bend is illustrated in Figs. 2.19-2.21. As observed from Fig. 2.19, with drift CSR neglected, the average

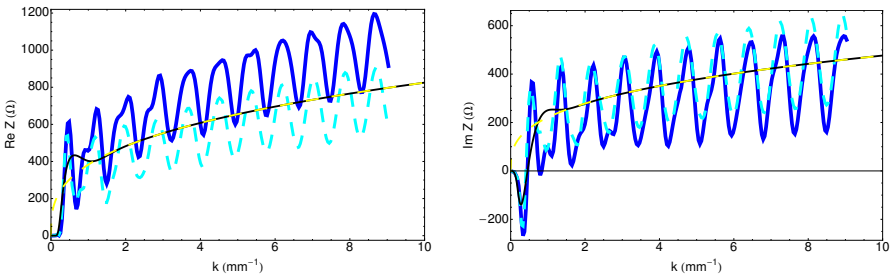

(a) Real part (b) Imaginary part

Figure 2.19: CSR impedance for a single bend in the cERL return loop with $\gamma = \infty$. Blue solid lines: with drift CSR considered; cyan dashed lines: with drift CSR neglected; black solid lines: steady-state parallel plates model; yellow dashed lines: steady-state free space model.

slope of the imaginary part of CSR impedance is close to the free-space model at high frequency. But the average slope of the real part is slightly lower than the free-space model. This is due to the transient effect at the entrance part. The drift CSR changes the slope of both real and imaginary parts of CSR impedance under the existence of straight chamber. This feature reveals the complexity of evaluating its effects on beam dynamics. The wake potentials corresponding to the impedances of Fig. 2.19 are shown in Fig. 2.20. One can easily see that the drift CSR causes additional energy loss and gain for particles in the vicinity of bunch centroid and in the bunch tail part, respectively.

Finally, the numerical results are compared with the free-space model for drift CSR given by Eq. (2.9) [61]. The results are shown in Fig. 2.21. It is seen that for bunch lengths longer than 1 ps, the free-space model overestimates the energy kick at the bunch centroid, and particles at the tail part gain energy due to chamber shielding.

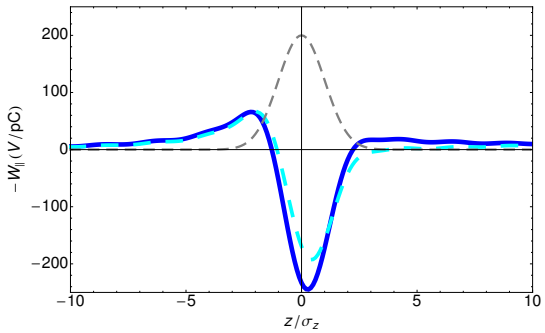

(a) $\sigma_t = 1$ ps

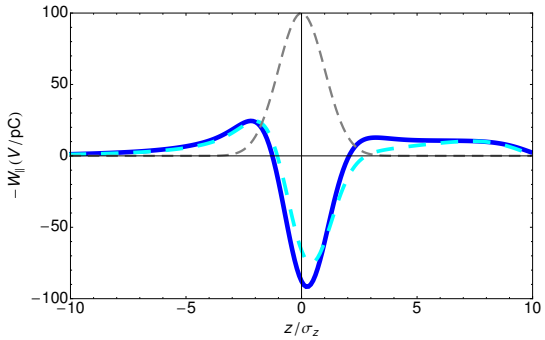

(b) $\sigma_t = 2$ ps

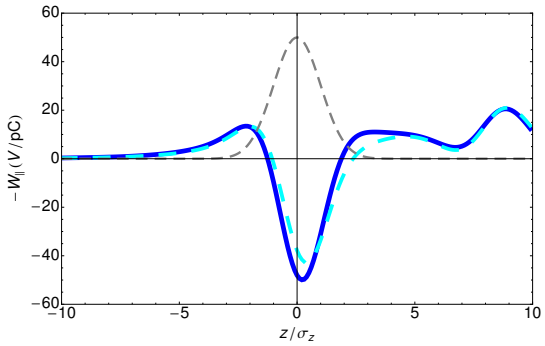

(c) $\sigma_t = 3$ ps

Figure 2.20: CSR wake potentials for a single bend in the cERL return loop with Gaussian bunch lengths of $\sigma_t = 1, 2, 3$ ps and $\gamma = \infty$. Blue solidlines: with drift CSR considered; cyan dashed lines: with drift CSR neglected; gray dashed lines: Gaussian bunch profile.

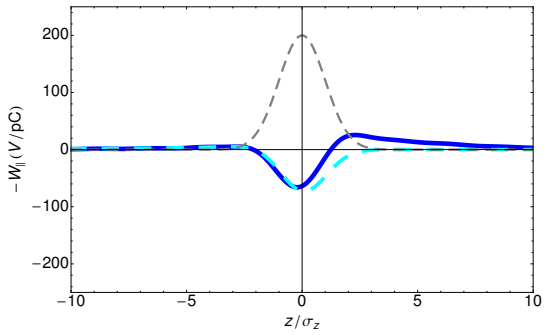

(a) $\sigma_t = 1$ ps

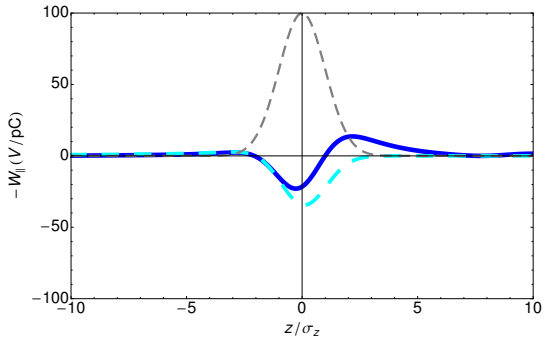

(b) $\sigma_t = 2$ ps

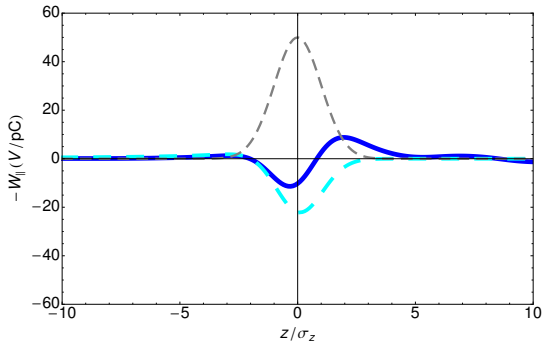

(c) $\sigma_t = 3$ ps

Figure 2.21: CSR wake potentials for a single bend in the cERL return loop with Gaussian bunch lengths of $\sigma_t = 1, 2, 3$ ps and $\gamma = \infty$. Blue solidlines: drift CSR by CSRZ; cyan dashed lines: drift CSR by Stupakov and Emma's free-space model; gray dashed lines: Gaussian bunch profile.

2.5.4 CSR in a wiggler

Now an example of a wiggler is to be studied. For a planar wiggler, the oscillations of the beam are confined to the horizontal plane. The beam traversing through the wiggler undergoes sinusoidal motion, to first-order approximation. Thus the curvature of the beam orbit can be approximated by a cosine function, i.e. Eq. (2.30). Since it has been assumed in the CSRZ code that the chamber cross-section is uniform along the beam orbit, the chamber inside the wiggler is modeled as a "wiggling" one in numerical calculations. The effect of a wiggling chamber was well discussed and compared with analytically obtained results in Ref. [89]. It was found that in the case of large aspect ratio of a/b, a wiggling chamber is correct enough for purpose of demonstration. For exemplification of

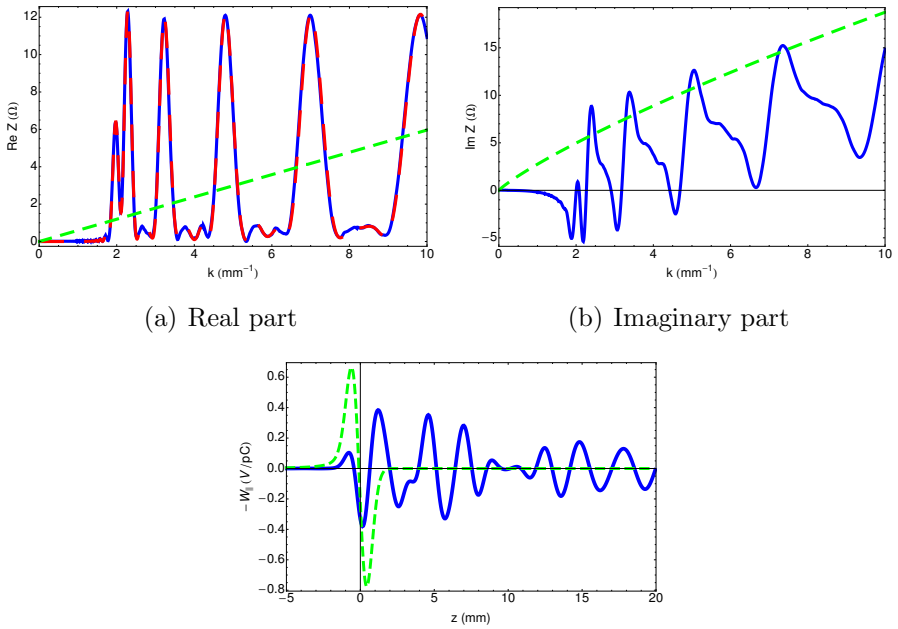

(a) Real part

(b) Imaginary part

(c) Wake potential

Figure 2.22: CSR impedance and wake potential of a wiggler. The blue lines are numerical results. The dashed red line and dashed green lines are given by Eq. (2.90) and Eq. (2.93), respectively. The gaussian bunch length $\sigma_z = 0.5$ mm with bunch head to the left side.

the approach, the parameters of a wiggler are set as: maximum bending radius

$R_0 = 100$ m and magnetic field wavelength $\lambda_w = 2\pi/k_w = 1$ m, and the number of periods $N_u = 10$. The chamber width and height are set to be $a = 10$ cm and $b = 2$ cm. The results are shown in Figs. 2.22(a) and 2.22(b). The wake potentials with rms bunch length of 0.5 mm corresponding to the impedances are plotted in Fig. 2.22(c). It turns out that the CWR with chamber shielding can differ remarkably from the free-space model.

By enlarging the chamber height, the shielding effect of up- and down-side chamber walls can be tested. This is demonstrated in Figs. 2.23. In these calcu-

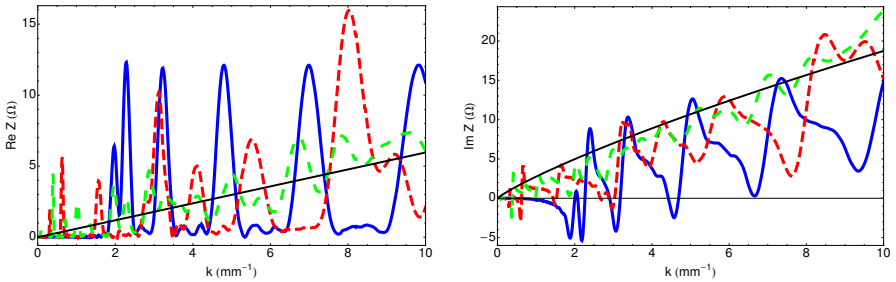

(a) Real part (b) Imaginary part

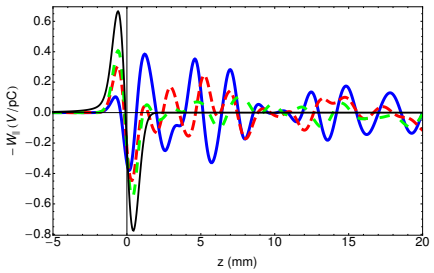

(c) Wake potential

Figure 2.23: CSR impedance and wake potential of a wiggler with $b = 2, 5, 10$ cm. The gaussian bunch length $\sigma_z = 0.5$ mm with bunch head to the left side. Blue solid lines: $b = 2$ cm; red dashed lines: $b = 5$ cm; green dashed lines: $b = 10$ cm; black solid lines: free-space model.

lations, the chamber height is varied as $b = 2, 5, 10$ cm and all other parameters are kept the same as in the previous example. Both the impedance and wake potential tend to be close to that of free-space model while the chamber height is enlarged.

Next the effect of wiggler length is tested. This is demonstrated in Figs. 2.24 and 2.24(c). In these calculations, the chamber height is set to be $b = 10$ cm and the number of periods, which correspond to total length of the wiggler, is varied as $N_u = 1, 4, 8$. All other parameters are kept the same as in the previous examples. It is seen that as the wiggler becomes longer, the impedance spectrum changes from smooth curve to that with many narrow peaks at low frequency part. And the narrow peaks in impedance cause fluctuations in the wake potential at the tail parts.

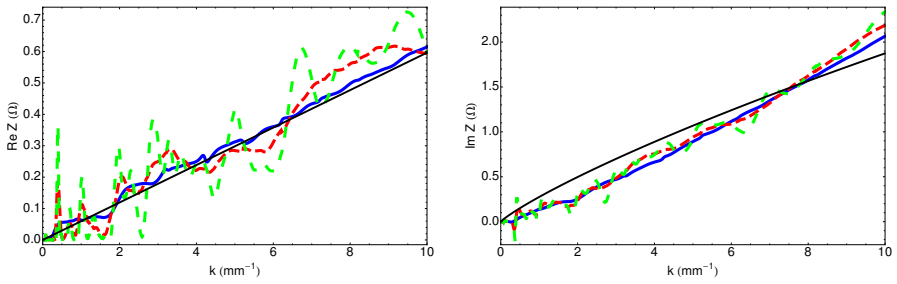

(a) Real part (b) Imaginary part

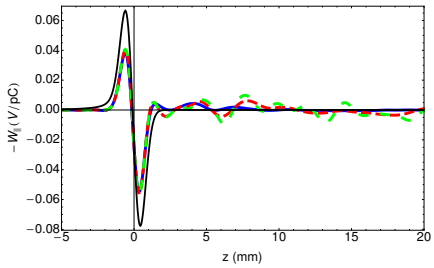

(c) Wake potential

Figure 2.24: CSR impedance and wake potential of a wiggler with the total length varied by setting $N_u = 1, 4, 8$. The impedances and wake potentials have been normalized by the number of period for convenience of comparison. The gaussian bunch length $\sigma_z = 0.5$ mm with bunch head to the left side. Blue solid lines: $N_u = 1$; red dashed lines: $N_u = 4$; green dashed lines: $N_u = 8$; black solid lines: free-space model.

In Ref. [89], the real part impedance in a rectangular chamber was calculated

analytically using mode expansion method

$$\text{Re } Z(k) = \frac{4Z_0}{abR_0^2} \sum_{m=0}^{\infty} \sum_{p=1}^{\infty} \frac{k}{(1+\delta_{m0})k_z} \frac{\sin^2\left((k-k_z-k_w)L_w/2\right)}{(k-k_z)^2 - k_w^2}, \tag{2.90}$$

where $k_z = \sqrt{k^2 - \alpha_{mp}^2}$ with $\alpha_{mp} = \sqrt{k_x^2 + k_y^2}$, $k_x = m\pi/a$ and $k_y = p\pi/b$. The quantity $L_w = N_u(2\pi/k_w)$ is the total length of the wiggler. The summation in Eq. (2.90) goes over the even values of m and the odd values of p. Equation (2.90) also indicates the resonance condition

$$k - k_z - k_w = 0, \tag{2.91}$$

which shows that the resonant peaks in impedance should appear at

$$k_{mp} = \frac{\alpha_{mp}^2 + k_w^2}{2k_w}. \tag{2.92}$$

The resonant peaks in Fig. 2.22(a) do agree with the above equation. The impedance for a wiggler in free space is given in Ref. [90]

$$Z(k) = \frac{1}{4} Z_0 L_w k \frac{k_w}{k_0} \left(1 - \frac{2i}{\pi}\left(\log\frac{4k}{k_0} + \gamma_E\right)\right), \tag{2.93}$$

where $k_0 = 4k_w^3 R_0^2$ is the fundamental radiation wavenumber with the wiggler parameter $K \gg 1$. The quantity $\gamma_E \approx 0.577$ is the Euler constant. One sees that the numerical results again agree well with the analytic formula Eq. (2.90) but disagree with Eq. (2.93). Specially, the imaginary part does not show the property of linear slope in the limit of low frequency which is predicted by the free space model.

In the last demonstration, the CSR impedance of one wiggler section in the SuperKEKB low energy ring was calculated. The wiggler field is approximated by a series of short hard-edge bending magnets with opposite polarity interleaved with drift chambers. The cross-section of the chamber is square with the size of 90 mm. The wiggler section consists of 15 identical super-periods and its total length is 141.4 m. The bending radius as function of s for one super-period is plotted in Fig. 2.25. The calculated impedance is shown in Figs. 2.26(a) and 2.26(b). The wake potentials with rms bunch length of 0.5 mm corresponding to the impedances are plotted in Fig. 2.26(c).

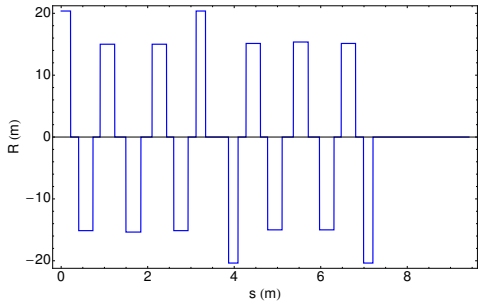

Figure 2.25: Bending radius as function of s for one super-period in the wiggler section of SuperKEKB low energy ring.

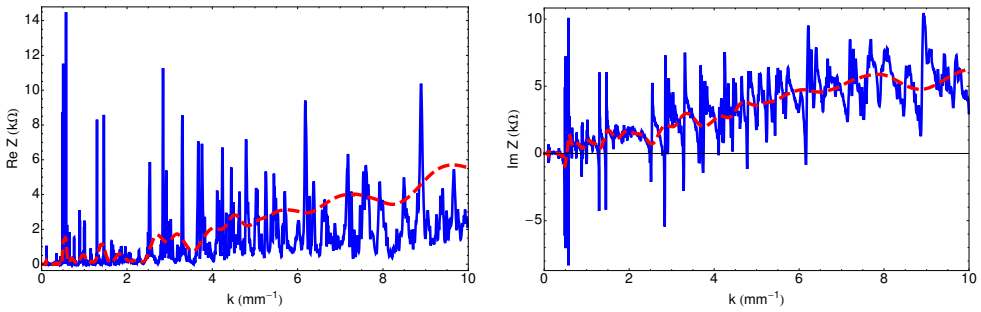

(a) Real part (b) Imaginary part

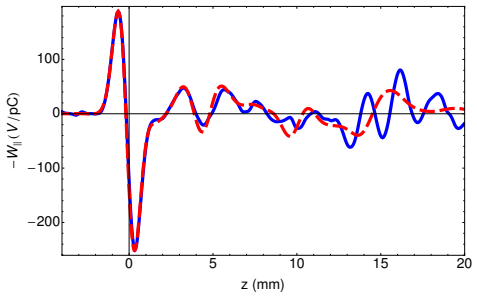

(c) Wake potential

Figure 2.26: CSR impedance and wake potential of the wiggler section in the SuperKEKB low energy ring. The gaussian bunch length $\sigma_z = 0.5$ mm with bunch head to the left side. Blue solid lines: 15 super-periods; red dashed lines: 1 super-period. For convenience of comparison, the values of red dashed curves have been timed by a factor of 15.

3

Coherent wiggler radiation

3.1 Introduction

In the main rings of KEKB and SuperKEKB, wigglers are used to shorten the damping time. In a damping ring where wigglers are used for main purpose of radiation damping, coherent radiation in the wigglers can also contribute impedance. The impedance from undulator or wiggler was first studied in Refs. [91, 92]. Simple formula was found for an infinite long wiggler in free space [90] and applied to the instability analysis in a storage ring [93].

In the light-source community, usually one is more interested in the radiation power emitted from accelerated particle in a wiggler or an undulator. A wiggler is characterized by $K \gg 1$ and typically an undulator has the feature of $K \ll 1$ [19]. The analysis of radiation is usually based on Liénard-Wiechert potentials [19] derived in free space. In the presence of uniform waveguide, it was treated using mode expansion methods, which is intimately related to Green's function (for examples, see Refs. [94, 95, 96, 97, 98, 99, 100]). The radiation in finite-length undulator was also studied based on Green's function method [91, 101]. Undulator radiation fields and impedance in the presence of round waveguide were calculated using paraxial Green's functions in Refs. [102, 103].

In Chapter 2, the coherent wiggler radiation (CWR) impedance was calculated using numerical code CSRZ. Therein, the chamber was approximated to be wiggling in the horizontal plane. In practice, the general theory based on dyadic Green's functions was applicable to this problem [91, 94]. Using dyadic Green's

functions, a general expression for the electric fields excited by a single electron, including both space-charge and radiation fields, can be obtained. This is exactly the main goal of this chapter.

The rest of this chapter is organized as follows. In Section 3.2, general theorems and formulas are discussed for purpose of preparation. For a test of the eigenfunction method, the space-charge fields and impedance is treated in Section 3.3. The main part of this chapter, Section 3.4, is devoted to an attempt to find the full solution for the CWR fields and impedance.

3.2 General theorems and formulas

3.2.1 Eigenfunction expansion method to solve inhomogeneous differential equation

In this section, a brief and non-rigorous introduction is given to the eigenfunction expansion method (also called Ohm-Rayleigh method in the literature) as applied to inhomogeneous partial differential equation (PDE).

Suppose an inhomogeneous differential equation for the distribution function $y(\vec{r})$ reads

$$\mathcal{L}y(\vec{r}) = -f(\vec{r}), \tag{3.1}$$

where $\mathcal{L}$ is a linear differential operator and $f(\vec{r})$ represents the source distribution. The Green's function is taken to be the solution of

$$\mathcal{L}G(\vec{r}, \vec{r}') = -\delta(\vec{r} - \vec{r}'), \tag{3.2}$$

where $\delta(z)$ is the Dirac delta function. If $\vec{r} = (x, y, z)$, then $\delta(\vec{r}) = \delta(x)\delta(y)\delta(z)$. An important property of Green's function is the symmetry of its two variables; that is, $G(\vec{r}, \vec{r}') = G(\vec{r}', \vec{r})$.

In a bounded region, the Green's function can be uniquely determined by applying boundary conditions or/and initial conditions. The region of the problem can be infinite extent or a bounding surface. In terms of Green's function, the particular solution of Eq. (3.1) takes on the form

$$y(\vec{r}) = \int_V G(\vec{r}, \vec{r}') f(\vec{r}') \, \mathrm{d}V. \tag{3.3}$$

Equation (3.3) indicates that the Green's function enters in an integral solution of Eq. (3.1). Therefore, the problem of solving Eq. (3.1) changes to solving the equation of Green's function.

The Green's function appears in various forms in the literature, depending on the properties of $y(\vec{r})$ and $f(\vec{r})$. There are three cases of interest which are quite popular in physics:

- If both $y(\vec{r})$ and $f(\vec{r})$ are scalar functions, then $G(\vec{r},\vec{r}')$ is a scalar function.
- If $y(\vec{r})$ is a vector function and $f(\vec{r})$ is a scalar function, then $G(\vec{r},\vec{r}')$ is a vector function.
- If both $y(\vec{r})$ and $f(\vec{r})$ are vector functions, then $G(\vec{r},\vec{r}')$ is a dyadic function.

The explicit expressions for Green's functions can be derived by different methods described in the theory of differential equations. Ohm-Rayleigh method is an alternative approach based on expanding the Dirac delta function in terms of the eigenfunctions of the relevant homogeneous equation

$$\mathcal{L}\psi(\vec{r}) = 0. \tag{3.4}$$

Usually, the above equation is solved in combination with equations of boundary conditions.

To apply Ohm-Rayleigh method, it is necessary to introduce two important properties of the Dirac delta function. Firstly, there exists the identification [104]

$$\delta(t-t') = \frac{1}{2\pi}\int_{-\infty}^{\infty} e^{-i\omega(t-t')}\, d\omega. \tag{3.5}$$

Equation (3.5) is a Fourier representation of Dirac delta function. When bilateral Laplace transform is applied, it results in the complex representation

$$\delta(t-t') = \frac{1}{2\pi i}\int_{\gamma-i\infty}^{\gamma+i\infty} e^{s(t-t')}\, ds, \tag{3.6}$$

which is essentially equivalent to the previous Fourier representation if one notes that ω can take any value in the complex plane.

Secondly, the Dirac delta function can be expanded in terms of any basis of real orthogonal function set $\{\psi_n(x), n = 0, 1, 2, ...\}$. The normalized orthogonal functions satisfy

$$\int_a^b \psi_m(x)\psi_n(x)\ dx = \delta_{mn}, \tag{3.7}$$

which is called the orthonormal relations. In the above equation, δ_{mn} is the Kronecker delta, and the interval (a, b) may be infinite at either end or both ends. Using ψ_n, the delta function can be expanded in terms of the orthogonal functions as follows

$$\delta(x - x') = \sum_{n=0}^{\infty} \psi_n(x')\psi_n(x). \tag{3.8}$$

As an example, the delta function expanded in the circular cylindrical coordinate system is in the form of [104]

$$\delta(\vec{r} - \vec{r}') = \frac{1}{4\pi^2\rho}\delta(\rho - \rho') \sum_{m=-\infty}^{\infty} e^{im(\varphi-\varphi')} \int_{-\infty}^{\infty} e^{i\beta(z-z')}\ d\beta, \tag{3.9}$$

where (ρ, φ, z) denote the three coordinates. Further expansion of $\delta(\rho - \rho')$ is possible if the linear operator $\mathcal{L}$ is given.

To demonstrate the Ohm-Rayleigh method, the inhomogeneous Helmholtz equation is solved as an example. The equation reads

$$\nabla^2\psi(\vec{r}) + k^2\psi(\vec{r}) = -\rho(\vec{r}). \tag{3.10}$$

The orthonormal eigenfunctions $\psi_n(\vec{r})$ satisfy the homogeneous Helmholtz equation

$$\nabla^2\psi_n(\vec{r}) + k_n^2\psi_n(\vec{r}) = 0, \tag{3.11}$$

where k_n is the associated eigenvalue. The Green's function $G(\vec{r}, \vec{r}')$ satisfies the point source equation

$$\nabla^2 G(\vec{r}, \vec{r}') + k^2 G(\vec{r}, \vec{r}') = -\delta(\vec{r} - \vec{r}') \tag{3.12}$$

and the boundary conditions imposed on the solutions of the homogeneous equation. The Green's function can be expanded in terms of $\psi_n(\vec{r})$ as follows

$$G(\vec{r}, \vec{r}') = \sum_{n=0}^{\infty} a_n(\vec{r}')\psi_n(\vec{r}). \tag{3.13}$$

By substituting Eqs. (3.8) and (3.13) into Eq. (3.12), the expressions of coefficients a_n can be obtained. Consequently, the solution for Green's function becomes

$$G(\vec{r},\vec{r}') = \sum_{n=0}^{\infty} \frac{\psi_n(\vec{r}')\psi_n(\vec{r})}{k_n^2 - k^2}. \tag{3.14}$$

3.2.2 Eigenmodes of a uniform waveguide

To determine all the eigenmodes of a uniform waveguide with perfectly conducting walls, we are to solve the homogeneous Helmholtz equation of vector potential

$$\nabla^2\vec{\mathcal{A}} - \frac{1}{c^2}\frac{\partial^2\vec{\mathcal{A}}}{\partial t^2} = 0. \tag{3.15}$$

The boundary condition for the above equation is $\vec{n}\times\vec{\mathcal{A}}|_s = 0$, where $\vec{n}$ is the unit vector normal to the boundary surface. This is derived from the boundary conditions for electric field $\vec{n}\times\vec{\mathcal{E}}|_s = 0$ and magnetic induction $\vec{n}\cdot\vec{\mathcal{B}}|_s = 0$. The problem is solved once a complete set of eigenfunctions to the homogeneous Helmholtz equation is known. These eigenfunctions are usually obtained by the method called separation of variables. Equation (3.15) is quite general and can be applied to any arbitrary cross-section of a waveguide.

The straight rectangular waveguide is the easiest geometry to be solved. It is convenient to solve Eq. (3.15) in the Cartesian coordinate system with the z axis defined to be along the axis of the waveguide. In that case the Laplacian can be evaluated to its characteristic equation by considering solutions of the form

$$\vec{\mathcal{A}}(x,y,z,t) = \vec{\phi}(x,y)e^{-i(\omega t \pm k_z z)}, \tag{3.16}$$

where the plus and minus signs denote backward and forward waves, respectively. Substituting Eq. (3.16) into Eq. (3.15), the equation for the components of $\vec{\phi}$ is obtained as follows

$$\nabla_\perp^2\phi_\nu + \alpha^2\phi_\nu = 0 \quad \text{with} \quad \nu = x,\ y,\ \text{or}\ z, \tag{3.17}$$

where $\alpha^2 = k^2 - k_z^2$, and it is assumed that $k \equiv \omega/c$. The subscript $\perp$ indicates the transverse Laplacian. The corresponding boundary condition is $\vec{n}\times\vec{\phi}|_s = 0$.

For a straight rectangular waveguide with transverse dimensions given by $0 < x < a$ and $0 < y < b$, the non-trivial solutions for the complete set of eigenfunctions are [94]

$$\phi_{mnx}\left(\vec{r}_{\perp}\right) = \phi_{mnx}\left(x,y\right) = \frac{2}{\sqrt{\left(1+\delta_{m0}\right)ab}}\cos\left(k_x x\right)\sin\left(k_y y\right), \tag{3.18a}$$

$$\phi_{mny}\left(\vec{r}_{\perp}\right) = \phi_{mny}\left(x,y\right) = \frac{2}{\sqrt{\left(1+\delta_{n0}\right)ab}}\sin\left(k_x x\right)\cos\left(k_y y\right), \tag{3.18b}$$

$$\phi_{mnz}\left(\vec{r}_{\perp}\right) = \phi_{mnz}\left(x,y\right) = \frac{2}{\sqrt{ab}}\sin\left(k_x x\right)\sin\left(k_y y\right), \tag{3.18c}$$

where $\vec{r}_{\perp}$ indicates the transverse coordinates (x,y), $k_x = \frac{m\pi}{a}$ and $k_y = \frac{n\pi}{b}$ are the transverse wavenumbers. Here m and n are the two integers representing a specific eigenmode. The eigenfunctions satisfy the Helmholtz equation

$$\nabla^2\phi_{mn\nu} + \alpha_{mn}^2\phi_{mn\nu} = 0, \tag{3.19}$$

and the orthonormal condition

$$\int\int \phi_{\mathrm{mn}\nu}\phi_{m'n'\nu}dxdy = \delta_{mm'}\delta_{nn'}, \tag{3.20}$$

where $\nu = x,\ y,$ or z and $\delta_{mm'}$ indicates the Kronecker delta

$$\delta_{mm'} = \begin{cases} 1 & \text{for} \quad m = m' \\ 0 & \text{for} \quad m \neq m' \end{cases}. \tag{3.21}$$

Substituting the eigenfuncitons into Eq. (3.19), the real eigenvalues are found to be

$$\alpha_{mn} = \sqrt{k_x^2 + k_y^2}. \tag{3.22}$$

It is worth to note that the eigenvalues for $\nu = x,\ y,$ or z are identical, and thus are degenerate. Consequently, the dispersion relation is found as follows

$$k^2 = k_x^2 + k_y^2 + k_z^2. \tag{3.23}$$

The propagation constant in the z-direction is $k_z = \sqrt{k^2 - \alpha_{mn}^2}$. For the propagating modes in a lossless waveguide, both k and k_z are real values. For a non-propagating (or evanescent) mode, k_z is imaginary. Therefore the cutoff

wavenumber is also defined as $k_c = \sqrt{k_x^2 + k_y^2}$. From Eq. (3.23), waves propagate along the waveguide according to a parabolic dispersion relation, which is illustrated in Fig. 3.1. The diagram is symmetrical about the k-axis, reflecting the quadratic nature of Eq. (3.23). Because the waveguide is passive, waves propagating in the positive or negative z-direction share the same dispersion behavior.

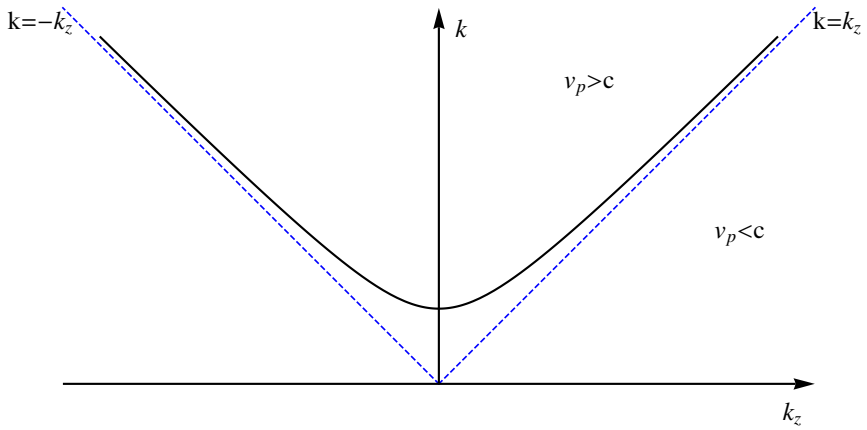

Figure 3.1: Parabolic dispersion relation, typical of waves propagating in a waveguide. The cutoff frequency is reached for $k_z = 0$. The dashed lines split the plane into fast- and slow-wave regions.

There are two distinct regions in the dispersion diagram: the fast-wave region where $v_p > c$ and the slow-wave region where $v_p < c$. The quantity $v_p \equiv \omega/k_z$ is referred to as the phase velocity. From Eq. (3.23), one obtains

$$v_p = \frac{kc}{\sqrt{k^2 - k_c^2}}. \tag{3.24}$$

The phase velocity for propagating modes ($k > k_c$) is actually larger than the speed of light c. Therefore, such waves are always fast waves.

When a wave packet enters the waveguide, its velocity is measured by $v_g \equiv \frac{d\omega}{dk_z}$. The quantity v_g is referred to as the group velocity, which indicates the velocity of the energy propagation along the waveguide. From Eq. (3.23), one finds

$$v_g = \frac{c\sqrt{k^2 - k_c^2}}{k}. \tag{3.25}$$

It is obvious that $v_p v_g = c^2$. A comprehensive discussion of dispersion relation for propagating waves in a waveguide can be found in Ref. [105].

The dispersion relation, i.e. Eq. (3.23), is quite general. In principle, it allows for complex values of k or k_z. For instance, when $k < k_c$, k_z is purely imaginary. The waves with imaginary k_z decay along z-direction and are called evanescent waves in the literature. Another possible case is that k is purely imaginary. Replacing $k \to i\bar{k}$, where $\bar{k}$ is a real value, one finds the dispersion relation changes to

$$-\bar{k}^2 = k_x^2 + k_y^2 + k_z^2, \tag{3.26}$$

where k_z has now to be purely imaginary. By defining $k_z = i\bar{k}_z$, one has $\bar{k}_z = \pm\sqrt{\bar{k}^2 + k_c^2}$. Then a similar dispersion diagram by analogy with the propagating waves can be plotted as shown in Fig. 3.2. It is interesting that one can still define the phase and group velocities for this kind of waves. It turns out that the phase velocity is smaller than c. Thus these waves can be taken as slow waves. In practice, Eq. (3.26) determine the poles on the imaginary wavenumber axis, which will be important in calculating CWR wake fields and impedance in the following sections.

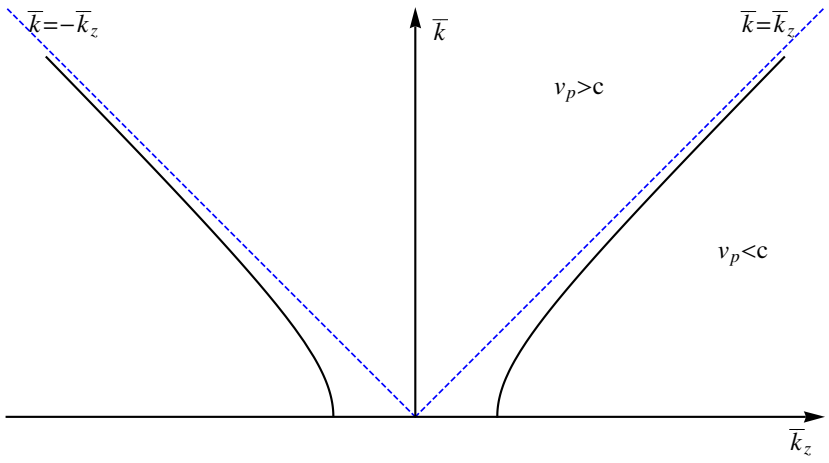

Figure 3.2: Dispersion relation of imaginary-frequency waves in a waveguide.

Before closing this section, let us define the unnormalized eigenfunctions which will be used later, i.e.

$$\phi'_{mnx}(x, y) = \cos(k_x x)\sin(k_y y), \tag{3.27a}$$

$$\phi'_{mny}(x,y) = \sin(k_x x)\cos(k_y y), \tag{3.27b}$$

$$\phi'_{mnz}(x,y) = \sin(k_x x)\sin(k_y y). \tag{3.27c}$$

3.2.3 Dyadic Green's function and vector potential

Now we are to find the solution for the equation of the vector potential, i.e. Eq. (1.13). Because both the source term and the potential are vectors, the relevant Green's function should be dyadic. The equation for the dyadic Green's function of the vector potential is

$$\nabla^2 \overline{\overline{G}}_A(\vec{r},\vec{r}') + k^2 \overline{\overline{G}}_A(\vec{r},\vec{r}') = -\overline{\overline{I}}\,\delta(\vec{r}-\vec{r}'), \tag{3.28}$$

where $\overline{\overline{I}}$ is the unit dyadic and $\delta(\vec{r}-\vec{r}') = \delta(x-x')\delta(y-y')\delta(z-z')$. The physical meaning of $\overline{\overline{G}}_A$ is that it represents the vector potential at $\vec{r}$ corresponding to a unit source at $\vec{r}'$.

For a passive waveguide, the delta function of z in Eq. (3.28) can be replaced by its Fourier transform in the form of Eq. (3.5). The delta function of transverse coordinates can be expanded into the summation of the eigenmodes of the rectangular waveguide as follows

$$\delta(\vec{r}-\vec{r}') = \frac{1}{2\pi}\sum_{m=0}^{\infty}\sum_{n=0}^{\infty}\phi_{mn\nu}(\vec{r}_\perp)\,\phi_{mn\nu}(\vec{r}'_\perp)\int_{-\infty}^{\infty} d\beta\; e^{i\beta(z-z')}, \tag{3.29}$$

where $\nu = x,\ y,$ or z. By applying Ohm-Rayleigh method, the solution of Eq. (3.28) can be obtained as [91, 94, 106]

$$\overline{\overline{G}}_A(\vec{r},\vec{r}') = \frac{1}{2\pi}\sum_{m,n\geq 0}\sum_{\nu=x,y,z}\vec{i}_\nu\vec{i}_\nu\int_{-\infty}^{\infty} d\beta \frac{\phi_{mn\nu}(\vec{r}_\perp)\,\phi_{mn\nu}(\vec{r}'_\perp)}{\beta^2-k_z^2}e^{i\beta(z-z')}, \tag{3.30}$$

where β is taken as the Fourier transform variable, and the subscript $\perp$ denotes the transverse coordinates. The integration over β in Eq. (3.30) can be done using the residue theorem [91, 106]. The result is

$$\overline{\overline{G}}_A(\vec{r},\vec{r}') = \frac{i}{2}\sum_{m,n\geq 0}\sum_{\nu=x,y,z}\vec{i}_\nu\vec{i}_\nu\frac{\phi_{mn\nu}(\vec{r}_\perp)\,\phi_{mn\nu}(\vec{r}'_\perp)}{k_z}e^{ik_z|z-z'|}. \tag{3.31}$$

The above equation is equivalent to

$$\overline{\overline{G}}_A(\vec{r},\vec{r}') = \frac{i}{2}\sum_{m,n\geq 0}\sum_{\nu=x,y,z}\vec{i}_\nu\vec{i}_\nu\frac{\phi_{mn\nu}(\vec{r}_\perp)\,\phi_{mn\nu}(\vec{r}'_\perp)}{k_z} \times\left[\theta(z-z')e^{ik_z(z-z')}+\theta(z'-z)e^{ik_z(z'-z)}\right], \tag{3.32}$$

where $\theta(z)$ is Heaviside step function defined by

$$\theta(z) = \begin{cases} 1 & \text{for} \quad z>0, \\ 0 & \text{for} \quad z<0. \end{cases} \tag{3.33}$$

Note that when evaluating the complex integration over β in Eq. (3.31), the lossy-waveguide condition as suggested in Ref. [94] has been used. For the lossy waveguide, the running waves must be attenuating both with time and along z-direction. This situation requires that $\mathrm{Im}\{\omega(\beta)\} < 0$ and $\mathrm{Im}\{\beta(\omega)\} > 0$, where the symbol $\mathrm{Im}\{\ \}$ denotes the imaginary part of the quantity concerned [94]. In the β-plane, the contour may be taken as in Fig. 3.3.

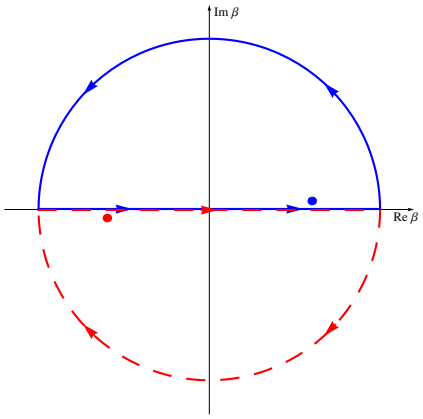

Figure 3.3: Contour for the complex integration over β. The blue solid line is for $z-z'>0$; the red dashed line is for $z-z'<0$. The blue and red dots represent the singular points in the upper and lower plane, respectively.

With in hand the explicit form of $\overline{\overline{G}}_A$, one is able to find the solution in integral form for Eq. (1.13)

$$\vec{A}(\vec{r},\omega) = \mu_0\int\int\int dV'\,\overline{\overline{G}}_A(\vec{r},\vec{r}')\cdot\vec{J}(\vec{r}',\omega)\,. \tag{3.34}$$

Note that the Hertz vector $\vec{\Pi}$ in Ref. [94] is related to the vector potential by $\vec{\mathcal{A}} = \partial\vec{\Pi}/\partial t$. With this definition, the present theory agrees with that in Ref. [94].

Substituting Eq. (3.30) into Eq. (3.34), the vector potential is expressed as

$$\vec{A}\left(\vec{r},\omega\right) = \frac{\mu_0 i}{2}\int\int\int dV' \sum_{m,n\geq 0}\sum_{\nu=x,y,z} \vec{i}_\nu \vec{i}_\nu \frac{\phi_{mn\nu}\left(\vec{r}_\perp\right)\phi_{mn\nu}\left(\vec{r}'_\perp\right)}{k_z} \times \left[\theta(z-z')e^{ik_z(z-z')} + \theta(z'-z)e^{ik_z(z'-z)}\right]\cdot \vec{J}\left(\vec{r}',\omega\right). \tag{3.35}$$

Then Cartesian components of the vector potential can be written down as follows

$$A_\nu\left(\vec{r},\omega\right) = \frac{\mu_0 i}{2}\int\int\int dV' \sum_{m,n\geq 0} \frac{\phi_{mn\nu}\left(\vec{r}_\perp\right)\phi_{mn\nu}\left(\vec{r}'_\perp\right)}{k_z} \times \left[\theta(z-z')e^{ik_z(z-z')} + \theta(z'-z)e^{ik_z(z'-z)}\right] J_\nu\left(\vec{r}',\omega\right), \tag{3.36}$$

where $\nu = x,\ y,$ or z. For sake of convenience, here we define

$$\Gamma^+(z,z') = \theta(z-z')e^{ik_z(z-z')} + \theta(z'-z)e^{ik_z(z'-z)}, \tag{3.37}$$

which indicates the phase advance in the z-direction, and

$$A_\nu\left(\vec{r},\omega\right) = \sum_{m,n\geq 0} A_{mn\nu}\left(\vec{r},\omega\right). \tag{3.38}$$

Consequently, one only needs to concentrate on calculating the vector potential of a single mode, i.e. $A_{mn\nu}\left(\vec{r},\omega\right)$. The explicit forms of $A_{mn\nu}\left(\vec{r},\omega\right)$ are

$$A_{mnx}\left(\vec{r},\omega\right) = \frac{\mu_0 i}{2}\frac{4}{(1+\delta_{m0})ab}\frac{\phi'_{mnx}\left(x,y\right)}{k_z} \times \int\int\int dV'\ \phi'_{mnx}\left(x',y'\right)\Gamma^+(z,z')J_x(\vec{r}',\omega), \tag{3.39}$$

$$A_{mny}\left(\vec{r},\omega\right) = \frac{\mu_0 i}{2}\frac{4}{(1+\delta_{n0})ab}\frac{\phi'_{mny}\left(x,y\right)}{k_z} \times \int\int\int dV'\ \phi'_{mny}\left(x',y'\right)\Gamma^+(z,z')J_y(\vec{r}',\omega), \tag{3.40}$$

$$A_{mnz}\left(\vec{r},\omega\right) = \frac{\mu_0 i}{2}\frac{4}{ab}\frac{\phi'_{mnz}\left(x,y\right)}{k_z} \times \int\int\int dV'\ \phi'_{mnz}\left(x',y'\right)\Gamma^+(z,z')J_z(\vec{r}',\omega). \tag{3.41}$$

The scalar potential of a single mode can be calculated through Eq. (1.15) as follows

$$\begin{aligned}\tilde{\Phi}_{mnx}\left(\vec{r},\omega\right) &= \frac{c^2}{i\omega}\frac{\partial A_{mnx}}{\partial x} \\ &= \frac{c^2}{i\omega}\frac{\mu_0 i}{2}\frac{4}{(1+\delta_{m0})ab}\frac{-k_x\phi'_{mnz}\left(x,y\right)}{k_z} \\ &\times \int\int\int dV'\ \phi'_{mnx}\left(x',y'\right)\Gamma^{+}(z,z')J_x(\vec{r}',\omega), \end{aligned} \tag{3.42}$$

$$\begin{aligned}\tilde{\Phi}_{mny}\left(\vec{r},\omega\right) &= \frac{c^2}{i\omega}\frac{\partial A_{mny}}{\partial y} \\ &= \frac{c^2}{i\omega}\frac{\mu_0 i}{2}\frac{4}{(1+\delta_{n0})ab}\frac{-k_y\phi'_{mnz}\left(x,y\right)}{k_z} \\ &\times \int\int\int dV'\ \phi'_{mny}\left(x',y'\right)\Gamma^{+}(z,z')J_y(\vec{r}',\omega), \end{aligned} \tag{3.43}$$

and

$$\begin{aligned}\tilde{\Phi}_{mnz}\left(\vec{r},\omega\right) &= \frac{c^2}{i\omega}\frac{\partial A_{mnz}}{\partial z} \\ &= \frac{c^2}{i\omega}\frac{\mu_0 i}{2}\frac{4}{ab}i\phi'_{mnz}\left(x,y\right) \\ &\times \int\int\int dV'\ \phi'_{mnz}\left(x',y'\right)\Gamma^{-}(z,z')J_z(\vec{r}',\omega), \end{aligned} \tag{3.44}$$

where

$$\Gamma^{-}(z,z') = \theta(z-z')e^{ik_z(z-z')} - \theta(z'-z)e^{ik_z(z'-z)} \tag{3.45}$$

is calculated from

$$\frac{\partial\Gamma^{+}(z,z')}{\partial z} = ik_z\Gamma^{-}(z,z'). \tag{3.46}$$

It should be emphasized that $\tilde{\Phi}_{mnz}\left(\vec{r},\omega\right)$ is discontinuous at $z=z'$. Consequently, its derivative over z results in delta function as to be discussed later.

With the vector and scalar potential given, the electric fields of a single mode

can be calculated using Eq. (1.16b) as

$$
\begin{aligned}
&E_{mnx}(\vec{r},\omega) = i\omega A_{mnx} - \frac{\partial}{\partial x}(\tilde{\Phi}_{mnx} + \tilde{\Phi}_{mny} + \tilde{\Phi}_{mnz}) \\
&= i\omega\frac{\mu_0 i}{2}\frac{4}{(1+\delta_{m0})ab}\left(1 - \frac{k_x^2}{k^2}\right)\frac{\phi'_{mnx}(x,y)}{k_z} \\
&\times \int\int\int dV'\ \phi'_{mnx}(x',y')\,\Gamma^+(z,z')J_x(\vec{r}',\omega) \\
&+ i\omega\frac{\mu_0 i}{2}\frac{4}{(1+\delta_{n0})ab}\frac{-k_x k_y}{k^2}\frac{\phi'_{mnx}(x,y)}{k_z}\int\int\int dV'\ \phi'_{mny}(x',y')\,\Gamma^+(z,z')J_y(\vec{r}',\omega) \\
&+ i\omega\frac{\mu_0 i}{2}\frac{4}{ab}\frac{ik_x k_z}{k^2}\frac{\phi'_{mnx}(x,y)}{k_z}\int\int\int dV'\ \phi'_{mnz}(x',y')\,\Gamma^-(z,z')J_z(\vec{r}',\omega),
\end{aligned}
\tag{3.47}
$$

and

$$
\begin{aligned}
&E_{mny}(\vec{r},\omega) = i\omega A_{mny} - \frac{\partial}{\partial y}(\tilde{\Phi}_{mnx} + \tilde{\Phi}_{mny} + \tilde{\Phi}_{mnz}) \\
&= i\omega\frac{\mu_0 i}{2}\frac{4}{(1+\delta_{n0})ab}\left(1 - \frac{k_y^2}{k^2}\right)\frac{\phi'_{mny}(x,y)}{k_z} \\
&\times \int\int\int dV'\ \phi'_{mny}(x',y')\,\Gamma^+(z,z')J_y(\vec{r}',\omega) \\
&+ i\omega\frac{\mu_0 i}{2}\frac{4}{(1+\delta_{m0})ab}\frac{-k_x k_y}{k^2}\frac{\phi'_{mny}(x,y)}{k_z}\int\int\int dV'\ \phi'_{mnx}(x',y')\,\Gamma^+(z,z')J_x(\vec{r}',\omega) \\
&+ i\omega\frac{\mu_0 i}{2}\frac{4}{ab}\frac{ik_y k_z}{k^2}\frac{\phi'_{mny}(x,y)}{k_z}\int\int\int dV'\ \phi'_{mnz}(x',y')\,\Gamma^-(z,z')J_z(\vec{r}',\omega).
\end{aligned}
\tag{3.48}
$$

To obtain the longitudinal electric field representation, special attention is required in performing the differentiation with respect to z on $\tilde{\Phi}_{mnz}$. Because $\tilde{\Phi}_{mnz}$ is discontinuous at $z = z'$, care must be exercised to account for the jump in $\tilde{\Phi}_{mnz}$ as one crosses the $z = z'$ point. In fact, there exists

$$
\frac{\partial\Gamma^-(z,z')}{\partial z} = ik_z\Gamma^+(z,z') + 2\delta(z-z'). \tag{3.49}
$$

The delta function in the above equation accounts for the behavior of discontinuity at $z = z'$. Using the above equation, one can calculate the longitudinal

electric field as

$$
\begin{aligned}
&E_{mnz}(\vec{r},\omega) = i\omega A_{mnz} - \frac{\partial}{\partial z}(\tilde{\Phi}_{mnx} + \tilde{\Phi}_{mny} + \tilde{\Phi}_{mnz}) \\
&= i\omega\frac{\mu_0 i}{2}\frac{4}{ab}\left(1 - \frac{k_z^2}{k^2}\right)\frac{\phi'_{mnz}(x,y)}{k_z}\int\int\int dV'\ \phi'_{mnz}(x',y')\,\Gamma^+(z,z')J_z(\vec{r}',\omega) \\
&+ i\omega\frac{\mu_0 i}{2}\frac{4}{(1+\delta_{m0})ab}\frac{-ik_xk_z}{k^2}\frac{\phi'_{mnz}(x,y)}{k_z}\int\int\int dV'\ \phi'_{mnx}(x',y')\,\Gamma^-(z,z')J_x(\vec{r}',\omega) \\
&+ i\omega\frac{\mu_0 i}{2}\frac{4}{(1+\delta_{n0})ab}\frac{-ik_yk_z}{k^2}\frac{\phi'_{mnz}(x,y)}{k_z}\int\int\int dV'\ \phi'_{mny}(x',y')\,\Gamma^-(z,z')J_y(\vec{r}',\omega) \\
&+ i\omega\frac{\mu_0 i}{2}\frac{4}{ab}\frac{2ik_z}{k^2}\frac{\phi'_{mnz}(x,y)}{k_z}\int\int\int dV'\ \phi'_{mnz}(x',y')\,J_z(\vec{r}',\omega)\delta(z-z'). \qquad (3.50)
\end{aligned}
$$

The summation over indices m and n for the last term in the above equation gives

$$
\begin{aligned}
&E_z^0(\vec{r},\omega) = \sum_{m,n\geq 0} i\omega\frac{\mu_0 i}{2}\frac{4}{ab}\frac{2ik_z}{k^2}\frac{\phi'_{mnz}(x,y)}{k_z}\int\int\int dV'\ \phi'_{mnz}(x',y')\,J_z(\vec{r}',\omega)\delta(z-z') \\
&= i\omega\frac{\mu_0 i}{2}\frac{2i}{k^2}\int\int\int dV'\ \left[\sum_{m,n\geq 0}\frac{4}{ab}\phi'_{mnz}(x,y)\,\phi'_{mnz}(x',y')\right]J_z(\vec{r}',\omega)\delta(z-z') \\
&= i\omega\frac{\mu_0 i}{2}\frac{2i}{k^2}\int\int\int dV'\ \delta(x-x')\delta(y-y')\delta(z-z')J_z(\vec{r}',\omega) \\
&= \frac{-i\mu_0\omega}{k^2}J_z(\vec{r},\omega), \qquad (3.51)
\end{aligned}
$$

which indicates the field at the source region. In the above equation, the identity of

$$
\delta(x-x')\delta(y-y') = \sum_{m,n\geq 0}\frac{4}{ab}\phi'_{mnz}(x,y)\,\phi'_{mnz}(x',y') \qquad (3.52)
$$

has been utilized.

3.3 Fields of a point charge moving with constant velocity in a rectangular waveguide

Let us first calculate the fields generated by a point charge moving parallel to the axis of a rectangular waveguide. The particle velocity is assumed be to constant.

The waveguide has infinite length in the z direction and its walls are perfectly conductive. The charge and current densities can be defined by Dirac delta functions as follows

$$\varrho(\vec{r},t) = e\delta(x-x_0)\delta(y-y_0)\delta(z-vt), \tag{3.53a}$$

$$\vec{\jmath}(\vec{r},t) = \varrho(\vec{r},t)\vec{v} = \vec{i}_z ev\delta(x-x_0)\delta(y-y_0)\delta(z-vt). \tag{3.53b}$$

Then the spectra of charge and current densities can be calculated via Fourier transform. The results are

$$\rho(\vec{r},\omega) = \frac{e}{v}\delta(x-x_0)\delta(y-y_0)e^{i\omega z/v}, \tag{3.54a}$$

$$\vec{J}(\vec{r},\omega) = \rho(\vec{r},\omega)\vec{v} = \vec{i}_z e\delta(x-x_0)\delta(y-y_0)e^{i\omega z/v}. \tag{3.54b}$$

Note that it has been assumed that $c \geq v > 0$ in the above equations. Substituting Eq. (3.54b) into Eq. (3.34), the expression of vector potential can be obtained as follows

$$\begin{aligned}\vec{A}(\vec{r},\omega) = \mu_0\vec{i}_z \int\int\int dV' \, \frac{1}{2\pi}\sum_{m,n\geq 0}\int_{-\infty}^{\infty} d\beta \frac{\phi_{mnz}(\vec{r}_\perp)\,\phi_{mnz}(\vec{r}'_\perp)}{\beta^2-k_z^2}e^{i\beta(z-z')} \\ \times e\delta(x'-x_0)\delta(y'-y_0)e^{i\omega z'/v}.\end{aligned} \tag{3.55}$$

Note that Eq. (3.30) is used in the above equation instead of Eq. (3.31). And it is only because of convenience in calculations. Taking the volume of integration as

$$\int\int\int dV' = \int_0^a dx' \int_0^b dy' \int_{-\infty}^{\infty} dz', \tag{3.56}$$

the integrals over x', y' and z' can be easily performed in Eq. (3.55), resulting in

$$\vec{A}(\vec{r},\omega) = \mu_0 e\vec{i}_z \sum_{m,n\geq 0}\int_{-\infty}^{\infty} d\beta \frac{\phi_{mnz}(x,y)\,\phi_{mnz}(x_0,y_0)}{\beta^2-k_z^2}e^{i\beta z}\delta(\beta-\omega/v). \tag{3.57}$$

It is seen from above that the integration over z' leads to Dirac delta function. The factor $\delta(\beta-\omega/v)$ means that the fields produced by the point charge have the same phase velocity v as the particle itself [107]. And it is only true when the particle trajectory is considered to be infinitely long. The delta function

tremendously simplifies the integration over β in Eq. (3.55). Such simplification will not appear when a trajectory with finite length in CWR is considered, as will be seen in the next sections of this chapter. Integrating out β in Eq. (3.57) yields

$$\vec{A}(\vec{r},\omega) = \mu_0 e\vec{i}_z \sum_{m,n\geq 0} \frac{\phi_{mnz}(x,y)\,\phi_{mnz}(x_0,y_0)}{\omega^2/v^2 - k_z^2} e^{i\omega z/v}. \tag{3.58}$$

At this point the full expression of the vector potential is obtained for describing the fields generated by a point charge in a rectangular waveguide. Equation (3.58) indicates that the vector potential can be expanded in terms of 2D eigenfunctions which are defined on the waveguide cross section [107], while the corresponding eigenvalues are determined by applying boundary conditions. Replacing ω by $\omega = kc$ and v by $\beta_r = v/c$ where the subscript r is to distinguish from β which has been used as Fourier transform variable, Eq. (3.58) can be equivalently written as

$$\vec{A}(\vec{r},k) = \mu_0 e\vec{i}_z \sum_{m,n\geq 0} \frac{\phi_{mnz}(x,y)\,\phi_{mnz}(x_0,y_0)}{k^2(1/\beta_r^2 - 1) + k_x^2 + k_y^2} e^{ikz/\beta_r}. \tag{3.59}$$

From the above equation, the vector potential in the time domain can be calculated using inverse Fourier transform

$$\vec{\mathcal{A}}(\vec{r},t) = \frac{c}{2\pi}\int_{-\infty}^{\infty} dk\; e^{-ikct}\mu_0 e\vec{i}_z \sum_{m,n\geq 0} \frac{\phi_{mnz}(x,y)\,\phi_{mnz}(x_0,y_0)}{k^2(1/\beta_r^2 - 1) + k_x^2 + k_y^2} e^{ikz/\beta_r}. \tag{3.60}$$

Suppose $\beta_r < 1$, the above integral contains imaginary poles in the complex k-plane at

$$k_{mn} = \pm i\sqrt{\frac{k_x^2 + k_y^2}{1/\beta_r^2 - 1}} = \pm i\beta_r\gamma k_c. \tag{3.61}$$

The physical interpretation of the imaginary poles can be illustrated by Fig. 3.4. Since the particle velocity $v \leq c$, there is no coupling between the propagating modes and the beam mode in a vacuum waveguide with perfectly conducting walls, as synchronism can not be achieved. That is, in a dispersion diagram the beam mode line never crosses the dispersion curves of the propagating waves. But, the beam mode line does cross the dispersion curves of the slow waves, and

the crossing points exactly determine the imaginary poles as shown in the above equation. Taking contour integration and using residue theorem, the time-domain vector potential of Eq. (3.60) is achieved as follows

$$\vec{\mathcal{A}}\left(\vec{r},t\right)=\frac{\mu_0 e\beta_r c\gamma\vec{i}_z}{2}\sum_{m,n\geq 0}\frac{\phi_{mnz}\left(x,y\right)\phi_{mnz}\left(x_0,y_0\right)}{k_c}e^{-\gamma k_c|z-vt|}. \tag{3.62}$$

It is seen that the fields generated by a moving point charge exponentially decay as $s=|z-vt|$, which indicates the distance from the charge location. In fact, the above equation describes self-fields carried by the particle [107].

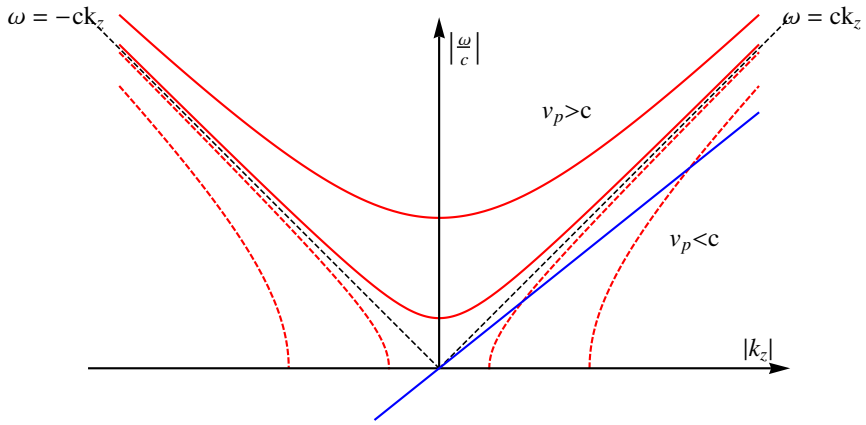

Figure 3.4: Dispersion relation for the waves excited by a point charge moving along a perfectly conducting waveguide with $v<c$. The solid blue line denotes the beam mode.

When $\beta_r\to 1$, the poles describe by Eq. (3.61) approach to infinity. Specially, if $v=c$, i.e. $\beta_r=1$, the term of k^2 in the denominator in Eq. (3.60) is cancelled. Then the k integral gives Dirac delta, resulting in

$$\vec{\mathcal{A}}\left(\vec{r},t\right)=\mu_0 ec\vec{i}_z\sum_{m,n\geq 0}\frac{\phi_{mnz}\left(x,y\right)\phi_{mnz}\left(x_0,y_0\right)}{k_c^2}\delta(z-ct). \tag{3.63}$$

The above result can also be derived from Eq. (3.62) by taking the limits $\beta_r\to 1$ and $\gamma\to\infty$. It is seen that, in the limit of $\beta_r\to 1$, the fields concentrate on the plane perpendicular to the z-direction.

The next step is to calculate the electric fields from the vector potential which has been obtained. Applying Eq. (3.59) to Eq. (1.16b), the three components of the electric fields are given as follows

$$E_x\left(\vec{r},k\right)=-\mu_0 e\beta_r c\gamma^2\frac{4}{ab}\sum_{m,n\geq 0}\frac{k_x\phi'_{mnx}\left(x,y\right)\phi'_{mnz}\left(x_0,y_0\right)}{k^2+\beta_r^2\gamma^2k_c^2}e^{ikz/\beta_r}, \tag{3.64a}$$

$$E_y\left(\vec{r},k\right)=-\mu_0 e\beta_r c\gamma^2\frac{4}{ab}\sum_{m,n\geq 0}\frac{k_y\phi'_{mny}\left(x,y\right)\phi'_{mnz}\left(x_0,y_0\right)}{k^2+\beta_r^2\gamma^2k_c^2}e^{ikz/\beta_r}, \tag{3.64b}$$

$$E_z\left(\vec{r},k\right)=-i\mu_0 ekc\frac{4}{ab}\sum_{m,n\geq 0}\frac{\phi'_{mnz}\left(x,y\right)\phi'_{mnz}\left(x_0,y_0\right)}{k^2+\beta_r^2\gamma^2k_c^2}e^{ikz/\beta_r}. \tag{3.64c}$$

Then the time-domain electric field components can be calculated via inverse Fourier transform. The results are

$$E_x\left(\vec{r},t\right)=-\frac{2\gamma e}{\epsilon_0 ab}\sum_{m,n\geq 0}\frac{k_x\phi'_{mnx}\left(x,y\right)\phi'_{mnz}\left(x_0,y_0\right)}{k_c}e^{-\gamma k_c|z-vt|}, \tag{3.65a}$$

$$E_y\left(\vec{r},t\right)=-\frac{2\gamma e}{\epsilon_0 ab}\sum_{m,n\geq 0}\frac{k_y\phi'_{mny}\left(x,y\right)\phi'_{mnz}\left(x_0,y_0\right)}{k_c}e^{-\gamma k_c|z-vt|}, \tag{3.65b}$$

$$E_z\left(\vec{r},t\right)=\frac{2e}{\epsilon_0 ab}\mathrm{sgn}(z-vt)\sum_{m,n\geq 0}\phi'_{mnz}\left(x,y\right)\phi'_{mnz}\left(x_0,y_0\right)e^{-\gamma k_c|z-vt|}, \tag{3.65c}$$

where $\mathrm{sgn}(z)$ denotes the sign function

$$\mathrm{sgn}\left(z\right)=\begin{cases}1 & \text{for} \quad z>0\\ 0 & \text{for} \quad z=0\\ -1 & \text{for} \quad z<0\end{cases}. \tag{3.66}$$

It is interesting that Eqs. (3.65) hold for all allowed values of particle velocity in the range of $0\leq\beta_r\leq 1$. When $\beta_r=0$ and $\gamma=1$, they represent the static fields of a point charge with shielding of the waveguide considered. When $\beta_r=1$, namely the particle moves with speed of light, one can take the limit approach of $\gamma\to\infty$ and obtains

$$E_x\left(\vec{r},t\right)=-\frac{2e}{\epsilon_0 ab}\sum_{m,n\geq 0}k_x\phi'_{mnx}\left(x,y\right)\phi'_{mnz}\left(x_0,y_0\right)\delta(z-vt), \tag{3.67a}$$

$$E_y(\vec{r},t) = -\frac{2e}{\epsilon_0 ab}\sum_{m,n\geq 0} k_y \phi'_{mny}(x,y)\,\phi'_{mnz}(x_0,y_0)\,\delta(z-vt), \tag{3.67b}$$

$$E_z(\vec{r},t) = 0. \tag{3.67c}$$

Up to now, the full expressions have been obtained for the electric fields generated by a point charge in a rectangular waveguide via eigenfunction method. The first straightforward application of these formulas would be to calculate the space-charge induced longitudinal and transverse impedance based on the general theory formulated in Chapter 1. For example, applying Eq. (3.64c) to Eq. (1.35) or Eq. (1.50), one can immediately get the longitudinal impedance per unit length for a point charge as follows

$$\frac{Z_\parallel(k)}{L} = i\mu_0 kc\frac{4}{ab}\sum_{m,n\geq 0}\frac{\phi'_{mnz}(x,y)\,\phi'_{mnz}(x_0,y_0)}{k^2+\beta_r^2\gamma^2 k_c^2}. \tag{3.68}$$

This is so called space-charge impedance with waveguide shielding taken into account. The expression is in form of expansion in terms of eigenfunctions, and it depends on the positions of both the source and test particles. The transverse impedance can be found in a similar way.

The most interesting observation from the previous calculations, which is intimately related to our topic of CWR (and also CSR), is that the space-charge (or particle/beam self-fields) effect is described by the imaginary poles in the frequency domain when eigenfunction method is applied. The poles are discretely distributed along the imaginary axis marked by the indices of the transverse eigenmodes. Existence of imaginary poles is the fundamental property of the fields generated by a moving charge. In most cases, specially in the ultra-relativistic limit, the space-charge effect can be neglected in beam instability theory. But in some cases, such as space charge with $\beta_r < 1$ (for instance, see Ref. [11]), resistive wall [11] or dielectric materials in a waveguide [107], charged beam moving along a curved trajectory(for instance, see Ref. [58]), the beam self-fields should be taken into account. In these cases, if eigenfunction method is applied (i.e. 2D eigenfunction expansion in the transverse plane, double Fourier transform in the z-direction and of time variable in the 3D bounded space), the beam self-fields will cause imaginary poles. The reason behind this conclusion is that the test particle which is put ahead of the source particle can feel fields in these cases as

listed previously. Thus the causality requirement (i.e. test particle ahead of the source particle does not feel fields or forces) in the conventional theory of beam instability (or impedance formalism) does not apply. For a non-causal system, when Fourier transform (or equivalent Laplace transform) is applied, singular poles usually appear in the upper half ω-plane.

3.4 Coherent wiggler radiation

3.4.1 Beam spectrum

In this section, the general theory of eigenfunction method demonstrated in the previous sections is applied to a practical case of wiggler radiation. Consider a straight rectangular pipe with infinite length, a wiggler is located at $0 \leq z \leq L$. The geometry of the problem is shown in Fig. 3.5. The source charge density is

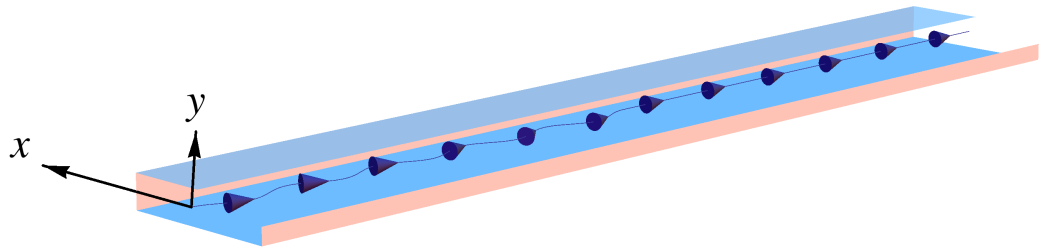

Figure 3.5: The geometry of the straight rectangular chamber for a wiggler. The beam moves along the curved line with arrows.

defined as

$$\varrho(\vec{r},t) = e\delta\left(x - x_t\right)\delta\left(y - y_t\right)\delta\left(z - z_t\right). \tag{3.69}$$

The beam orbit, as shown in Fig. 3.6 is defined in the $x - z$ plane as

$$x_t(t) = \begin{cases} x_0 & \text{for} \quad t < 0 \text{ or } t > \frac{L}{v} \\ \frac{\theta_0}{k_w}\sin\left(\omega_0 t\right) + x_0 & \text{for} \quad 0 \leq t \leq \frac{L}{v} \end{cases}, \tag{3.70a}$$

$$y_t(t) = y_0 \quad \text{for} \quad -\infty < t < \infty, \tag{3.70b}$$

$$z_t(t) = vt \quad \text{for} \quad -\infty < t < \infty, \tag{3.70c}$$

where $x_0 = a/2$, $y_0 = b/2$, $\theta_0 = \frac{K}{\gamma}$ and $k_w = \frac{\omega_0}{c}$. The parameter K is the strength parameter, γ is the relativistic factor, and k_w is the wavenumber of the wiggler. It is assume that $L = 2\pi N_u/k_w$ where N_u is integer, and the particle has constant velocity along z axis [89].

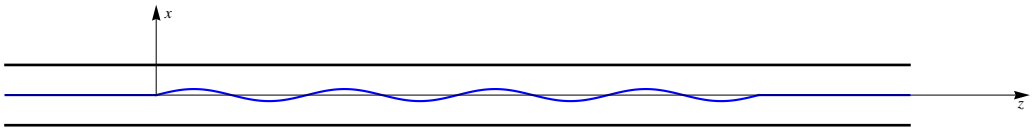

Figure 3.6: The beam orbit inside a wiggler. Note that the chamber width and orbit amplitude adopt different scale.

It follows from Eqs. (3.69) and (3.70) that the current density is

$$\vec{\mathcal{J}}\left(\vec{r},t\right) = \varrho(\vec{r},t)\vec{v}(t). \tag{3.71}$$

With $\vec{v}$ calculated from Eq. (3.70), the current densities in the three directions are found as follows

$$\mathcal{J}_x(\vec{r},t) = \begin{cases} 0 \quad \text{for} \quad t<0 \text{ or } t>\frac{L}{v} \\ ec\theta_0 \cos\left(\omega_0 t\right)\delta\left(\vec{r}-\vec{r}_t\right) \quad \text{for} \quad 0\le t\le\frac{L}{v} \end{cases}, \tag{3.72a}$$

$$\mathcal{J}_y(\vec{r},t) = 0 \quad \text{for} \quad -\infty < t < \infty, \tag{3.72b}$$

$$\mathcal{J}_z(\vec{r},t) = \begin{cases} ev\delta\left(\vec{r}-\vec{r}_0\right) \quad \text{for} \quad t<0 \text{ or } t>\frac{L}{v} \\ ev\delta\left(\vec{r}-\vec{r}_t\right) \quad \text{for} \quad 0\le t\le\frac{L}{v} \end{cases}, \tag{3.72c}$$

where

$$\delta\left(\vec{r}-\vec{r}_t\right) = \delta\left(x - \frac{\theta_0}{k_w}\sin\left(\omega_0 t\right) - x_0\right)\delta\left(y-y_0\right)\delta\left(z-vt\right) \tag{3.73}$$

and

$$\delta\left(\vec{r}-\vec{r}_0\right) = \delta\left(x-x_0\right)\delta\left(y-y_0\right)\delta\left(z-vt\right) \tag{3.74}$$

are the three-dimensional delta functions. Equation (3.72) is a full description of the source current density. If the particle moves parallel to the axis of the waveguide with constant velocity and does not conduct oscillation, it will not cause radiation fields. This case has been studied in Section 3.3. The fields

generated by the particle with uniform motion is not interesting right now. To calculate the wiggler radiation fields, it is better to define the source current density as

$$\mathcal{J}_x^U(\vec{r},t) = \begin{cases} 0 \quad \text{for} \quad t<0 \text{ or } t>\frac{L}{v} \\ ec\theta_0 \cos(\omega_0 t)\,\delta(\vec{r}-\vec{r}_t) \quad \text{for} \quad 0\le t\le \frac{L}{v} \end{cases}, \tag{3.75a}$$

$$\mathcal{J}_y^U(\vec{r},t) = 0 \quad \text{for} \quad -\infty < t < \infty, \tag{3.75b}$$

$$\mathcal{J}_z^U(\vec{r},t) = \begin{cases} 0 \quad \text{for} \quad t<0 \text{ or } t>\frac{L}{v} \\ ev\left(\delta(\vec{r}-\vec{r}_t)-\delta(\vec{r}-\vec{r}_0)\right) \quad \text{for} \quad 0\le t\le \frac{L}{v} \end{cases}. \tag{3.75c}$$

This current density is only due to the oscillating motion in the wiggler. Correspondingly, it is only necessary to calculate the radiation field $\vec{\mathcal{A}}^U(\vec{r},t)$. Since $\mathcal{J}_y^U(t)$ is always equal 0, one can easily conclude from Eq. (3.36) that there is no vertical component in $\vec{\mathcal{A}}^U(\vec{r},t)$. That is, there always is $\mathcal{A}_y^U(\vec{r},t)=0$.

Let us first calculate the spectrum of the current density using Fourier transform. For $\mathcal{J}_x^U(\vec{r},t)$, the delta function of transverse coordinates can be expanded as follows

$$\delta(x-x_t)\delta(y-y_t) = \frac{4}{ab}\sum_{m,n\ge 0}\frac{1}{1+\delta_{m0}}\phi'_{mnx}(x,y)\phi'_{mnx}(x_t,y_t). \tag{3.76}$$

With the above equation, one has

$$\mathcal{J}_x^U(\vec{r},t) = ec\theta_0 \sin(\omega_0 t)\delta(z-vt)\frac{4}{ab}\sum_{m,n\ge 0}\frac{1}{1+\delta_{m0}}\phi'_{mnx}(x,y)\phi'_{mnx}(x_t,y_t) \tag{3.77}$$

for $0 \le t \le L/v$. Equation (3.77) can be further expanded with the help of Jacobi-Anger expansion of exponentials of trigonometric functions in the basis of their harmonics. The Jacobi-Anger expansion is given by

$$e^{iz\cos(\psi)} = \sum_{p=-\infty}^{\infty} i^p J_p(z) e^{ip\psi}, \tag{3.78a}$$

and

$$e^{iz\sin(\psi)} = \sum_{p=-\infty}^{\infty} J_p(z) e^{ip\psi}, \tag{3.78b}$$

where $J_p(z)$ is the p-th Bessel function. Taking derivative over ψ on both sides of Eq. (3.78b) yields

$$\cos(\psi)e^{iz\sin(\psi)} = \frac{1}{z}\sum_{p=-\infty}^{\infty} pJ_p(z)e^{ip\psi} \quad \text{with} \quad z \neq 0. \tag{3.79}$$

Furthermore, using Jacobi-Anger expansion, one has

$$\begin{aligned}\cos(\omega_0 t)\phi'_{mnx}(x_t, y_t) &= \cos(\omega_0 t)\cos(k_x x_t)\sin(k_y y_0) \\ &= \frac{k_w}{2k_x\theta_0}\sum_{p=-\infty}^{\infty} pF_{mnp}e^{ip\omega_0 t},\end{aligned} \tag{3.80}$$

where it is assumed $k_x \neq 0$ and F_{mnp} is defined by

$$F_{mnp}(x_0, y_0) = \sin(k_y y_0)\left[e^{ik_x x_0} - (-1)^p e^{-ik_x x_0}\right] J_p(k_x\frac{\theta_0}{k_w}). \tag{3.81}$$

Substituting Eq. (3.80) into Eq. (3.77) yields

$$\mathcal{J}_x^U(\vec{r}, t) = \frac{eck_w}{2}\delta(z - vt)\sum_{m,n\geq 0}\sum_{p=-\infty}^{\infty}\frac{4}{(1+\delta_{m0})abk_x}\phi'_{mnx}(x, y)pF_{mnp}e^{ip\omega_0 t}. \tag{3.82}$$

At last the Fourier transform of $\mathcal{J}_x^U(\vec{r}, t)$ can be calculated as follows

$$\begin{aligned}J_x^U(\vec{r}, \omega) &= \int_{-\infty}^{\infty} dt\ \mathcal{J}_x^U(\vec{r}, t)e^{i\omega t} \\ &= \frac{eck_w}{2v}\sum_{m,n\geq 0}\sum_{p=-\infty}^{\infty}\frac{4}{(1+\delta_{m0})abk_x}pF_{mnp}\phi'_{mnx}(x, y)e^{i\beta_p z},\end{aligned} \tag{3.83}$$

where the quantity β_p is defined by

$$\beta_p = \frac{\omega + p\omega_0}{v}. \tag{3.84}$$

For $\mathcal{J}_z^U(\vec{r}, t)$, the delta function of transverse coordinates can be expanded as follows

$$\delta(x - x_t)\delta(y - y_t) = \frac{4}{ab}\sum_{m,n\geq 0}\phi'_{mnz}(x, y)\phi'_{mnz}(x_t, y_t). \tag{3.85}$$

With the above equation, the longitudinal current density can be written as

$$\mathcal{J}_z^U(\vec{r}, t) = ev\delta(z - vt)\frac{4}{ab}\sum_{m,n\geq 0}\left[\phi'_{mnz}(x, y)\phi'_{mnz}(x_t, y_t) - \phi'_{mnz}(x, y)\phi'_{mnz}(x_0, y_0)\right] \tag{3.86}$$

for $0 \leq t \leq L/v$.

Using the Jacobi-Anger expansion once more, one has

$$\phi'_{mnz}(x_t, y_t) = \sin(k_x x_t)\sin(k_y y_0) = \frac{1}{2i}\sum_{p=-\infty}^{\infty} F_{mnp} e^{ip\omega_0 t}. \tag{3.87}$$

Substituting Eq. (3.87) into Eq. (3.86) yields

$$\mathcal{J}_z^U(\vec{r}, t) = \frac{ev}{2i}\delta(z - vt)\sum_{m,n\geq 0}\sum_{\substack{p=-\infty \\ p\neq 0}}^{\infty} \frac{4}{ab}\phi'_{mnz}(x, y) F_{mnp} e^{ip\omega_0 t}. \tag{3.88}$$

Then the Fourier transform of $\mathcal{J}_z^U(\vec{r}, t)$ can be written as follows

$$\begin{aligned} J_z^U(\vec{r}, \omega) &= \int_{-\infty}^{\infty} dt\ \mathcal{J}_z^U(\vec{r}, t) e^{i\omega t} \\ &= \frac{e}{2i}\sum_{m,n\geq 0}\sum_{\substack{p=-\infty \\ p\neq 0}}^{\infty} \frac{4}{ab} F_{mnp}\phi'_{mnz}(x, y) e^{i\beta_p z}. \end{aligned} \tag{3.89}$$

3.4.2 Electric fields in a finite-length wiggler

The fields excited by a point charge moving along a wiggler can be interpreted by the dispersion relation as shown in Fig. 3.7. According to Eq. (3.84), the beam mode is shifted due to the wiggler. As sketched in the figure, the upshifted beam modes can couple with the propagating waveguide modes. This mode synchronism leads to the well-known wiggler radiation. On the other hand, the downshifted beam modes can couple with the slow waves. It leads to a kind of radiative fields similar to space-charge fields as discussed in the previous section. The crossing points between the beam modes and the fast/slow waves indicate real/imaginary poles in the complex wavenumber plane.

The radiation fields corresponding to the real poles is to be treated in this subsection. With the spectrum of a wiggling beam yielded, the electric fields can be calculated using the formulas obtained in Section 3.2.3. For the horizontal

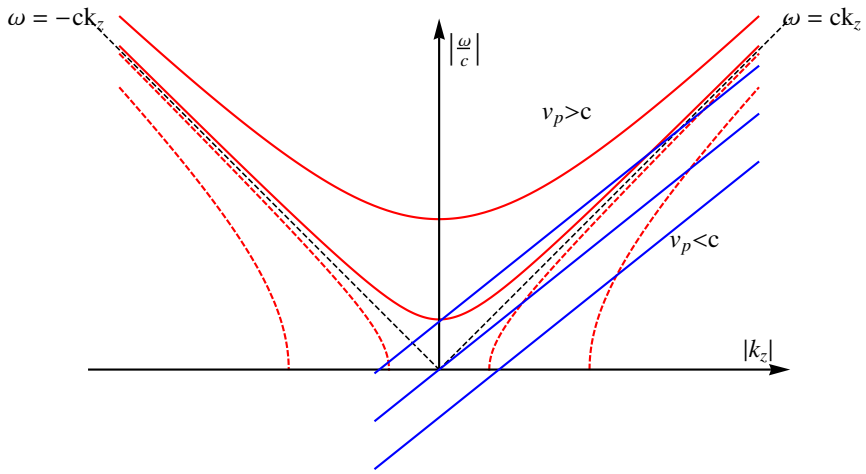

Figure 3.7: Dispersion relation for the waves excited by a point charge moving along a perfectly conducting waveguide sandwiched by a wiggler. The solid blue line denotes the beam mode.

electric field, the result is

$$
\begin{aligned}
E^U_{mnx}(\vec{r},\omega) &= i\omega\frac{\mu_0 i}{2}\frac{4}{(1+\delta_{m0})ab}\left(1-\frac{k_x^2}{k^2}\right)\frac{\phi'_{mnx}(x,y)}{k_z} \\
&\times\int_0^a dx'\int_0^b dy'\int_0^L dz'\;\phi'_{mnx}(x',y')\,\Gamma^+(z,z')J^U_x(\vec{r}',\omega) \\
&+ i\omega\frac{\mu_0 i}{2}\frac{4}{ab}\frac{ik_xk_z}{k^2}\frac{\phi'_{mnx}(x,y)}{k_z} \\
&\times\int_0^a dx'\int_0^b dy'\int_0^L dz'\;\phi'_{mnz}(x',y')\,\Gamma^-(z,z')J^U_z(\vec{r}',\omega).
\end{aligned}
\tag{3.90}
$$

One can define

$$
Y^+_{mnx} = \int_0^a dx'\int_0^b dy'\int_0^L dz'\;\phi'_{mnx}(x',y')\,\Gamma^+(z,z')J^U_x(\vec{r}',\omega), \tag{3.91}
$$

and

$$
Y^-_{mnz} = \int_0^a dx'\int_0^b dy'\int_0^L dz'\;\phi'_{mnz}(x',y')\,\Gamma^-(z,z')J^U_z(\vec{r}',\omega). \tag{3.92}
$$

Performing the integration over x', y' and z' yields

$$
Y^+_{mnx}(z) = \frac{eck_w}{2vk_x}\sum_{p=-\infty}^{\infty} pF_{mnp}Q^+_{mnp}(z), \tag{3.93}
$$

and

$$Y^{-}_{mnz}(z) = \frac{e}{2i} \sum_{\substack{p=-\infty \\ p\neq 0}}^{\infty} F_{mnp} Q^{-}_{mnp}(z), \tag{3.94}$$

where two quantities are defined as follows

$$Q^{+}_{mnp}(z) = e^{ik_z z} \frac{e^{i(\beta_p - k_z)z} - 1}{i(\beta_p - k_z)} + e^{-ik_z z} \frac{e^{i(\beta_p + k_z)L} - e^{i(\beta_p + k_z)z}}{i(\beta_p + k_z)}, \tag{3.95}$$

and

$$Q^{-}_{mnp}(z) = e^{ik_z z} \frac{e^{i(\beta_p - k_z)z} - 1}{i(\beta_p - k_z)} - e^{-ik_z z} \frac{e^{i(\beta_p + k_z)L} - e^{i(\beta_p + k_z)z}}{i(\beta_p + k_z)}. \tag{3.96}$$

Then the horizontal field is obtained as

$$\begin{aligned} E^{U}_{x}(\vec{r},\omega) &= i\omega \frac{i\mu_0 e}{4} \frac{4}{ab} \sum_{m,n\geq 0} \frac{\phi'_{mnx}(x,y)}{k_z} \\ &\times \sum_{\substack{p=-\infty \\ p\neq 0}}^{\infty} F_{mnp} \left[\left(1 - \frac{k_x^2}{k^2}\right) \frac{p k_w^v}{(1+\delta_{m0}) k_x} Q^{+}_{mnp}(z) + \frac{k_x k_z}{k^2} Q^{-}_{mnp}(z) \right], \end{aligned} \tag{3.97}$$

where $k_w^v = k_w c/v$.

Similarly, the expression for the longitudinal electric field is

$$\begin{aligned} E_z(\vec{r},\omega) &= i\omega \frac{i\mu_0 e}{4} \frac{4}{ab} \sum_{m,n\geq 0} \frac{\phi'_{mnz}(x,y)}{k_z} \\ &\times \frac{1}{i} \sum_{\substack{p=-\infty \\ p\neq 0}}^{\infty} F_{mnp} \left[\left(1 - \frac{k_z^2}{k^2}\right) Q^{+}_{mnp}(z) + \frac{k_z p k_w^v}{(1+\delta_{m0}) k^2} Q^{-}_{mnp}(z) \right] \\ &- \frac{i\mu_0 \omega}{k^2} J_z(\vec{r},\omega). \end{aligned} \tag{3.98}$$

3.4.3 Wake potential and impedance

Using the formulas for the electric fields, the longitudinal wake can be calculated as the work of the electric field done on the test particle. It is assumed that the test particle adopts the same orbit as the source particle does, but with a time

delay T. In general, T can be positive or negative values, indicating the test particle is behind or ahead of the source particle. The wake potential is

$$W(T) = -\frac{1}{e^2}\int\int\int dV \int_{T}^{T+\frac{L}{v}} dt\ \vec{\mathcal{J}}\left(\vec{r}, t-T\right)\cdot\vec{\mathcal{E}}^{U}\left(\vec{r}, t\right)$$
$$= -\frac{1}{e^2}\int\int\int dV \int_{0}^{\frac{L}{v}} dt\ \vec{\mathcal{J}}\left(\vec{r}, t\right)\cdot\vec{\mathcal{E}}^{U}\left(\vec{r}, t+T\right). \tag{3.99}$$

With the electric field replaced by its Fourier transform, the above equation is written as

$$W(T) = -\frac{1}{e^2}\int\int\int dV \int_{0}^{\frac{L}{v}} dt\ \vec{\mathcal{J}}\left(\vec{r}, t\right)\cdot\frac{1}{2\pi}\int_{-\infty}^{\infty} d\omega\ \vec{E}^{U}\left(\vec{r}, \omega\right)e^{-i\omega(t+T)}$$
$$= \frac{1}{2\pi}\int_{-\infty}^{\infty} d\omega\ \left[-\frac{1}{e^2}\int\int\int dV \int_{0}^{\frac{L}{v}} dt\ \vec{\mathcal{J}}\left(\vec{r}, t\right)\cdot\vec{E}^{U}\left(\vec{r}, \omega\right)e^{-i\omega t}\right]e^{-i\omega T}. \tag{3.100}$$

Since the Fourier transform of the wake is related to the impedance by

$$W\left(T\right) = \frac{1}{2\pi}\int_{-\infty}^{\infty} Z\left(\omega\right)e^{-i\omega T}d\omega, \tag{3.101}$$

the longitudinal CWR impedance can be expressed by

$$Z_{\parallel}(\omega) = -\frac{1}{e^2}\int\int\int dV \int_{0}^{\frac{L}{v}} dt\ \vec{\mathcal{J}}\left(\vec{r}, t\right)\cdot\vec{E}^{U}\left(\vec{r}, \omega\right)e^{-i\omega t}$$
$$= -\frac{1}{e^2}\int\int\int dV \int_{0}^{\frac{L}{v}} dt$$
$$\times\left[\mathcal{J}_x\left(\vec{r}, t\right)E_x^{U}\left(\vec{r}, \omega\right) + \mathcal{J}_z\left(\vec{r}, t\right)E_z^{U}\left(\vec{r}, \omega\right)\right]e^{-i\omega t}. \tag{3.102}$$

First the impedance due to the horizontal electric field is to be calculated

$$Z_{\parallel x}(\omega) = -\frac{1}{e^2}\int\int\int dV \int_{0}^{\frac{L}{v}} dt\ \mathcal{J}_x\left(\vec{r}, t\right)E_x^{U}\left(\vec{r}, \omega\right)e^{-i\omega t}$$
$$= -\frac{1}{e^2}\int\int\int dV \int_{0}^{\frac{L}{v}} dt\ ec\theta_0\cos\left(\omega_0 t\right)$$
$$\times\delta\left(x - \frac{\theta_0}{k_w}\sin\left(\omega_0 t\right) - x_0\right)\delta\left(y - y_0\right)\delta\left(z - vt\right)E_x^{U}\left(\vec{r}, \omega\right)e^{-i\omega t}. \tag{3.103}$$

Substituting Eq. (3.97) into the above equation and integrating over x, y and z yields

$$Z_{\parallel x}(\omega) = -\frac{1}{e^2}\int_0^{\frac{L}{v}} dt\ ec\theta_0 \cos(\omega_0 t) \times i\omega\frac{i\mu_0 e}{4}\frac{4}{ab}\sum_{m,n\geq 0}\frac{1}{k_z}\cos\left(k_x(\frac{\theta_0}{k_w}\sin(\omega_0 t)+x_0)\right)\sin(k_y y_0) \times \sum_{\substack{p=-\infty\\ p\neq 0}}^{\infty} F_{mnp}\left[\left(1-\frac{k_x^2}{k^2}\right)\frac{pk_w^v}{(1+\delta_{m0})k_x}Q^+_{mnp}(vt)+\frac{k_x k_z}{k^2}Q^-_{mnp}(vt)\right]e^{-i\omega t}. \quad (3.104)$$

Applying the same expansion as Eq. (3.80) to the above equation gives

$$Z_{\parallel x}(\omega) = -\int_0^{\frac{L}{v}} dt\ c\theta_0 i\omega\frac{i\mu_0 e}{4}\frac{4}{ab}\sum_{m,n\geq 0}\frac{1}{k_z}\frac{k_w}{2k_x\theta_0}\sum_{p'=-\infty}^{\infty} p' F_{mnp'}e^{ip'\omega_0 t} \times \sum_{\substack{p=-\infty\\ p\neq 0}}^{\infty} F_{mnp}\left[\left(1-\frac{k_x^2}{k^2}\right)\frac{pk_w^v}{(1+\delta_{m0})k_x}Q^+_{mnp}(vt)+\frac{k_x k_z}{k^2}Q^-_{mnp}(vt)\right]e^{-i\omega t}. \quad (3.105)$$

The integration over t can be done without difficulty, with the final result of

$$Z_{\parallel x}(\omega) = \frac{\mu_0 c}{2abk}\sum_{m,n\geq 0}\sum_{p'=-\infty}^{\infty}\sum_{\substack{p=-\infty\\ p\neq 0}}^{\infty}\frac{k_w^v}{k_z k_x}p' F_{mnp'}F_{mnp} \times\left[\left(k^2-k_x^2\right)\frac{pk_w^v}{(1+\delta_{m0})k_x}Q^+_{mnpp'}+k_x k_z Q^-_{mnpp'}\right], \quad (3.106)$$

where two quantities are defined as

$$Q^+_{mnpp'} = -\frac{iL}{\beta_p-k_z}\delta_{p(-p')}-\frac{e^{-i(\beta_{-p'}-k_z)L}-1}{(\beta_p-k_z)(\beta_{-p'}-k_z)} + \frac{iL}{\beta_p+k_z}\delta_{p(-p')}+\frac{1-e^{i(\beta_{-p'}+k_z)L}}{(\beta_p+k_z)(\beta_{-p'}+k_z)}, \quad (3.107)$$

and

$$Q^-_{mnpp'} = -\frac{iL}{\beta_p-k_z}\delta_{p(-p')}-\frac{e^{-i(\beta_{-p'}-k_z)L}-1}{(\beta_p-k_z)(\beta_{-p'}-k_z)} - \frac{iL}{\beta_p+k_z}\delta_{p(-p')}-\frac{1-e^{i(\beta_{-p'}+k_z)L}}{(\beta_p+k_z)(\beta_{-p'}+k_z)}, \quad (3.108)$$

with

$$\beta_{-p'} = \frac{\omega - p'\omega_0}{v}. \tag{3.109}$$

Secondly, the impedance due to the longitudinal electric field is to be calculated

$$\begin{aligned} Z_{\parallel z}(\omega) &= -\frac{1}{e^2}\int\int\int dV \int_0^{\frac{L}{v}} dt\ \jmath_z\left(\vec{r},t\right) E_z^U\left(\vec{r},\omega\right) e^{-i\omega t} \\ &= -\frac{1}{e^2}\int\int\int dV \int_0^{\frac{L}{v}} dt\ ev \\ &\times \delta\left(x - \frac{\theta_0}{k_w}\sin\left(\omega_0 t\right) - x_0\right)\delta\left(y - y_0\right)\delta\left(z - vt\right) E_z^U\left(\vec{r},\omega\right) e^{-i\omega t}. \end{aligned} \tag{3.110}$$

Substituting Eq. (3.98) into the above equation and integrating over x, y and z yields

$$\begin{aligned} Z_{\parallel z}(\omega) &= -\frac{1}{e^2}\int_0^{\frac{L}{v}} dt\ ev \\ &\times i\omega\frac{i\mu_0 e}{4}\frac{4}{ab}\sum_{m,n\geq 0}\frac{1}{k_z}\sin\left(k_x(\frac{\theta_0}{k_w}\sin\left(\omega_0 t\right) + x_0)\right)\sin(k_y y_0) \\ &\times \frac{1}{i}\sum_{\substack{p=-\infty \\ p\neq 0}}^{\infty} F_{mnp}\left[\left(1 - \frac{k_z^2}{k^2}\right)Q_{mnp}^{+}(vt) + \frac{k_z p k_w^v}{(1+\delta_{m0})k^2}Q_{mnp}^{-}(vt)\right]e^{-i\omega t} \\ &- \frac{1}{e^2}\int_0^{\frac{L}{v}} dt\ ev\frac{i\mu_0\omega}{k^2}\frac{e}{2i}\sum_{m,n\geq 0}\sum_{\substack{p=-\infty \\ p\neq 0}}^{\infty}\frac{4}{ab}F_{mnp} \\ &\times \sin\left(k_x(\frac{\theta_0}{k_w}\sin\left(\omega_0 t\right) + x_0)\right)\sin(k_y y_0)e^{i\beta_p vt}e^{-i\omega t}. \end{aligned} \tag{3.111}$$

The same expansion as Eq. (3.87) is applied to the above equation and yields

$$
\begin{aligned}
Z_{\parallel z}(\omega) = &- \int_0^{\frac{L}{v}} dt\ vi\omega \frac{i\mu_0}{4}\frac{4}{ab}\sum_{m,n\geq 0}\frac{1}{k_z}\frac{1}{2i}\left[\sum_{p'=-\infty}^{\infty} F_{mnp'}e^{ip'\omega_0 t}\right] \\
&\times \frac{1}{i}\sum_{\substack{p=-\infty \\ p\neq 0}}^{\infty} F_{mnp}\left[\left(1-\frac{k_z^2}{k^2}\right)Q^+_{mnp}(vt) + \frac{k_z p k_w^v}{(1+\delta_{m0})k^2}Q^-_{mnp}(vt)\right]e^{-i\omega t} \\
&- \int_0^{\frac{L}{v}} dt\ v\frac{i\mu_0\omega}{k^2}\frac{1}{2i}\sum_{m,n\geq 0}\sum_{\substack{p=-\infty \\ p\neq 0}}^{\infty}\frac{4}{ab}F_{mnp} \\
&\times \left[\sum_{p'=-\infty}^{\infty} F_{mnp'}e^{ip'\omega_0 t}\right]e^{i\beta_p v t}e^{-i\omega t}. \qquad (3.112)
\end{aligned}
$$

The integration over t can be done without difficulty, with the final result of

$$
\begin{aligned}
Z_{\parallel z}(\omega) = &\frac{\mu_0 c}{2abk}\sum_{m,n\geq 0}\sum_{p'=-\infty}^{\infty}\sum_{\substack{p=-\infty \\ p\neq 0}}^{\infty}\frac{1}{k_z}F_{mnp'}F_{mnp} \\
&\times \left[\left(k_z^2-k^2\right)Q^+_{mnpp'} - \frac{pk_w^v k_z}{1+\delta_{m0}}Q^-_{mnpp'} - 2ik_z L\delta_{p(-p')}\right]. \qquad (3.113)
\end{aligned}
$$

Equations (3.106) and (3.113) are the final results for the coherent radiation impedance of a wiggler with finite length. The expressions are quite general. It is seen that the formulas for the total CWR impedance contains summations over four indices: $m,\ n,\ p,$ and p'. The indices m and n indicate the mode numbers of the rectangular chamber. The indices p and p' represent the harmonic numbers of the source particle and the test particle, respectively.

For convenience of discussion, the impedance is re-written as the sum of the individual parts indicated as follows (m, n, p, p'), i.e.

$$
\begin{aligned}
Z_{mnpp'x}(\omega) = &\frac{\mu_0 c}{2abk}\frac{k_w^v}{k_z k_x}p' F_{mnp'}F_{mnp} \\
&\times \left[\left(k^2-k_x^2\right)\frac{pk_w^v}{(1+\delta_{m0})k_x}Q^+_{mnpp'} + k_x k_z Q^-_{mnpp'}\right], \qquad (3.114)
\end{aligned}
$$

and

$$
\begin{aligned}
Z_{mnpp'z}(\omega) = &\frac{\mu_0 c}{2abk}\frac{1}{k_z}F_{mnp'}F_{mnp} \\
&\times \left[\left(k_z^2-k^2\right)Q^+_{mnpp'} - \frac{pk_w^v k_z}{1+\delta_{m0}}Q^-_{mnpp'} - 2ik_z L\delta_{p(-p')}\right]. \qquad (3.115)
\end{aligned}
$$

According to the discussions in Sections 3.2.2, there exists an independent solution of Maxwell's equations which contains singular poles on the imaginary axis of ω-plane. With ω replaced by $i\omega$, the whole CWR theory can be re-derived. Similar to the discussions of imaginary poles in CSR [58], it is found that the impedances due to the imaginary poles have the same forms as Eqs. (3.106) and (3.113) but with imaginary argument $i\omega$. The detailed calculation is postponed until subsection 3.4.5.

3.4.4 Simplification of the solutions

The results of Eqs. (3.114) and (3.115) look complicated at the first sight. But more simplifications are possible. Firstly, the beam velocity can be assumed as $v = c$, and this is certainly true at high energy electron or positron accelerators. Then one has $\beta_p = k + pk_w$ and $\beta_{-p'} = k - p'k_w$.

The next simplification is based on the observation that the terms with $p = 0$ is negligible. This is obvious because that $p = 0$ indicates uniform beam motion. And the beam with uniform motion will not generate radiation fields.

It is noticed that Eqs. (3.107) and (3.108) indicate the amplitude of the CWR impedance. In the case of long wiggler with large period number N_u, $Q^+_{mnpp'}$ and $Q^-_{mnpp'}$ become highly peaked near the values of k which satisfy the equation

$$\beta_p - k_z = \beta_{-p'} - k_z = 0, \tag{3.116}$$

or

$$\beta_p + k_z = \beta_{-p'} + k_z = 0. \tag{3.117}$$

The straightforward implication of the above equations is that strong resonances happen when $p = -p'$. Thus the terms of $p = -p'$ are most important in calculating CWR impedance. Solving Eq. (3.116) gives the positions of the resonant frequencies

$$k_{mn} = \frac{-p^2k_w^2 - k_c^2}{2pk_w} \tag{3.118}$$

for $v = c$ and $p \neq 0$. In general, the resonant frequencies are

$$k_{mn} = \gamma^2 \left[-pk_w \pm \frac{v}{c}\sqrt{(pk_w)^2 - \frac{k_c^2}{\gamma^2}} \right] \tag{3.119}$$

for $v < c$. Here $\gamma = 1/\sqrt{1 - v^2/c^2}$ is the Lorentz factor.

The third simplification is related to the Bessel function in F_{mnp}. If $k_x \frac{\theta_0}{k_w} \ll 1$, the Bessel function can be approximated by its asymptotic form

$$J_p(k_x \frac{\theta_0}{k_w}) \approx \left(k_x \frac{\theta_0}{2k_w} \right)^p, \tag{3.120}$$

where $p > 0$. If $p < 0$, there exists $J_p(x) = (-1)^p J_{-p}(x)$. In the following, the case of $k_x \frac{\theta_0}{k_w} \ll 1$ will be studied. This condition indicates a wiggler with small deflecting angle of $\theta_0 = K/\gamma \ll 1$.

The last simplification comes from the beam orbit. The beam is assumed to enter the wiggler with $x_0 = a/2$ and $y_0 = b/2$, which are the values at the center of the waveguide.

With the above simplifications, the CWR impedance with first- and second-order harmonics can be calculated. For the first-order harmonics, summing up the terms with $|p| = |p'| = 1$ yields the result due to the real poles

$$Z_1(k) = Z_0 \theta_0^2 \Theta_1(k), \tag{3.121}$$

where the dimensionless function $\Theta_1(k)$ is

$$\begin{aligned} \Theta_1(k) = & \frac{L^2}{ab} \sum_{m=0}^{\infty} \sum_{n=0}^{\infty} \frac{k}{(1+\delta_{m0})k_z} \cos^2(k_x x_0) \sin^2(k_y y_0) \\ & \times \left\{ \left(\frac{k - k_z}{k - k_z + k_w} \right)^2 \left[S^+(\frac{(k - k_z - k_w)L}{2}) + \frac{i}{(k - k_z)L} \right] \right. \\ & \left. + \left(\frac{k + k_z}{k + k_z + k_w} \right)^2 \left[S^-(\frac{(k + k_z - k_w)L}{2}) - \frac{i}{(k + k_z)L} \right] \right\}, \end{aligned} \tag{3.122}$$

where two functions are defined

$$S^+(z) = \frac{\sin^2(z) + i\left[\sin(z)\cos(z) - z\right]}{z^2}, \tag{3.123}$$

and

$$S^-(z) = \frac{\sin^2(z) - i\left[\sin(z)\cos(z) - z\right]}{z^2}. \tag{3.124}$$

If $x_0 = a/2$ and $y_0 = b/2$, the summation in Eq. (3.122) only goes over even values of m and odd values of n.

As previously discussed, the CWR impedance is highly peaked around the resonances $k + pk_w - k_z = 0$. The profile of the impedance is mainly determined by the sink-like functions $S^+(z)$ and $S^-(z)$. The width of each peak can be estimated by $\mathrm{sinc}^2(x) = 1/2$. Correspondingly, for a wiggler with period N_u, $k - k_z - k_w$ is evaluated in the range of $k_w/(2N_u)$. If N_u is large enough, then $k_w/(2N_u) \ll 1$ and $k - k_z \approx k_w$.

For the second-order harmonics, summing up the terms with $|p| = |p'| = 2$ yields the result due to real poles

$$Z_2(k) = Z_0\theta_0^4\Theta_2(k), \tag{3.125}$$

where the dimensionless function $\Theta_2(k)$ is

$$\begin{aligned}\Theta_2(k) = {} & \frac{L^2}{ab}\sum_{m=1}^{\infty}\sum_{n=1}^{\infty}\frac{4k}{k_z}\sin^2(k_x x_0)\sin^2(k_y y_0) \\ & \times\left\{\frac{k_x^2}{(k-k_z+2k_w)^2}\left[S^+(\frac{(k-k_z-2k_w)L}{2}) - \frac{i(k-k_z+4k_w)}{4k_w^2 L}\right]\right. \\ & \left. + \frac{k_x^2}{(k+k_z+2k_w)^2}\left[S^-(\frac{(k+k_z-2k_w)L}{2}) + \frac{i(k+k_z+4k_w)}{4k_w^2 L}\right]\right\}.\end{aligned} \tag{3.126}$$

By comparing the amplitude of $Z_1(k)$ and $Z_2(k)$, it is seen that $\left|\frac{Z_2(k)}{Z_1(k)}\right|$ is in the order of $\frac{\theta_0^2 k_x^2}{k_w^2}$. In the case of $\frac{\theta_0^2 k_x^2}{k_w^2} \ll 1$, one can safely neglect the CWR impedance of high-order harmonics. And crossing terms between different harmonics are also negligible.

When doing summation over m and n, Eq. (3.122) converges slowly. To get better convergence performance, the function $\Theta_1(k)$ is split into two parts as follows

$$\Theta_1(k) = \Theta_1^L(k) + \Theta_1^H(k), \tag{3.127}$$

where

$$\Theta_1^L(k) = \frac{L^2}{ab}\sum_{m=0}^{\infty}\sum_{n=0}^{\infty}\frac{k}{(1+\delta_{m0})k_z}\cos^2(k_x x_0)\sin^2(k_y y_0)$$
$$\times\left\{\left(\frac{k-k_z}{k-k_z+k_w}\right)^2 S^+(\frac{(k-k_z-k_w)L}{2})\right.$$
$$\left.+\left(\frac{k+k_z}{k+k_z+k_w}\right)^2 S^-(\frac{(k+k_z-k_w)L}{2})\right\}, \tag{3.128}$$

and

$$\Theta_1^H(k) = \frac{iL}{ab}\sum_{m=0}^{\infty}\sum_{n=0}^{\infty}\frac{k}{(1+\delta_{m0})k_z}\cos^2(k_x x_0)\sin^2(k_y y_0)$$
$$\times\left[\frac{k-k_z}{(k-k_z+k_w)^2}-\frac{k+k_z}{(k+k_z+k_w)^2}\right]. \tag{3.129}$$

The low-order resonant modes dominate $\Theta_1^L(k)$, and therefore the summation over m and n converges quickly. On the other hand, $\Theta_1^H(k)$ converges slowly when doing summation over m and n. The reason is that high-order modes are more important in this term. To get better convergence performance in evaluating $\Theta_1^H(k)$, the summation over m and n can be changed to integration by using substitution of

$$\sum_{m=0}^{\infty}\sum_{n=0}^{\infty}\to\frac{1}{4}\int_0^{\infty}dm\int_0^{\infty}dn=\frac{ab}{4\pi^2}\int_0^{\infty}dk_x\int_0^{\infty}dk_y. \tag{3.130}$$

Then there is

$$\Theta_1^H(k) = \frac{iL}{ab}\frac{ab}{4\pi^2}\int_0^k dk_x\int_0^k dk_y\frac{k}{k_z}\left[\frac{k-k_z}{(k-k_z+k_w)^2}-\frac{k+k_z}{(k+k_z+k_w)^2}\right], \tag{3.131}$$

where x_0 and y_0 are set to $x_0 = a/2$ and $y_0 = b/2$. Using variable substitution of $k_x = r\sin(\theta)$ and $k_y = r\cos(\theta)$, the integration is changed to

$$\Theta_1^H(k) = \frac{iL}{4\pi^2}\int_0^k rdr\int_0^{\frac{\pi}{2}}d\theta\frac{k}{\sqrt{k^2-r^2}}$$
$$\times\left[\frac{k-\sqrt{k^2-r^2}}{(k-\sqrt{k^2-r^2}+k_w)^2}-\frac{k+\sqrt{k^2-r^2}}{(k+\sqrt{k^2-r^2}+k_w)^2}\right]. \tag{3.132}$$

The integration over θ gives a factor of $\pi/2$. Using another variable substitution of $r = k\sin(\psi)$, one gets

$$\begin{aligned}\Theta_1^H(k) &= \frac{iL}{8\pi}\int_0^{\frac{\pi}{2}} k\sin(\psi)k\cos(\psi)d\psi\frac{k}{k\cos(\psi)} \\ &\times\left[\frac{k(1-\cos(\psi)}{\left[k(1-\cos(\psi))+k_w\right]^2}-\frac{k(1+\cos(\psi)}{\left[k(1+\cos(\psi))+k_w\right]^2}\right] \\ &= \frac{ikL}{8\pi}\left[\int_0^1 dt\frac{t}{\left(t+\frac{k_w}{k}\right)^2}-\int_1^2 dt\frac{t}{\left(t+\frac{k_w}{k}\right)^2}\right]. \end{aligned} \tag{3.133}$$

The last integration can be easily done and the result is [108]

$$\begin{aligned}\Theta_1^H(k) = \frac{ikL}{8\pi}\Bigg[&\log\left(\frac{k+k_w}{k_w}\right) \\ &-\frac{2}{(1+k_w/k)(2+k_w/k)}-2\coth^{-1}\left(3+\frac{2k_w}{k}\right)\Bigg], \end{aligned} \tag{3.134}$$

where $\coth^{-1}(z)$ is the inverse hyperbolic cotangent function. The first term in the above square brackets is dominant. The second and third terms can be neglected at high frequency where $k/k_w \gg 1$. It is noteworthy that Eq. (3.134) does not contain a or b. The implication is that the effect of waveguide shielding is negligible in this term.

Before finishing this subsection, Eq. (3.121) is used to calculate the CWR impedance and compare with the results given by the numerical code CSRZ. The parameters for the wiggler and waveguide cross-section were chosen as the same as those in Fig. 2.22(a). The maximum wavenumber of interest is set to $k_{max} = 10\ \mathrm{mm}^{-1}$. According to Eq. (3.118), it is only essential to consider the dominant modes with their indices satisfying $k_{mn} < k_{max}$. And it corresponds to

$$m \le m_{max} = \frac{a}{\pi}\sqrt{2k_w k_{max} - k_w^2}, \tag{3.135a}$$

$$n \le n_{max} = \frac{b}{\pi}\sqrt{2k_w k_{max} - k_w^2}. \tag{3.135b}$$

According to the above equations, in the example the summation over m and n goes to maximum values of 11 and 3, respectivley. The results are plotted in Figures 3.8(a) and 3.8(b). It turns out that the analytical formula agrees well

with the numerical results in the real part impedance but not in the imaginary part. The problem will be fixed if the impedance due to imaginary poles is taken into account, as will be discussed in the next section.

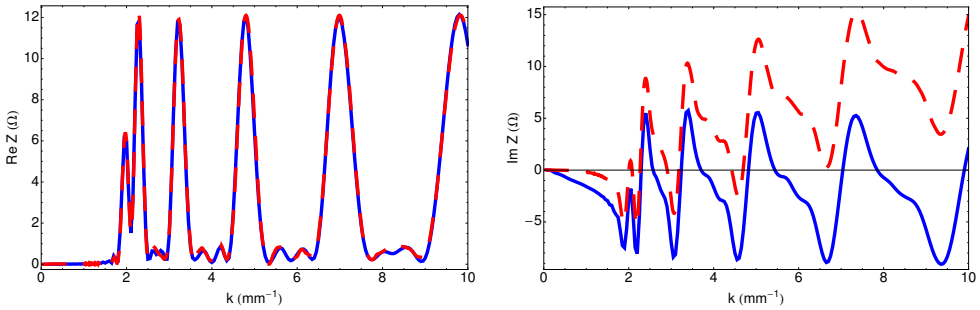

(a) Real part (b) Imaginary part

Figure 3.8: CWR impedance of a wiggler. The blue solid and red dashed lines represent analytic and numerical results, respectively.

As Eqs. (3.135) show, m_{max} and n_{max} are proportional to the chamber dimensions. This implies that when the chamber sizes become larger in which case the shielding effect would be weaker, the number of modes taken into account should go higher. Therefore, mode expansion method for calculating CWR impedance is more efficient for relatively small chambers.

It is also worth noting that the high order modes are non-negligible in Eq. (3.121) due to the term of $\frac{1}{k_z}$. It is obvious that $\frac{1}{k_z} \to \infty$ when $k \to k_c$, thus summing over higher order modes may give finite values. Let us test the same example discussed in the previous paragraphs. To calculate the CWR impedance, we sum the modes up to $m = \text{Min}[\frac{ka}{\pi}, \frac{ak_w}{\pi\theta_0}]$ and $n = kb/\pi$ at every wavenumber of k. Here the symbol Min[ ] stands for taking the minimum value of the quantities concerned. It comes from the approximation condition which was required in obtaining Eq. (3.121). The result is compared with that of blue lines in Figure 3.8(a) and 3.8(b). As shown in Figure 3.9(a) and 3.9(b), the real part impedance does not change at all when high order modes were taken into account, it implies that the lower order modes dominate the real part of CWR impedance. While for the imaginary part impedance, high order modes are also important and lead to a significant change of slope in the spectrum.

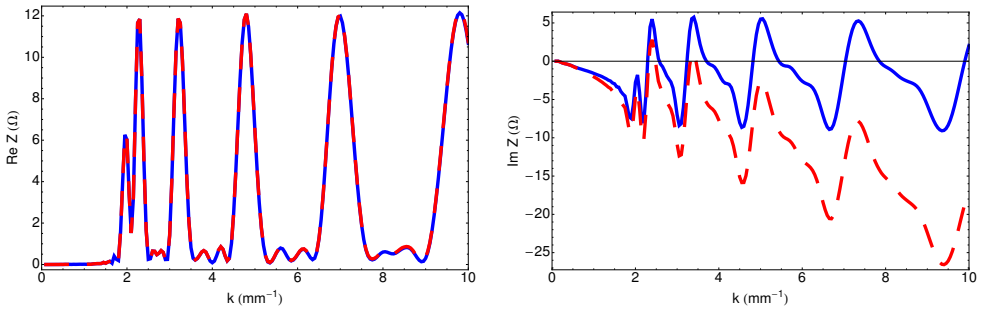

(a) Real part (b) Imaginary part

Figure 3.9: CWR impedance of a wiggler with high order modes considered. The blue solid represents the result with only low order modes considered; the red dashed line stands for the result with high order modes also taken into account.

3.4.5 CWR impedance due to imaginary frequencies

The impedance due to the imaginary frequencies is of importance in the CWR theory. This issue is discussed in this separate subsection.

In the previous subsections, it has been found that the fields generated by the wiggling beam propagate along the waveguide with the form of $\vec{\mathcal{A}} \propto e^{i(\omega t \pm k_z z)}$, where the plus and minus signs indicate the outward and inward waves, respectively. $k_z > 0$ denotes the propagating modes. For the conventionally defined evanescent modes, k is real and $k < \alpha_{mn}$. The fields of this kind of evanescent modes vanish exponentially along z axis. To take into account the evanescent modes with $k < \alpha_{mn}$, one can do the summations in Eqs. (3.106) and (3.113) beyond the cutoff. But, numerical tests almost give the same results as Fig. 3.8(b). It implies that the discrepancy shown in Fig. 3.8(b) is not due to the conventional evanescent modes.

The idea of considering imaginary poles was originated in Ref. [58]. As discussed in Section 3.3, the CWR impedance due to imaginary poles should be related to space-charge (or beam self-fields) effect. As did in Ref. [58], the trick is to do replacement $k \to ik$, and then re-derive the whole CWR theory. It was found that the CWR impedance due to imaginary poles can be described by

$$\bar{Z}_{mnpp'x}(\omega) = iZ_{mnpp'x}(i\omega), \tag{3.136a}$$

$$\bar{Z}_{mnpp'z}(\omega) = iZ_{mnpp'z}(i\omega). \tag{3.136b}$$

Suppose the wavenumber is purely imaginary, the wavenumbers k and k_z can be replaced by ik and $i\bar{k}_z = i\sqrt{k^2 + \alpha_{mn}^2}$, respectively. Keep in mind that here k and α_{mn} are real. All the derivations in the previous sections could then be repeated. It is found that all the formulas keep the same forms as those obtained previously. And the final impedance formula can be re-used when k and k_z are replaced by ik and $i\bar{k}_z$ as shown in Eqs. (3.136).

Simplifying the formula for first-ordr harmonic gives

$$\bar{Z}_1(k) = Z_0\theta_0^2\bar{\Theta}_1(k), \tag{3.137}$$

where

$$\begin{aligned}\bar{\Theta}_1(k) = {} & \frac{i}{ab}\sum_{m=0}^{\infty}\sum_{n=0}^{\infty}\frac{k}{(1+\delta_{m0})\bar{k}_z}\cos^2(k_x x_0)\sin^2(k_y y_0) \\ & \times\left\{\frac{(\bar{k}_z - k)\left[L\left((\bar{k}_z - k)^2 + k_w^2\right) + 2(\bar{k}_z - k)(e^{-(\bar{k}_z - k)L} - 1)\right]}{\left[(\bar{k}_z - k)^2 + k_w^2\right]^2}\right. \\ & \left. + \frac{(\bar{k}_z + k)\left[L\left((\bar{k}_z + k)^2 + k_w^2\right) + 2(\bar{k}_z + k)(e^{-(\bar{k}_z + k)L} - 1)\right]}{\left[(\bar{k}_z + k)^2 + k_w^2\right]^2}\right\}.\end{aligned} \tag{3.138}$$

The second term in the curly braces is small comparing with the first term. It will be neglected in the following calculations. Assumed that $x_0 = a/2$ and $y_0 = b/2$, the summation over m goes to even numbers and n goes to odd numbers. Consequently, the summation over m and n can be changed to integration as what is did in the previous section. The result is

$$\begin{aligned}\bar{\Theta}_1(k) \approx {} & \frac{i}{4\pi^2}\int_0^{\infty} dk_x \int_0^{\infty} dk_y \, \frac{k}{\bar{k}_z} \\ & \times \frac{(\bar{k}_z - k)\left[L\left((\bar{k}_z - k)^2 + k_w^2\right) + 2(\bar{k}_z - k)(e^{-(\bar{k}_z - k)L} - 1)\right]}{\left[(\bar{k}_z - k)^2 + k_w^2\right]^2}.\end{aligned} \tag{3.139}$$

By using variable substitution of $k_x = r\cos\theta$ and $k_y = r\sin\theta$, the integration

was changed to

$$\bar{\Theta}_1(k) \approx \frac{i}{4\pi^2}\int_0^\infty r dr \int_0^{\frac{\pi}{2}} d\theta \; \frac{k}{\bar{k}_z} \times \frac{(\bar{k}_z - k)\left[L\left((\bar{k}_z - k)^2 + k_w^2\right) + 2(\bar{k}_z - k)(e^{-(\bar{k}_z - k)L} - 1)\right]}{\left[(\bar{k}_z - k)^2 + k_w^2\right]^2} \tag{3.140}$$

with $\bar{k}_z = \sqrt{k^2 + r^2}$. The integration over θ is straightforward. One more variable substitution is to be done: $r = k\tan\psi$, resulting in $rdr = k^2 \tan\psi \sec^2\psi d\psi$ and $\bar{k}_z = k\sec\psi$. With more calculations, the integration becomes

$$\bar{\Theta}_1(k) \approx \frac{i}{8\pi}\int_0^{\frac{\pi}{2}} \tan\psi \sec\psi d\psi \times \frac{(\sec\psi - 1)\left[kL\left((\sec\psi - 1)^2 + k_w^2/k^2\right) + 2(\sec\psi - 1)(e^{-(\sec\psi - 1)kL} - 1)\right]}{\left[(\sec\psi - 1)^2 + k_w^2/k^2\right]^2}. \tag{3.141}$$

Since $\tan\psi\sec\psi d\psi = d\sec\psi$, one more simplification can be done:

$$\bar{\Theta}_1(k) \approx \frac{i}{8\pi}\int_1^\infty dt \times \frac{(t-1)\left[kL\left((t-1)^2 + k_w^2/k^2\right) + 2(t-1)(e^{-(t-1)kL} - 1)\right]}{\left[(t-1)^2 + k_w^2/k^2\right]^2}. \tag{3.142}$$

Another step of integral by parts yields

$$\int_1^\infty dt \frac{2(t-1)^2(e^{-(t-1)kL} - 1)}{\left[(t-1)^2 + k_w^2/k^2\right]^2} = \int_1^\infty dt \frac{e^{-(t-1)kL}\left(1 - kL(t-1)\right) - 1}{(t-1)^2 + k_w^2/k^2}. \tag{3.143}$$

With the above calculations, the integral of Eq. (3.142) can be changed to

$$\bar{\Theta}_1(k) \approx \frac{i}{8\pi}\int_1^\infty dt \; \frac{(t-1)kL - 1 + e^{-(t-1)kL}\left(1 - kL(t-1)\right)}{(t-1)^2 + k_w^2/k^2}. \tag{3.144}$$

The above equation can be evaluated by symbolic computation using Mathematica [109]. The result is

$$\bar{\Theta}_1(k) \approx \frac{ikL}{8\pi}\left[-\log\left(\frac{k_w}{k}\right) + C(k_w L)\right], \tag{3.145}$$

where

$$C(z) = \mathrm{Ci}(z) - \frac{\mathrm{Si}(z)}{z}, \tag{3.146}$$

and $\mathrm{Ci}(z) = -\int_z^\infty \cos(t)/t \; dt$ and $\mathrm{Si}(z) = \int_0^z \sin(t)/t \; dt$ are the cosine and sine integral functions, respectively. Since $k_w L = 2N_u\pi$, if the period of the wiggler is large, there exists $C(z) \to 0$. So the quantity $C(k_w L)$ in Eq. (3.145) can be neglected, resulting in

$$\bar{\Theta}_1(k) \approx -\frac{ikL}{8\pi} \log\left(\frac{k_w}{k}\right). \tag{3.147}$$

Adding Eq. (3.137) to Eq. (3.121), the new imaginary part is plotted in Fig. 3.10. It shows that the discrepancy in Figure 3.8(b) is well mitigated. The remaining

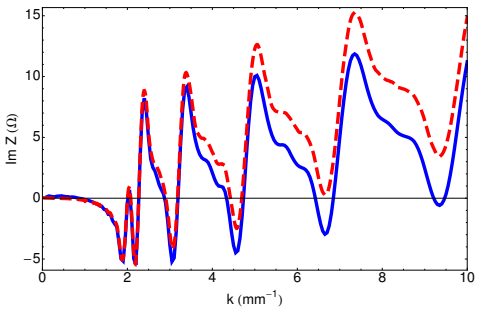

Figure 3.10: Imaginary part of the CWR impedance. The blue solid and red dashed lines represent analytic and numerical results, respectively.

discrepancy may be due to the paraxial approximation which is adopted in numerical calculations. Similar to the discussions in Ref. [58], we do find that the imaginary poles also play an important role in the CWR theory.

3.4.6 An infinite long wiggler

Consider that the wiggler is infinitely long. A particle traversing the wiggler takes the orbit as follows

$$x_t(t) = \frac{\theta_0}{k_w} \sin(\omega_0 t) + x_0, \tag{3.148a}$$

$$y_t(t) = y_0, \tag{3.148b}$$

$$z_t(t) = vt + z_0, \tag{3.148c}$$

with $-\infty < t < \infty$. It is seen that the beam spectrum has the same form as derived in the previous subsection.

Suppose that a test particle follows the source particle entering the wiggler with time difference T. We are to calculate the total work done by the CWR fields with a path length of L. Instead of using Eq. (3.32), Eq. (3.30) is directly substituted into Eq. (3.34). In combination with Eqs. (3.83) and (3.89), the vector potential due to a single mode are calculated as follows

$$A_{mnx}(\vec{r},\omega) = \frac{4\mu_0}{(1+\delta_{m0})ab}\frac{ek_w^v}{2k_x}\sum_{p=-\infty}^{\infty}\frac{pF_{mnp}}{\beta_p^2-k_z^2}\phi'_{mnx}(x,y)e^{i\beta_p z}, \tag{3.149}$$

and

$$A_{mnz}(\vec{r},\omega) = \frac{4\mu_0}{ab}\frac{e}{2i}\sum_{p=-\infty}^{\infty}\frac{F_{mnp}}{\beta_p^2-k_z^2}\phi'_{mnz}(x,y)e^{i\beta_p z}. \tag{3.150}$$

To obtain the above equations, the integration over z' is firstly done and it leads to Dirac delta function, i.e.

$$\int_{-\infty}^{\infty} dz' e^{i(\beta_p-\beta)z'} = 2\pi\delta(\beta-\beta_p). \tag{3.151}$$

Then the integration over β is easily done. The integrations over x' and y' are also straightforward. It is noteworthy that the cross terms of different eigenmodes are canceled due to their orthogonal property.

Using Eq. (1.16b), the horizontal and longitudinal compoents of the electric field can be calculated as follows

$$\begin{aligned} E_x(\vec{r},\omega) =& i\omega\frac{4\mu_0}{ab}\frac{e}{2}\sum_{m,n\geq 0}\sum_{p=-\infty}^{\infty}\left[(1-\frac{k_x^2}{k^2})\frac{pk_w^v}{(1+\delta_{m0})k_x}+\frac{\beta_p k_x}{k^2}\right] \\ &\times\frac{F_{mnp}}{\beta_p^2-k_z^2}\phi'_{mnx}(x,y)e^{i\beta_p z}, \end{aligned} \tag{3.152}$$

and

$$\begin{aligned} E_z(\vec{r},\omega) =& i\omega\frac{4\mu_0}{ab}\frac{e}{2i}\sum_{m,n\geq 0}\sum_{p=-\infty}^{\infty}\left[1-\frac{k_x^2}{k^2}+\frac{\beta_p}{k^2}\frac{pk_w^v}{1+\delta_{m0}}\right] \\ &\times\frac{F_{mnp}}{\beta_p^2-k_z^2}\phi'_{mnz}(x,y)e^{i\beta_p z}. \end{aligned} \tag{3.153}$$

The impedances are found to be

$$Z_{\parallel x}(\omega) = \frac{i\mu_0 ckL}{ab} \sum_{m,n\geq 0} \sum_{p=-\infty}^{\infty} \frac{pk_w^v}{k_x} \frac{F_{mnp}F_{mn(-p)}}{\beta_p^2 - k_z^2} \times \left[\left(1 - \frac{k_x^2}{k^2}\right) \frac{pk_w^v}{(1+\delta_{m0})k_x} + \frac{\beta_p k_x}{k^2} \right], \tag{3.154}$$

and

$$Z_{\parallel z}(\omega) = \frac{i\mu_0 ckL}{ab} \sum_{m,n\geq 0} \sum_{p=-\infty}^{\infty} \frac{F_{mnp}F_{mn(-p)}}{\beta_p^2 - k_z^2} \left[1 - \frac{\beta_p^2}{k^2} + \frac{\beta_p}{k^2} \frac{pk_w^v}{1+\delta_{m0}} \right]. \tag{3.155}$$

Summing up the above impedances together, the total impedance is given as follows

$$Z_{\parallel}(\omega) = \frac{i\mu_0 ckL}{ab} \sum_{m,n\geq 0} \sum_{p=-\infty}^{\infty} \frac{F_{mnp}F_{mn(-p)}}{(\beta_p^2 - k_z^2)k_x^2} \frac{c^2}{(1+\delta_{m0})v^2} \left[p^2 k_w^2 - \frac{k_x^2}{\gamma^2} \right]. \tag{3.156}$$

Since the term of $F_{mnp}F_{mn(-p)}$ is always real value, the above results are apparently imaginary and contain singular poles at $\beta_p^2 - k_z^2 = 0$. This feature is very similar to that of steady-state CSR, as discussed in Ref. [58]. Consider the

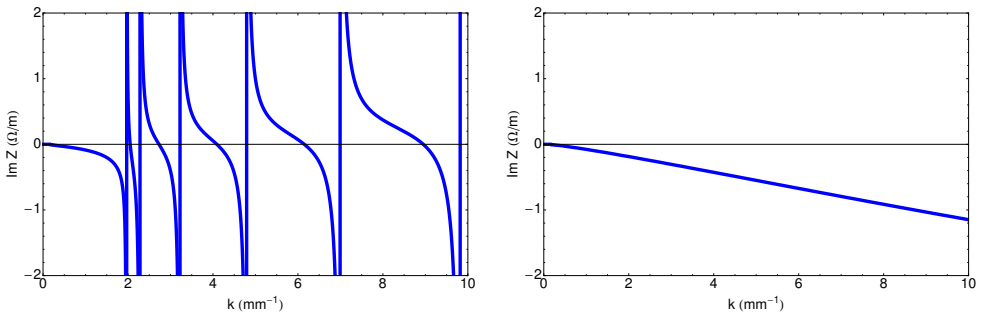

(a) $p = -1$ (b) $p = 1$

Figure 3.11: Imaginary part of the CSR impedance of an infinitely long wiggler with $p = -1$ and $p = 1$.

first-order harmonics and assume $v = c$, the CWR impedances per unit length are plotted in Fig. 3.11(a) for $p = -1$ and Fig. 3.11(b) for $p = 1$ with wiggler parameters the same as those of Fig. 2.22(a). It is noteworthy that Eq. (3.156) can be derived from Eq. (3.121) by taking the limit of $N_u \to \infty$. By taking the oscillation amplitude $\theta_0 \to 0$, one can easily see that Eq. (3.156) reduces to the space-charge impedance of Eq. (3.68).

4

Microwave instability

4.1 Introduction

There are tremendous studies on the single-bunch instabilities in storage rings (for examples, see Refs. [110, 111, 112, 113]) or linacs in the literature. The collective effects originating from CSR have been studied for many years (for instances, see Refs. [30, 64, 114, 115, 116, 117, 118, 119, 120, 121, 122, 123, 124]). A review on the theory and simulations of microbunch instability can be found in Ref. [125]. The single-bunch instabilities may occur in the longitudinal direction alone, or in the coupled system between the longitudinal and the transverse directions due to the dispersion effect (for example, see Ref. [126]). In general when the bunch length gets shorter in accelerators from storage rings to linacs, the CSR effects become more of importance. This chapter is dedicated to addressing microwave instability (MWI) with CSR taken into account in electron storage rings.

The CSR instability in several storage rings was investigated in Ref. [127] using existing theories on estimates of the instability threshold. A comprehensive overview of microwave instability theories was given in Ref. [128]. Handy formulas based on steady-state CSR models are now available for a simple estimation of CSR induced MWI threshold for an electron or positron ring. If the ring operates well above the MWI threshold, numerical simulations are proper for predicting the turn-by-turn beam dynamics (for instance, see Ref. [120]).

A simple coasting beam model was first developed in Ref. [129] to predict the CSR driven MWI in electron storage rings. Using free-space CSR impedance

model of Eq. (2.1), the theory gives a bunch population threshold for the instability [129, 130, 131]

$$N_{th1} = \frac{CI_A}{ce}\frac{\pi^{1/6}\alpha_p\gamma\sigma_\delta^2\sigma_z}{\sqrt{2}R^{1/3}\lambda^{2/3}}, \tag{4.1}$$

where C is the circumference of the ring, α_p is the momentum compaction, σ_δ is the relative energy spread, σ_z is the rms bunch length, R is the bending radius of dipoles, and λ is the specific wavelength. Following the notations of Ref. [128], I_A is Alfvén current defined by

$$I_A = 4\pi\epsilon_0\frac{m_e c^3}{e}, \tag{4.2}$$

where m_e is the electron mass. When applying the steady-state parallel-plates model of Eq. (2.3) to the coasting beam theory, a threshold independent of wavelengths was found [128] as follows

$$N_{th2} = \frac{CI_A}{ce}\frac{3\sqrt{2}\alpha_p\gamma\sigma_\delta^2\sigma_z}{\pi^{3/2}b}, \tag{4.3}$$

where b is the distance between the plates. It is noteworthy that the wavelength does not appear in the above equation. Furthermore, the instability threshold for a bunched beam is given in Ref. [124]

$$N_{th3} = \frac{CI_A}{ce}\frac{\alpha_p\gamma\sigma_\delta^2}{\sigma_z}\frac{\sigma_z^{4/3}}{R^{1/3}}\xi_{th}. \tag{4.4}$$

In the above equation, the quantity ξ_{th} is an empirical function determined from numerical simulations [128]

$$\xi_{th} = 0.5 + 0.34\chi, \tag{4.5}$$

where the dimensionless parameter χ is so called shielding parameter

$$\chi = \sigma_z\sqrt{\frac{R}{b^3}}. \tag{4.6}$$

It is interesting to compare Eqs. (4.3) and (4.4) by defining a ratio of

$$F(\chi) = N_{th2}/N_{th3} = \frac{3\sqrt{2}\chi^{2/3}}{\pi^{3/2}(0.5 + 0.34\chi)}. \tag{4.7}$$

The above function is plotted in Fig. 4.1. It is seen that for a large range of values of χ, F is close to 1. It infers that, for $\chi > 2$, the coasting beam theory with the parallel-plates CSR model has general agreements with the bunched theory. That is, Equation (4.3) is good enough for estimating the CSR instability threshold. This has been pointed out in Ref. [128]. It is also interesting to point out the significant discrepancy at very large values of χ. More careful studies are needed to fully understand it.

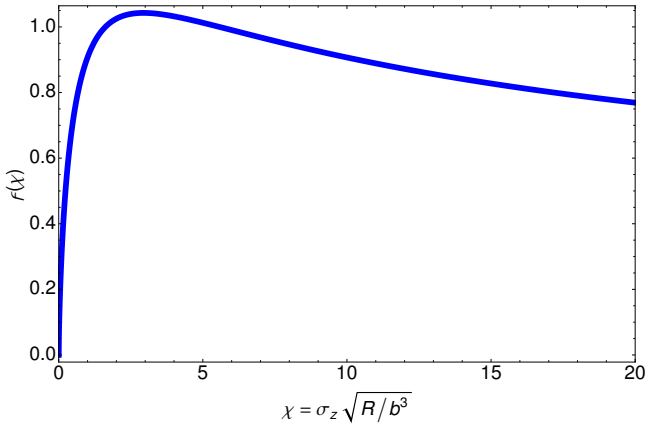

Figure 4.1: Ratio of the thresholds of coasting beam model to the bunched beam model, as a function of shielding parameter.

It is easy to see that shielding is negligible for $\chi \ll 1$. For free space CSR model, $\chi = 0$, equalizing Eqs. (4.1) and (4.4) gives a critical wavelength of $\lambda_{th} = (8\pi)^{1/4}\sigma_z \approx 2.24\sigma_z$. This wavelength is very close to the full width at half maximum (FWHM) for a Gaussian distribution. It indicates that for a Gaussian bunch, radiation at wavelength of λ_{th} is strongest and causes instability at the lowest bunch current.

Actually the shielding parameter χ is intimately related to the characteristic path difference between the beam and the radiation waves reflecting back from the metal walls. This is to be discussed in the next section.

The threshold given by Eq. (4.4) also suggests measures for avoiding CSR instability in a storage ring. The criterion is to push the MWI threshold as high as possible. By defining a machine parameter as

$$F = C\alpha_p\gamma\sigma_\delta^2\left(\frac{\sigma_z}{R}\right)^{1/3}\xi_{th} \tag{4.8}$$

from Eq. (4.4), the simple rule is to maximize the parameter F. It is obvious that F is intimately related to the details of the optics design. It is seen that the chamber height has been included in the parameter F. It is obvious that decreasing the chamber height leads to higher instability threshold.

4.2 Deviations from steady-state models

The instability analysis in the previous section is based on steady-state CSR model in free space or with parallel-plates shielding. Actually in a realistic storage ring, dipole magnets are interleaved with drifts. The chamber is usually toroidal inside the dipoles and is straight in the drifts. The vacuum chamber acts as a waveguide. Guided CSR fields can propagate along with the beam. While using the simple steady-state CSR model, transient effect, toroidal chamber shielding effect and multi-bend interference effect should be checked. These effects may make difference in evaluations of CSR instability threshold.

Transient effect is related to the magnet length. The beam starts to generate radiation when entering a bending magnet. The radiation stops once the beam moves into drift space. The build-up of the radiation is characterized by an overtaking length of [64]

$$L_{th1} = \left(24R^2\sigma_z\right)^{1/3}, \tag{4.9}$$

where R is the bending radius of the dipole magnet and σ_z indicates the rms bunch length. If the magnet length is much longer than L_{th1}, transient effect can be fairly neglected. The transient effect was also studied from the viewpoint of impedance in Chapter 2. Note that Eq. (4.9) has no information of the dimensions of the chamber. It is only determined by the curvature of the beam orbit and the bunch length.

The shielding of the chamber walls can be considered as follows: the beam emits radiation fields which propagate away from the beam. The radiation fields are reflected by the chamber walls and may act back to the beam. The shielding effect depends on the wavelength of the radiation fields. The criteria should be drawn from comparing the wavelengths $\lambda = 2\pi/k$ with the geometry of the chamber. Suppose that the chamber cross section is rectangular and the beam

is moving along the center of the chamber. The critical wavenumbers related to chamber geometries were found in Ref. [58] as follows

$$k_{th1} = \frac{3}{2}\sqrt{\frac{R}{a^3}}, \tag{4.10}$$

$$k_{th2} = \sqrt{\frac{2R}{3}\left(\frac{\pi}{b}\right)^3}, \tag{4.11}$$

where a and b indicate the chamber width and height, respectively. It is stated in Ref. [58] that at wavenumbers $k \gg k_{th1}$ and $k \gg k_{th2}$, toroidal chamber shielding is negligible. The above critical wavenumbers define critical bunch lengths by $\sigma_{zth1} = 1/k_{th1}$ and $\sigma_{zth2} = 1/k_{th2}$. If the bunch length $\sigma_z \ll \sigma_{zth1}$ and $\sigma_z \ll \sigma_{zth2}$, the radiation fields reflected back from the chamber walls never reach the beam and thus have no actions on the beam. It also means that the beam never feels the fields reflected from the chamber walls. Consequently, chamber shielding can be neglected.

The simple geometrical analysis in Chapter 2 gives similar results as Eq. (4.10). A critical magnet length regarding to the width of the chamber was also found as follows

$$L_{th2} = 2\sqrt{Ra}. \tag{4.12}$$

From the viewpoint of impedance, instead of wake potential, L_{th2} is related to the CSR impedance as follows: If the magnet length $L_d \ll L_{th2}$, CSR impedance significantly differs from the parallel-plates model and transient effect, including both entrance and exit, should be important; If $L_d \approx L_{th2}$, paralel-plates model works well; If $L_d \gg L_{th2}$, CSR impedance spectrum becomes highly fluctuated and contains many narrow peaks. From the viewpoint of beam instability, the importance of side-wall reflections should be evaluated via comparing the bunch length with the path difference σ_{zth1}, as stated in the previous paragraph.

CSR fields generated in one dipole can propagate together with the bunch and enter the next dipole. In the next dipole, new CSR fields can interfere with the fields from the previous dipole. If such interference happens inside the variation of a bunch, the CSR effect on single-bunch instability can be enhanced. The geometrical analysis in Chapter 2 can be extended to discuss the multi-bend CSR interference. In principle, if the radiation fields reflecting back from the

side walls can reach the beam itself, such interference effect should be taken into account. A reliable way is to calculate the CSR impedance in a series of dipole magnets, and then apply the impedance to numerical simulations or instability analysis. The relevant discussions are to be presented in the next sections.

There are evidences on the effect of the side-wall reflection in the literature. The spectral intensity of synchrotron radiation, which is linearly proportional to the real part of CSR impedance, measured in the NSLS VUV ring [84, 132] contains pseudo-equidistant peaks. This spectrum is very similar to the CSR impedance in a long magnet as shown in Chapter 2. Similar fine structures were also observed in the Canadian Light Source (CLS) [133].

The deviations from the steady-state model require careful calculations of CSR impedance for a storage ring. If the impedances from vacuum components can compete with CSR or even dominate the total impedance, they also have to be counted in MWI simulations.

4.3 Code development for simulations of microwave instability

A code solving Vlasov-Fokker-Planck (VFP) was developed for purpose of simulating MWI including CSR. Basically Warnock and Elisson's work is followed [134] to solve the VFP equation numerically. The VFP equation including collective wake force is written as

$$\frac{\partial \psi}{\partial s} + \frac{\partial q}{\partial s} \cdot \frac{\partial \psi}{\partial q} + \frac{\partial p}{\partial s} \cdot \frac{\partial \psi}{\partial p} = \frac{2\beta}{c} \frac{\partial}{\partial p} \left[p\psi + \sigma_\delta^2 \frac{\partial \psi}{\partial p} \right], \tag{4.13}$$

where $\psi = \psi(q, p, s)$ is the probability density in the longitudinal phase space and is normalized as $\iint \psi(q, p, s) dp dq = 1$. The coordinate $q = z$ is the longitudinal coordinate and $p = \Delta p / p_0$ is the relative momentum deviation. The quantities σ_δ and β are the relative energy spread and the damping coefficient, respectively. The corresponding longitudinal distribution is calculated from $\psi(q, p, s)$ as

$$\lambda(q, s) = \int \psi(q, p, s) dp \tag{4.14}$$

and will be used in calculating the wake forces. The Hamiltonian's equations are

$$\frac{\partial q}{\partial s} = \frac{\omega_s \sigma_z}{c\sigma_\delta} \cdot p, \tag{4.15}$$

$$\frac{\partial p}{\partial s} = -\frac{\omega_s \sigma_\delta}{c\sigma_z} \cdot q - I_n \cdot F(q,s), \tag{4.16}$$

where $I_n = \dfrac{Ne^2}{E_0 C}$ and ω_s is the synchrotron frequency. The wake force is

$$F(q,s) = \int_{q'=-\infty}^{\infty} W_\parallel(q'-q)\lambda(q')dq', \tag{4.17}$$

where $W_\parallel$ is the longitudinal wake function and its unit is V/pC. The parameters N, C and E_0 are the bunch population, the circumference and the design energy of the storage ring, respectively.

4.3.1 Operator splitting

The technique of operator splitting [135, 136], or called time splitting, is widely used in solving partial differential equations (PDEs). To solve the VFP equation, Eq. (4.13) is re-written and the operators are split into three parts as follows

$$\frac{\partial \psi}{\partial s} = \mathcal{L}\psi = \left(\sum_{i=1}^{3} \mathcal{L}_i\right)\psi, \tag{4.18}$$

where

$$\mathcal{L}_1 = -\frac{\omega_s \sigma_z}{c\sigma_\delta} \cdot p \cdot \frac{\partial}{\partial q} + \frac{\omega_s \sigma_\delta}{c\sigma_z} \cdot q \cdot \frac{\partial}{\partial p}, \tag{4.19}$$

$$\mathcal{L}_2 = I_n \cdot F(q,s) \cdot \frac{\partial}{\partial p}, \tag{4.20}$$

$$\mathcal{L}_3 = \frac{2\beta}{c}\frac{\partial}{\partial p}\left[p + \sigma_\delta^2 \frac{\partial}{\partial p}\right]. \tag{4.21}$$

The operators $\mathcal{L}_1$ and $\mathcal{L}_2$ are called Liouville operators, and $\mathcal{L}_3$ is called Fokker-Planck operator. The Liouville operator is reversible and the Fokker-Planck operator is irreversible. Finite differencing Eq. (4.18) yields the solution on the $(n+1)$-th time step

$$\psi^{n+1} = e^{\Delta s \mathcal{L}}\psi^n. \tag{4.22}$$

The simple first-order splitting can be formulated as

$$e^{\Delta s\mathcal{L}} \approx e^{\Delta s\mathcal{L}_1} e^{\Delta s\mathcal{L}_2} e^{\Delta s\mathcal{L}_3}. \tag{4.23}$$

And high-order splitting instead of Eq. (4.23) can be applied to achieve better approximation. For example, the second-order symmetric splitting scheme can be adopted

$$e^{\Delta s(\mathcal{L}_1+\mathcal{L}_2)} \approx e^{\Delta s\mathcal{L}_1/2} e^{\Delta s\mathcal{L}_2} e^{\Delta s\mathcal{L}_1/2}. \tag{4.24}$$

To get better approximation, the one-turn map in the ring can be divided into k integration steps. This scheme can be formulated as

$$e^{C\mathcal{L}} \approx [e^{C\mathcal{L}_1/k} e^{C\mathcal{L}_2/k} e^{C\mathcal{L}_3/k}]^k. \tag{4.25}$$

4.3.2 Discrete operator

The discrete version of the Liouville operator is Frobenius-Perron operator. Let $\mathcal{F}_1$ and $\mathcal{F}_2$ are the Frobenius-Perron operators corresponding to $\mathcal{L}_1$ and $\mathcal{L}_2$, then the evolution of probability density corresponding to the reversible operators can be evaluated as

$$\psi^*(q,p) = \mathcal{F}_1\psi(q,p,n\Delta s) = \psi(\mathcal{R}^{-1}(q,p), n\Delta s), \tag{4.26}$$

$$\psi^{**}(q,p) = \mathcal{F}_2\psi^*(q,p) = \psi^*(\mathcal{K}^{-1}(q,p)), \tag{4.27}$$

where the rotation mapping $\mathcal{R}$ is

$$\begin{bmatrix} q' \\ p' \end{bmatrix} = \begin{bmatrix} \cos(\mu_s\Delta s/C) & \beta_z \sin(\mu_s\Delta s/C) \\ -\sin(\mu_s\Delta s/C)/\beta_z & \cos(\mu_s\Delta s/C) \end{bmatrix} \begin{bmatrix} q \\ p \end{bmatrix}, \tag{4.28}$$

and the kick mapping $\mathcal{K}$ is

$$\begin{bmatrix} q' \\ p' \end{bmatrix} = \begin{bmatrix} q \\ p - I_n F(q,s)\Delta s/C \end{bmatrix}. \tag{4.29}$$

Here μ_s is the synchrotron phase advance in one turn, and β_z is the equivalent beta function of synchrotron motion. For the Fokker-Planck operator, the exponentially fitting scheme (EFS) [137] is proposed for discretization

$$\begin{aligned} \frac{\psi_i^{n+1} - \psi_i^n}{\Delta s} = \frac{2\beta}{c}\psi_i^{n+1} + \frac{\beta p_i(\psi_{i+1}^{n+1} - \psi_{i-1}^{n+1})}{c\Delta p} + \\ \rho_i^{n+1}\frac{2\beta\sigma_\delta^2}{c}\frac{\psi_{i+1}^{n+1} - 2\psi_i^{n+1} + \psi_{i-1}^{n+1}}{\Delta p^2}, \end{aligned} \tag{4.30}$$

where

$$\rho_i^{n+1} = \frac{p_i \Delta p}{2\sigma_\delta^2} \coth \frac{p_i \Delta p}{2\sigma_\delta^2}. \tag{4.31}$$

As proved in Ref. [137], the EFS has the properties of: 1) being uniformly stable for all values of integration step Δs, damping coefficient β and mesh size Δp; 2) being free of numerical oscillation.

4.4 Microwave instability in the KEKB low energy ring

The KEKB B-factory [1] has operated for more than 10 years since its first commissioning from Dec. 1, 1998. In June 2009, the peak luminosity reached 2.11×10^{34} cm^{-2}s^{-1} with stored beam currents of 1.64/1.12A (LER/HER) due to crab crossing and off-momentum optics corrections. One of the merits of KEKB [138], which contributed to such high luminosity, was squeezing the vertical beta function at the interaction point (IP) to 0.59 cm. Correspondingly, the natural bunch length is around 4.6 mm. And at normal operating bunch current of 1.0 mA at LER, the measured bunch length is around 7 mm.

Since the beam-beam simulations showed that the crab crossing should boost the luminosity by a factor of 2 [139], the achieved peak luminosity in 2009 was still far from expectations. Besides chromatic coupling induced by lattice nonlinearity [140], microwave instability in the LER may be another potential obstacle for achieving higher luminosity at KEKB by way of increasing beam currents.

In 2008, Y. Cai *et al.* studied the microwave instability in the KEKB rings by using broadband resonator impedance models [113]. In that work, it was demonstrated that the models described the longitudinal single-bunch beam dynamics very well when comparing with experimental observations. As predicted by Cai's model, the threshold of microwave instability at LER of KEKB is around 0.5 mA, which is well lower than the operating current of 1.0 mA.

4.4.1 Quasi Green's function of wake potential

To study the longitudinal single-bunch instabilities, the ultra-short wake potentials of various vacuum components were calculated using GdfidL [141], which was installed on a cluster with 256 GB memory at KEK. As trade-off between the capability of the cluster and the interested frequency range, 0.5 mm bunch length was chosen for most vacuum components of KEKB LER.

Figure 4.2 shows the total geometrical wake potential of KEKB LER. The length of driving Gaussian bunch used in GdfidL is 0.5 mm. CSR is another important impedance source at KEKB LER. The bending radius of both normal dipoles and wigglers at KEKB LER are 15.87 m. This value is much smaller than the average radius of the ring. The calculated CSR wake potential of 0.5 mm bunch for dipoles are shown in Fig. 4.3. Interference between consecutive magnets was neglected since the drifts between them are quite long.

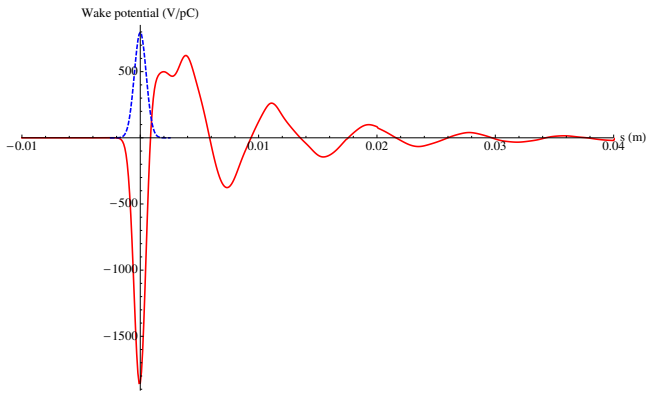

Figure 4.2: Calculated geometrical wake potentials of 0.5 mm bunch for KEKB LER. Blue dashed line: bunch profile; red solid line: wake potential.

From the short-bunch wake potentials, loss factors were also calculated using Gaussian bunch profile for different sources of impedance in the KEKB LER. The results are illustrated in Fig. 4.4. It is seen that RF cavities, movable masks, synchrotron radiation masks, resistive wall, and bellows contributed most of the loss factors at the normal operating bunch current with $\sigma_z = 7$ mm. It is noticed that CSR only causes remarkable power loss at bunch length shorter than 5 mm. The calculated loss factors were compared with experimental data [142]

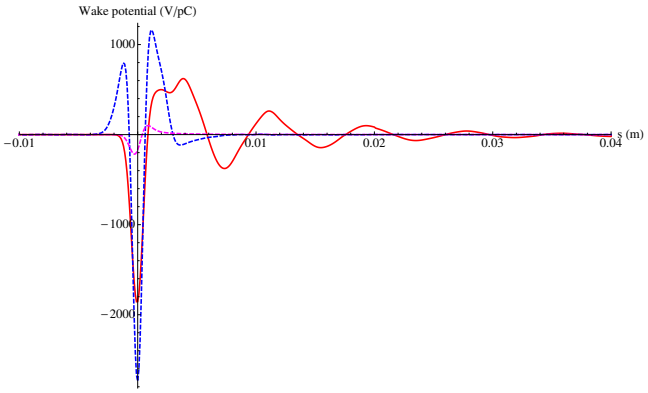

Figure 4.3: Calculated geometrical, resistive wall and CSR wake potentials of 0.5 mm bunch for KEKB LER. Red solid line: geometrical, magenta dashed line: resistive wall, blue dashed line: CSR.

and predictions based on the resonator model proposed in Ref. [113], as shown in Fig. 4.5. In the figure, a fitting function of

$$\kappa_{\parallel}(\sigma_z) = c_1 \sigma_z^{-c_2} \tag{4.32}$$

was used to fit the data obtained from three methods. The values of c_1 for measured data, calculated data and resonator model are 3600, 480, 3000 V/pC, respectively. The relevant values of c_2 are 2.67, 1.63 and 3.1 with the unit of mm for the bunch length. These parameters indicate that the three methods give quite different scaling laws for predicting the total loss factors of KEKB LER. It is noteworthy that the calculated loss factors are much smaller than measurements at bunch lengths short than 5 mm, but are remarkably higher at bunch lengths longer than 7 mm. It is still not well understood what kind of impedance sources make this discrepancy. Though the measurements show a hint of contribution from high-frequency impedance, CSR is not likely to be a strong candidate as seen from Fig. 4.4. On the other hand, the resonator model amazingly predicted the microwave instability in the KEKB LER, as stated in Ref. [113]. But it underestimates the loss factor at bunch lengths longer than 4 mm.

Experimental measurements showed that the longitudinal bunch profile deviates from Gaussian distribution in KEKB LER (see Figure 3 in Ref. [113]). It is not clear how the tilt in bunch profile will change the total loss factors. A

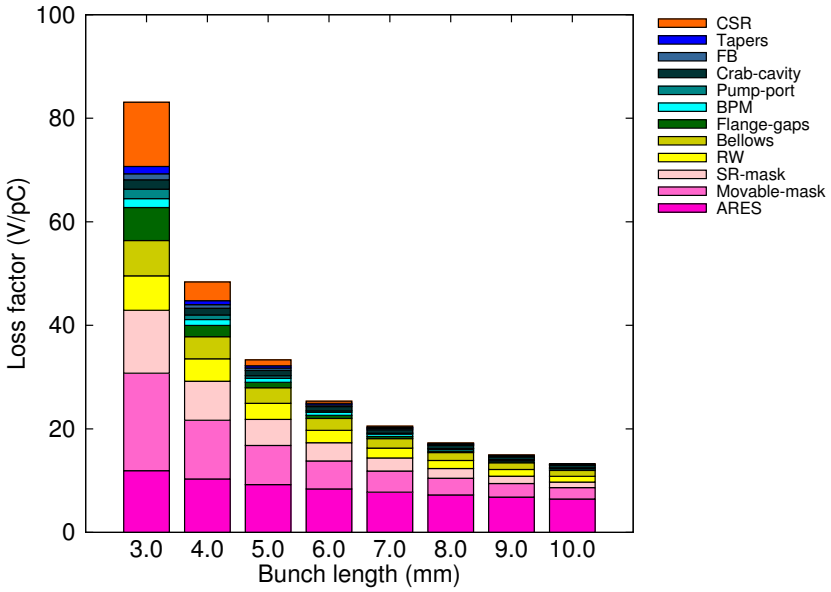

(a) Loss factor as a function of bunch length

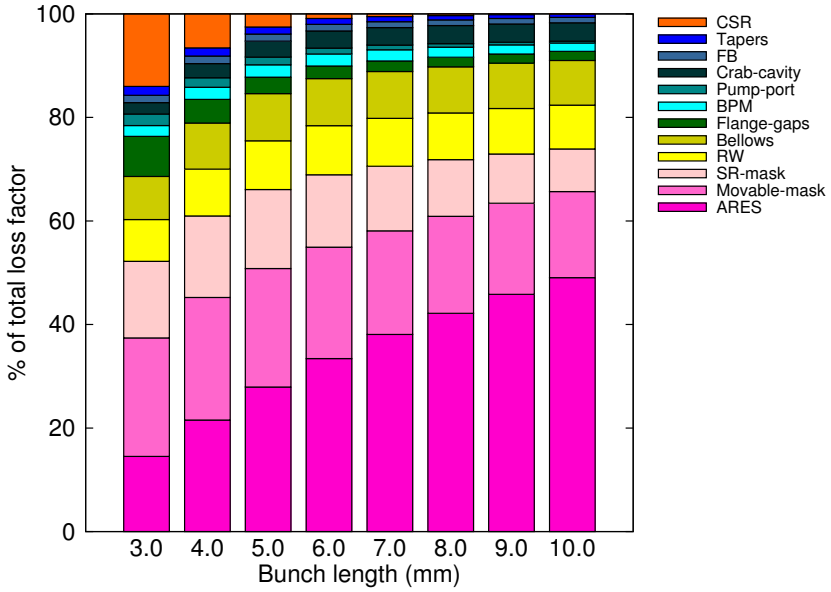

(b) Percentage distribution of the total loss factor

Figure 4.4: Calculated loss factor as a function of bunch length for KEKB LER. Gaussian bunch is assumed in calculating the loss factors.

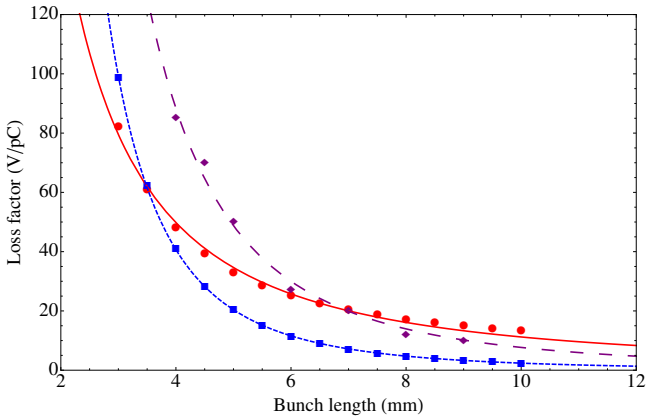

Figure 4.5: Comparison of calculated and measured loss factor as a function of bunch length for KEKB LER. Purple dots: measured data; red dots: calculated from numerical wakes; blue dots: calculated from resonator model. The lines are fitted curves as described in the text.

RF power balance method [143] may provide crosscheck to the measurements of loss factors. It was tried at KEKB rings but proved to be unsuccessful [144]. Due to noise in the data obtained from streak camera, it is hard to use the measured bunch profile for direct calculations of loss factors. Extracting the coupling impedance from measured bunch profile, which is possible by solving the inverse problem of Haïssinski equation [145, 146, 147], is one attempt but it is also very sensitive to the noise in the bunch profile [148].

4.4.2 Simulation results and comparison with measurements

Based on the algorithms described in Section 4.3, a code of VFP solver was developed and used in simulations of microwave instability at KEKB LER. The main parameters of KEKB LER are listed in Table 4.1.

Two methods were used to determine the bunch length of KEKB LER. As described in Ref. [149], one method developed by T. Ieiri was based on the beam spectrum. Suppose the longitudinal bunch profile has Gaussian distribution. The amplitude of the bunch spectrum has the form of Eq. (1.69). It is easily seen that measuring the amplitude at two frequencies under the condition of $k\sigma_z < 1$ should

Table 4.1: Main parameters of KEKB LER.

Parameter	**Value**	**Unit**
Circumference	3016.25	m
Beam energy	3.5	GeV
Bunch population	6.6	10^{10}
Natural bunch legnth	4.58	mm
Synchrotron tune	0.024	
Longitudinal damping time	2000	turn
Energy spread	7.27	10^{-4}

determine the bunch length. This method is applicable even there is tilt in the shape of the bunch profile due to potential-well distortion. As pointed out in Ref. [142], the bunch-length monitor needs to be calibrated due to the unequal gains in the two signal channels. One choice for such calibration is to set the bunch length extrapolated from the measured data to be equal to the natural bunch length of the ring at zero current. The measurements were conducted with the ring operating in the multi-bunch mode. The beam contained a train of well-separated bunches with equal intensity in each bunch. The multi-bunch mode has the merit of amplifying the signal detected by the bunch-length monitor. But only averaged bunch length could be measured.

Another method was based on streak camera, which works in the single-turn single-shot mode [150]. In principle, the streak camera provides the direct observation of the arbitrary longitudinal profile of a bunch. Using this method, the bunch-by-bunch shapes in a train can be measured simultaneously. The bunch-length monitor can also be calibrated by comparing with an independent measurement using streak camera.

For the KEKB LER, the results of bunch length as a function of bunch current given by the bunch-lenght monitor and streak camera are shown in the yellow and cyan curves of Fig. 4.6. It is seen that the two methods agree well at high bunch currents and have slight discrepancy at very low bunch currents. The discrepancy may be due to uncertainties of the measured signals for low currents.

Simulations of the bunch lengthening using different impedance models in the

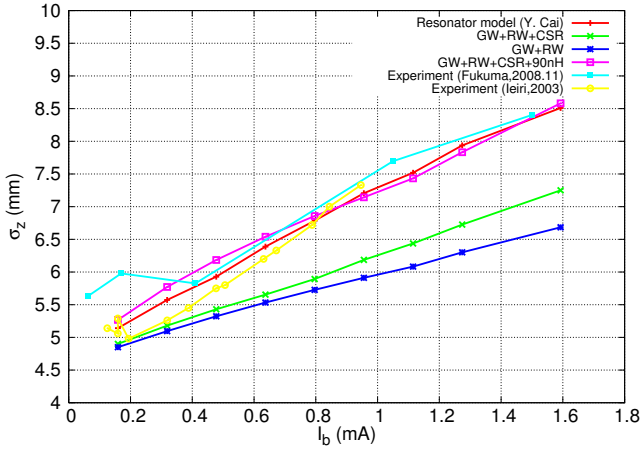

Figure 4.6: Bunch length as function of bunch current at KEKB LER. Red curve: prediction of the resonator model given in [113]; green curve: simulation with calculated geometrical, resistive wall and CSR wakes; blue curve: simulation with calculated geometrical and resistive wall wakes; magenta curve: simulation with calculated geometrical, resistive wall and CSR wakes plus a pure inductance of 90 nH; cyan curve: measurement by streak camera done in November, 2008; yellow curve: measurement by bunch-length monitor done in 2003.

KEKB LER are compared with the measurements in Fig. 4.6. It is seen that the numerical impedance model predicts much weaker bunch lengthening against measurements [142, 151]. The result of using geometrical and resistive wall wakes is represented in the blue curve. The result of adding CSR impedance to the previous model is given in the green curve. It turns out that the CSR impedance remarkably changes both the bunch lengthening and the MWI threshold (see Fig. 4.7) of the KEKB LER. According to Fig. 4.7, threshold current of MWI with CSR impedance is around 0.7 mA. Without CSR, the threshold is around 1.1 mA. A tentative conclusion can be drawn that CSR might be an important source to drive the microwave instability in the KEKB LER.

In order to get similar bunch lengthening, a pure inductance of around 90 nH was added in this numerical impedance model, as shown in the magenta curve in Fig. 4.6. It seems that the numerical impedance model only gives an inductance of around 26 nH, which is much smaller than the previous prediction in Refs. [113, 142], for the KEKB LER. On the contrary, when the pure inductance

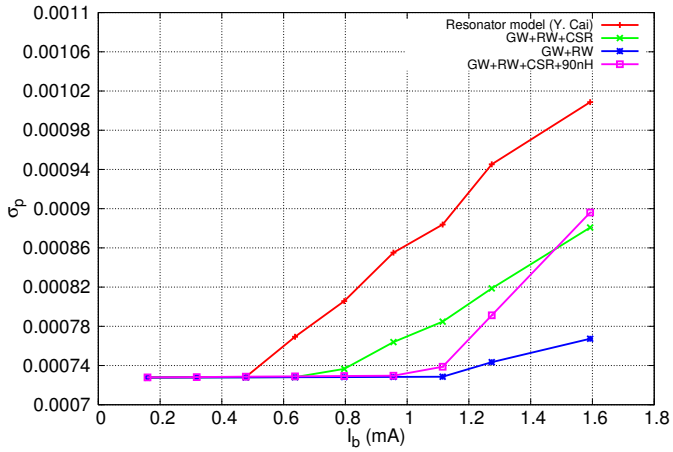

Figure 4.7: Energy spread as function of bunch crrent at KEKB LER.

was added, the threshold of MWI gets much higher as shown in Fig. 4.7. This disagreement indicates the same conclusion, as stated previously, that there are unknown impedance sources in the KEKB LER. It can also be inferred that a simple inductive impedance model is insufficient for explaining the MWI in the KEKB LER.

4.5 Microwave instability in the SuperKEKB positron damping ring

The CSR induced microwave instability in the SuperKEKB positron damping ring (DR) is examined in this section. The main machine parameters for two versions of designs are listed in Table 4.2.

For the SuperKEKB DR, the critical values discussed in Section 4.2 are tabulated in Table 4.3. The vacuum chamber dimensions are set as $a = b = 34$ mm. The bending radius of the magnet is 2.7 m. From the comparisons, the conclusions are:

1. Transient effect is not negligible in this damping ring.

2. From the fact that $\sigma_z \gg \sigma_{zth2}$, chamber shielding due to the upper- and lower-plates is significant. But it does not mean CSR instability is totally

Table 4.2: Main parameters used in tracking simulations for the SuperKEKB DR.

Parameter	**Ver. 1.140**	**Ver. 1.210**
Beam energy (GeV)	1	1.1
Circumference (m)	135.5	135.5
Bunch population (10^{10})	5	5
RF voltage (MV)	0.5	0.5
Bunch length (mm)	5.1	11.01
Energy spread (10^{-4})	5.44	5.5
Synchrotron tune	0.00788	0.0152
Damping rateturm (10^{-5})	7.28	8.25
Momentum compaction factor	0.00343	0.0141

suppressed as to be discussed soon.

3. From the facts that $L_b > L_{th2}$ and $\sigma_z > \sigma_{zth1}$, the side-wall (outer- and inner-wall) reflection should play a role in the CSR instability.

Table 4.3: Some critical parameters related to CSR for the SuperKEKB DR

	Ver. 1.140	Ver. 1.210
Magnet length (Design, m)	0.74	0.74
L_{th1} (m)	0.96	1.24
L_{th2} (m)	0.61	0.61
Bunch length (Design, mm)	5.1	11.01
σ_{zth1} (mm)	2.54	2.54
σ_{zth2} (mm)	0.84	0.84
χ	1.34	2.89

One may conclude from the fact $\sigma_z \gg \sigma_{zth2}$ that there should be no CSR instability in rings like SuperKEKB DR, because the radiation at wavelengths longer than $2\pi/k_{th2}$ have been well suppressed due to the chamber shielding. It should be pointed out that this conclusion is not correct and may be misleading. One may notice that there is no information about radiation wavelengths in Eqs. (4.3)

and (4.4), although parallel-plates shielding has been considered. This observation implies that the CSR instability is independent of radiation wavelength, but is only dependent on the beam parameters, which are fixed during the optics design. There always is CSR instability in an electron storage ring, provided that the bunch current is high enough. The criterion of $\sigma_z \gg \sigma_{zth2}$ assumed a smooth Gaussian bunch. Actually, microbunching may appear and coherent radiation can arise from the development of a microwave instability. Perturbations on a smooth long bunch may lead to bursts of coherent synchrotron radiation. Such bursts of CSR radiation have been reported in many machines. For detailed discussions, the reader is referred to Ref. [152].

4.5.1 Instability analysis based on broad-band CSR impedance

The two versions of the designed optics were also examined using the simple model developed for instability analysis of a coasting beam due to CSR [129]. Assuming positive momentum compaction, the instability is determined by the dispersion relation

$$1 = -i\frac{4\pi\epsilon_0 c\Lambda}{\sqrt{2\pi}} \cdot \frac{Z(k)}{kC} \int_{-\infty}^{\infty} dp \frac{pe^{-p^2/2}}{A+p} \tag{4.33}$$

where $\Lambda = n_b r_0/(\alpha_p \gamma \sigma_\delta^2)$ and $A = \Omega/(ck\alpha_p\sigma_\delta)$, and $Z(k)$ is the total CSR impedance in unit of Ohm. With Gaussian bunch n_b is equal to $N/(\sqrt{2\pi}\sigma_z)$. The beam is unstable if $\mathrm{Im}\{\Omega\} > 0$.

The integral in Eq. (4.33) can be replaced by

$$G(A) = \sqrt{2\pi} + i\pi A e^{-A^2/2}\{1 + \mathrm{erf}[iA/\sqrt{2}]\} \tag{4.34}$$

where erf[z] is error function. Using Eq. (4.34) and the CSR impedances given by the free space model, the parallel plates model, and numerical results for single dipole model, the dispersion relation Eq. (4.33) can be numerically solved. The thresholds as a function of the wavelength are depicted in Fig. 4.8. With respect to the design version 1.140, the Stupakov-Heifets (S-H) theory [129] infers that the damping ring is designed well above CSR instability threshold. For the version 1.210, the S-H theory predicts threshold higher than the maximum design goal.

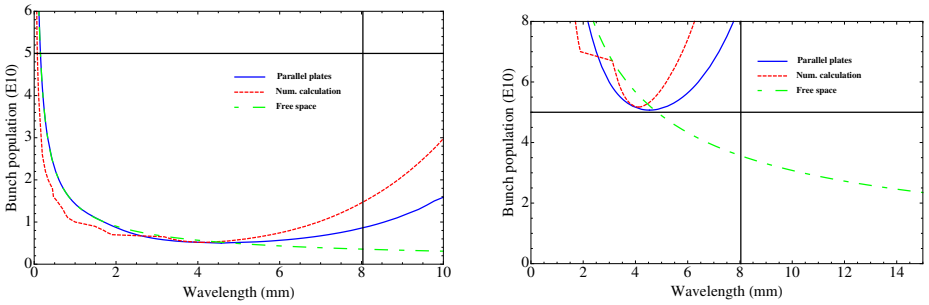

Figure 4.8: The CSR threshold as a function of the wavelength in SuperKEKB DR. The blue solid, red dashed and green dash-dotted lines are the results of CSR impedances given by parallel-plates model, numerical code, and free space model, respectively. The vertical straight line is the approximate shielding threshold due to parallel plates calculated by $2\sqrt{b^3/R}$. The horizontal straight line denotes the designed bunch population. The top and bottom figures correspond to the design version 1.140 and 1.210, respectively.

4.5.2 Instability analysis in the presence of narrow-band CSR impedance

As shown in Fig. 2.15, in a practical ring like SuperKEKB positron damping ring, CSR impedance including interference effect exhibits many narrow peaks. The peaks indicates field resonances generated by consecutive dipole magnets. There is concern that if such resonant CSR impedance is considered, beam will become unstable. The threshold of microwave instability due to CSR can be estimated by solving the dispersion relation [129, 153] or by solving Vlasov-Fokker-Planck equation [123]. For a simple instability analysis, one can apply the Keil-Schnell criterion [154] to a bunched beam [155]

$$\left|\frac{Z_\parallel}{n}\right| < F Z_0 \frac{\gamma \alpha_p \sigma_\delta^2 \sigma_z}{N r_e}, \tag{4.35}$$

where $Z_\parallel/n$ is the longitudinal impedance driving the instability, α_p is the momentum compaction factor, σ_δ is the relative energy spread, σ_z is the rms bunch length, N is the bunch population, r_e is the classical radius of electron. F is a form factor, for a Gaussian bunch, its value is taken as $F = \sqrt{\pi/2}$. $n = \omega/\omega_0$ is the harmonic and ω_0 is the revolution angular frequency. The above equation is also called Keil-Schnell-Boussard criterion. It is apparent that this criterion can

only provide a crude estimate of the instability threshold in a storage ring. As pointed out in Ref. [156], this criterion is only correct for a broad-band impedance wider than the frequency spectrum of the bunch. In principle, sharp resonances can also drive microwave instability [157]. But, as derived from Ref. [156], it is more appropriate to use a modified criterion as follows

$$\left|\frac{\sqrt{2\pi}k_0\sigma_z}{4}\frac{R_s}{Q}\right| < FZ_0\frac{\gamma\alpha_p\sigma_\delta^2\sigma_z}{Nr_e}, \tag{4.36}$$

to detect the instability threshold driven by sharp resonances, of which the frequency width is much narrower than that of bunch spectrum. In the above equation, $k_0 = \omega_0/c = 2\pi/C$ where C is the circumference of the storage ring. One should notice that Eq. (4.36) is written in the form that it has the same right side as Eq. (4.35). In the above equation, R_s is shunt impedance, and Q is quality factor. These parameters define the well-known resonator impedance model of

$$Z_\parallel(k) = \frac{R_s}{1 + iQ(k_r/k - k/k_r)}, \tag{4.37}$$

where k_r is the resonant frequency. For an impedance described by the above resonator model, Equation (4.35) applies if the impedance is much wider than that of the bunch spectrum, i.e. $k_r/Q \gg 1/\sigma_z$. On the contrary, at high quality factor of $Q \gg k_r\sigma_z$, Equation (4.36) applies. The wake function of a resonator impedance can also be calculated via Fourier transform

$$W_\parallel(z) = \frac{R_s c k_r}{Q\bar{k}_r}\frac{\partial}{\partial z}\Big[e^{-\alpha z}\sin(\bar{k}_r z)\Big]\theta(z), \tag{4.38}$$

where $\alpha = k_r/(2Q)$, $\bar{k}_r = \sqrt{k_r^2 - \alpha^2}$ and $\theta(z)$ is the Heaviside step function. When obtaining the above result, integration over k contains two singular poles at $k = -i\alpha \pm \bar{k}_r$. Therefore, complex contour integration should be performed. Because the two poles are always located in the lower half ω-plane for $Q > 0$, $W_\parallel(z)$ satisfies the causality condition and only has non-zero values for $z \geq 0$. One should also notice that Eq. (4.38) is valid for $Q > 0$. If $Q > 1/2$ and consequently $\bar{k}_r$ is real, Eq. (4.38) represents an underdamped solution. On the contrast, if $Q < 1/2$ and $\bar{k}_r$ is purely imaginary, it is an overdamped solution. When $Q = 1/2$, it is critically damped.

As an example, let us examine the resonant peak at $k_r = 1.264$ mm^{-1} in the CSR impedance shown in Fig. 2.15. This peak is chosen because it is the highest and exhibits relatively large width. As shown in the figure, R_s and Q should be functions of number of cells N_{cell}. This peak is fitted by using Eq. (4.37) and the corresponding parameters of R_s and Q are obtained. The results are plotted in Fig. 4.9. The figures show that the quality factor is almost a linear function of N_{cell}. And $R_s/Q/N_{cell}$ converges to a constant of around 132 Ω when $N_{cell} > 5$, this agrees with the shape of calculated wake potentials in Fig. 2.15(c). Larger values are observed at $N_{cell} < 5$ and it may be due to fitting errors. It is seen that for small number of cells, the CSR impedance spectrum becomes broad-band and neighboring resonant peaks overlap with each other.

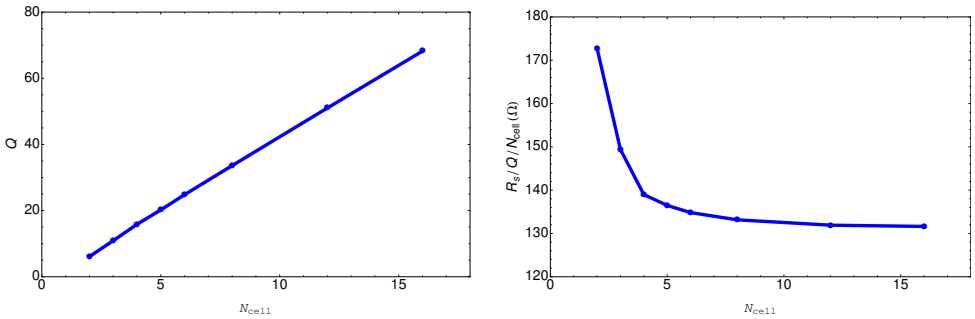

(a) Quality factor (b) Shunt impedance

Figure 4.9: Quality factor and shunt impedance as a function of number of cells at the resonant peak of $k_r = 1.264$ mm^{-1}. CSR impedances are calculated using different number of cells in one arc section of SuperKEKB positron damping ring dipole magnents. The shunt impedances have been normalized by the number of cells and quality factor.

Next the instability threshold is checked by using a set of machine parameters of SuperKEKB positron damping ring as shown in Ref. [86]. The parameters are listed as follows: $C = 135.5$ m, $\gamma = 2153$, $\alpha_p = 0.0141$, $\sigma_\delta = 5.5 \times 10^{-4}$, $\sigma_z = 7.74$ mm, $N = 5.0 \times 10^{10}$. Using these parameters, the right hand side of Eq. (4.36) is calculated to be 0.24 Ω.

The bunch length of $\sigma_z = 7.74$ mm corresponds to a critical bandwidth 0.13 mm^{-1} in unit of wavenumber. With $k_r = 1.264$ mm^{-1}, the critical qual-

ity factor is $Q_{th} = 9.8$. Comparing with Fig. 4.9(a), it is concluded that when $N_{cell} > 5$, Eq. (4.36) should be applied. Choosing $R_s/Q/N_{cell} = 130\ \Omega$ and taking into account the total number of cells $N_{cell} = 32$ for two arc sections, an impedance of $0.95\ \Omega$ is obtained for the left hand side of Eq. (4.36). This value is quite above $0.24\ \Omega$ which is defined by machine parameters. It implies that CSR may be of importance in the SuperKEKB positron damping ring. More careful studies via standard numerical simulations have also been performed [158] and general agreements were observed in estimations of the instability threshold.

5

Summary and outlook

This chapter summarizes the work presented in this thesis and discusses possible directions for future research.

5.1 Summary

5.1.1 Coherent synchrotron radiation

CSR has become a hot topic in accelerator physics over the last decade. It plays an important role in the single-bunch collective effects existing in both storage rings and linacs where high current and/or short bunch length are preferred. In storage rings, it may leads to bunch lengthening and even microwave instability. In linacs, it may cause unwanted emittance growth and microbunching in linac-based FEL light sources.

A numerical code, CSRZ, was developed based on the parabolic equation originally introduced in Ref. [26]. The numerical algorithms were described in detail. Numerous calculations of the longitudinal CSR impedance for a beam moving in an arbitrarily curved chamber have been performed. The CSRZ code was used to investigate the properties of CSR impedance of a single bending magnet as well as the profiles of the radiation field. It turns out that the magnet length, in addition to the chamber aspect ratio, may also play an important role in defining the profile of CSR impedance and wake function. For a long magnet, the shielding effect of the outer wall can be well understood using a simple geometric

model. With this code, the CSR interference in a series of bending magnets was straightforwardly approached. The calculations revealed that the interference might be significant in a practical small storage ring. In such a ring, the bending radius may be in the order of a few meters, and the CSR fields reflected by the outer wall may reach the bunch tail if the bunch length is in the order of a few millimeters. And the damping of the resistive wall on CSR field is negligible.

The case of a weak wiggler was also studied using the CSRZ code with a tiny approximation in modeling the vacuum chamber. With shielding of the chamber, the CWR impedance of a wiggler looks to be quite different from the free-space model. This observation was proved by an analytic approach.

The studies suggested that during evaluating the single-bunch instabilities due to CSR in a small storage ring or a damping ring dominated by wigglers, multi-bend CSR interference effect and chamber shielding in wigglers should be examined.

5.1.2 Coherent wiggler radiation

The eigenfunction method for calculating the fields generated by a moving point charge inside a rectangular waveguide has been investigated intensively. The method uses dyadic Green's functions in electromagnetic theory and is rigorous for the case of straight chamber. However, the electrodynamic system consists of relativistic electrons. Substantial alterations are required in order to make it applicable to calculate the charge self-fields. When Fourier transform is used to solve the system in frequency domain, the imaginary frequency has to be introduced as a mathematical tool to include the anomalous part of the charge self-fields. The theory of eigenfunction expansion method is re-derived and made suitable for calculating the full expressions for coherent wiggler radiation fields and impedance. The space-charge fields are expressed in terms of slow waves, and are related to imaginary poles in the complex frequency domain. Closed-form expressions for the electric fields of CWR have been derived. As a result, it is possible to obtain the CWR impedance for a point-charge in uniform and wiggling motions inside the rectangular waveguide.

Due to chamber shielding, the CWR impedance exhibits narrow peaks at frequencies satisfying the phase matching conditions, which were not seen in the theory for CWR in free space. The analytic work also provided excellent benchmarking to the CSRZ code.

5.1.3 Microwave instability

A code of Vlasov solver was developed for simulating the microwave instability in electron storage rings. Using this code, the single-bunch instability in the KEKB low energy ring was studied in detail. Different from Cai's resonator model [113], we started from careful calculations of impedances of the vacuum components, because an accurate impedance model is essential for studying the microwave instability in electron storage rings. Since there was a lack of convincing model for explanation of the MWI in the KEKB LER, the original scenario was to find out the unknown impedance sources in the KEKB LER.

CSR was taken into account in the impedance modeling for the KEKB LER. But, when comparing with beam observations, the numerical impedance model for KEKB LER still gave insufficient bunch lengthening and predicted higher threshold for MWI. CSR is not likely to be a strong candidate of the unknown impedance sources. The discrepancy between numerical model and measurements are around 90nH in case of bunch lengthening. A hypothesis for explaining this discrepancy is that a simple inductive impedance model is insufficient for explaining the MWI in the KEKB LER.

On the other hand, CSR was found to be a very important source of impedance driving microwave instability in the SuperKEKB positron damping ring. In modeling the CSR impedance in such a small ring, transient effect, chamber shielding and multi-bend interference have to be properly treated.

5.2 Directions for future work

For further explorations and refinements following the present work, two directions of research are identified and are presented below.

5.2.1 Numerical method based on the parabolic equation

The numerical method based on the parabolic equation is potentially applicable to a wide variety of studies, such as better understanding the measurements of coherent undulator radiation [159], the measured CSR pulses and spectra of THz radiations produced by electron storage rings [84, 132, 133, 160, 161, 162, 163, 164], the field dynamics and measurements of visible lights from edge radiation generated by the charged beam at the fringe region of bending magnets [165, 166, 167, 168, 169], etc.

As pointed out in Ref. [26], the parabolic equation method is also applicable to the case of chamber with varying cross section along the beam orbit. The resistive-wall boundary conditions can be applied easily, since the method works in the frequency domain. Besides calculating the geometrical impedance in structures such as collimators, the method can also treat the case of abrupt vacuum chamber near the IR ports for extracting THz radiation. As discussed in Ref. [133], such abruption of vacuum chamber may distort the CSR spectrum from that predicted by a smooth-chamber model.

By a slight modification of the parabolic equation, the method should be applicable to the studies of Cherenkov radiation for beam acceleration in dielectric wakefield accelerators (DWA) (for example of DWA, see Ref. [107]) or THz sources (for example of Cherenkov THz sources, see Ref. [170]).

The frequency-domain method is far from being investigated in simulations of the CSR fields. One possibility is to solve the electromagnetic system defined by Eqs. (2.22) and (2.23). In this case, challenges have to be faced to resolve the numerical instability during its implementation process.

5.2.2 Analytical method of eigenfunction expansion

The eigenfunction expansion method is a very general method and has various applications in solving partial differential equations. The eigenfunctions form a basis for the linear space of all solutions to the differential equation concerned. Typically, the eigenfunctions are chosen so as to form an orthonormal basis.

When the eigenfunction expansion method is applied to an electromagnetic system including relativistic charged sources, the substantial alteration is to ex-

tend the theory to include the sources's self-fields. The self-fields are near fields and are typically in the form of space-charge fields. The space-charge effect is a fundamental issue in particle accelerators in the low energy or ultra-short bunch regime.

Equation (3.68) represents the longitudinal impedance of a point charge. Possible simplification of its form may be seen as another step towards applications in simulating collective effects induced by the space-charge forces. Both Eq. (3.64) and Eq. (3.68) can be taken as Green's functions and used for calculating the electromagnetic fields and impedance of a bunched beam. The space-charge effects in proton accelerators can also be studied in the same framework.

Actually, the works presented in Refs. [58, 107] were successful applications of the eigenfunction expansion method to the problems of coherent radiations. In the present thesis work, the space-charge fields of a point charge are successfully expressed in terms of eigenfunctions of a rectangular waveguide. The same problem in a circular waveguide is also solvable using similar approach. In principle, the method is usable for any waveguide whose cross section is uniform. There is no necessity to restrict the curvature of the waveguide in the propagation direction. A similar statement has been made in Ref. [44] for calculation of CSR impedance in a toroidal pipe.

The resistive wall effect can be introduced as a perturbation to the eigenfunction expansion method. The application of time-dependent Green's functions (for example, see Ref. [171]) can also be investigated. Care should be taken not to exclude from consideration in the charge self-fields, which is always necessary in studying the collective effects of charged beams in accelerators.

References

[1] **KEKB B-factory Design Report**. KEK-Report- 95-7, KEK, 1995. 1, 119

[2] E. D. Courant and H. S. Snyder. **Theory of the Alternating-Gradient Synchrotron**. *Annals of Physics*, **281**(1-2):360 – 408, 2000. 2

[3] M. Sands. **THE PHYSICS OF ELECTRON STORAGE RINGS: AN INTRODUCTION**. SLAC-0121. 2

[4] S. Y. Lee. *Accelerator physics.* World Scientific, 2004. 2

[5] Helmut Wiedemann. *Particle Accelerator Physics; 3rd ed.* Springer, Berlin, 2007. 2, 16

[6] R. E. Collin. *Field Theory of Guided Waves.* IEEE, New York, 1991. 3, 5, 40

[7] L. Palumbo, V. G. Vaccaro, and M. Zobov. **Wake Fields and Impedance**. Technical Report LNF-94/041(P), September, 1994. "CAS - CERN Accelerator School: 5th Advanced Accelerator Physics Course". 6

[8] Alex Chao. *Lecture Notes on Topics in Accelerator Physics.* November 2002. SLAC-PUB-9574. 8

[9] Bruno W. Zotter and S. A. Kheifets. *Impedances and wakes in high-energy particle accelerators.* World Scientific, 1998. 9

[10] S. A. Heifets and S. A. Kheifets. **Coupling impedance in modern accelerators**. *Rev. Mod. Phys.*, **63**:631–673, Jul 1991. 10

[11] A. Chao. *Physics of Collective Beam Instabilities in High Energy Accelerators.* Wiley, 1993. 11, 87

[12] H. M. Nussenzveig. *Causality and Dispersion Relations*. Academic Press, New York and London, 1972. p. 27. 12

[13] L. D. Landau, E. M. Lifshitz, and L. P. Pitaevskii. *Electrodynamics of Continuous Media*. Pergamon, Oxford, 1984. 2nd edition. 12

[14] R. de L. Kronig. **On the Theory of Dispersion of X-Rays**. *J. Opt. Soc. Am.*, **12**(6):547–556, Jun 1926. 13

[15] H. A. Kramers. **La diffusion de la lumiere par les atomes**. *Atti Cong. Intern. Fisica*, **2**:545–557, 1927. 13

[16] F. R. Elder, A. M. Gurewitsch, R. V. Langmuir, and H. C. Pollock. **Radiation from Electrons in a Synchrotron**. *Phys. Rev.*, **71**:829–830, Jun 1947. 16

[17] Helmut Wiedemann. *Synchrotron radiation*. Advanced Texts in Physics. Springer, Berlin, 2003. 16

[18] A. Chao and W. Chou. *Reviews of accelerator science and technology*. Number v. 1 in Reviews of Accelerator Science and Technology. World Scientific, 2009. 16

[19] J. D. Jackson. *Classical Electrodynamics Third Edition*. Wiley, August 1998. 16, 19, 69

[20] J. Schwinger. **On radiation by Electrons in a Betatron**. Unpublished, see also M. A. Furman, LBNL-39088, 1945. 18, 20

[21] Olivier Vallée and Manuel Soares. *Airy Functions and Applications to Physics*. Imperial College Press, London, second edition, 2010. 19

[22] Julian Schwinger. **On the Classical Radiation of Accelerated Electrons**. *Phys. Rev.*, **75**:1912–1925, Jun 1949. 19

[23] A. Faltens and L. J. Laslett. **An Estimate of Limits to the Longitudinal Coupling Impedance**. BNL 20550, BNL, 1975. 20

[24] T. Nakazato, M. Oyamada, N. Niimura, S. Urasawa, O. Konno, A. Kagaya, R. Kato, T. Kamiyama, Y. Torizuka, T. Nanba, Y. Kondo, Y. Shibata, K. Ishi, T. Ohsaka, and M. Ikezawa. **Observation of coherent synchrotron radiation**. *Phys. Rev. Lett.*, **63**:1245–1248, Sep 1989. 21

[25] J. B. Murphy. **Coherent Synchrotron Radiation in Storage Rings**. *Beam Dynamics Newsletter*, **35**:20, 2004. 21

[26] T. Agoh and K. Yokoya. **Calculation of coherent synchrotron radiation using mesh**. *Phys. Rev. ST Accel. Beams*, **7**(5):054403, May 2004. 21, 23, 24, 27, 30, 31, 33, 34, 35, 41, 42, 43, 45, 46, 57, 133, 136

[27] K. Oide, T. Abe, K. Akai, Y. Funakoshi, T. Kageyama, H. Koiso, K. Ohmi, Y. Ohnishi, K. Shibata, Y. Suetsugu, and M. Tobiyama. **A Few Issues on the Upgrade of KEKB B-Factory**. In *Proceedings of the 2009 Particle Accelerator Conference*, page 23, Vancouver, BC, Canada, 2009. 21, 23, 27

[28] M. Masuzawa. **Next Generation B-Factories**. In *Proceedings of the 1st International Particle Accelerator Conference*, page 4764, Kyoto, Japan, 2010. 21

[29] R. Talman. *Accelerator x-ray sources*. Wiley-VCH, 2006. 21

[30] B. G. Shchinov, A. G. Bonch-Osmolovski, V. G. Makhankov, and V. N. Tsytovitch. **The Development of Radiation Instability**. *Plasma Physics*, **15**:211, 1973. 23, 111

[31] A. Faltens and L. J. Laslett. **Longitudinal Coupling Impedance of a Stationary Electron Ring in a Cylindrical Geometry**. *Part. Accel.*, **4**:151, 1973. 23, 24, 57

[32] S. A. Kheifets and Bruno W. Zotter. **Coherent synchrotron radiation, wake field and impedance**. Technical Report CERN-SL-95-43 AP, CERN, Geneva, Jun 1995. 23

[33] M. Borland. **elegant: A Flexible SDDS-Compliant Code for Accelerator Simulation**. Technical Report Argonne National Laboratory Advanced Photon Source Report No. LS-287, 2000. presented at ICAP 2000, Darmstadt, Germany. 23, 59

[34] A. Novokhatski. **Field dynamics of coherent synchrotron radiation using a direct numerical solution of Maxwell's equations**. *Phys. Rev. ST Accel. Beams*, **14**:060707, Jun 2011. 23

[35] G. Bassi, T. Agoh, M. Dohlus, L. Giannessi, R. Hajima, A. Kabel, T. Limberg, and M. Quattromini. **Overview of CSR codes**. *Nuclear Instruments and*

Methods in Physics Research Section A: Accelerators, Spectrometers, Detectors and Associated Equipment, **557**(1):189 – 204, 2006. Proceedings of the 32nd Advanced ICFA Beam Dynamics Workshop on Energy Recovering Linacs. 23

[36] M. Borland. **Simple method for particle tracking with coherent synchrotron radiation**. *Phys. Rev. ST Accel. Beams*, **4**:070701, Jul 2001. 23, 26

[37] Ji Qiang, Robert D. Ryne, Salman Habib, and Viktor Decyk. **An Object-Oriented Parallel Particle-in-Cell Code for Beam Dynamics Simulation in Linear Accelerators**. *Journal of Computational Physics*, **163**(2):434 – 451, 2000. 23

[38] J. Qiang, R. D. Ryne, M. Venturini, A. A. Zholents, and I. V. Pogorelov. **High resolution simulation of beam dynamics in electron linacs for x-ray free electron lasers**. *Phys. Rev. ST Accel. Beams*, **12**:100702, Oct 2009. 23

[39] Christopher Mayes and Georg Hoffstaetter. **Exact 1D model for coherent synchrotron radiation with shielding and bunch compression**. *Phys. Rev. ST Accel. Beams*, **12**(2):024401, Feb 2009. 23, 26

[40] David Sagan, Georg Hoffstaetter, Christopher Mayes, and Udom Sae-Ueng. **Extended one-dimensional method for coherent synchrotron radiation including shielding**. *Phys. Rev. ST Accel. Beams*, **12**(4):040703, Apr 2009. 23, 26, 49

[41] A. Novokhatski and M. Sullivan. **Algorithm for Computation of Electromagnetic Fields of an Accelerated Short Bunch inside a Rectangular Chamber**. In *Proceedings of the 1st International Particle Accelerator Conference*, page 1584, Kyoto, Japan, 2010. 23

[42] R. Warnock and J. Bergstrom. **CSR Fields From Using a Direct Numerical Solution of Maxwell's Equations**. In *Proceedings of the 2011 Particle Accelerator Conference*, page 784, New York, NY, USA, 2011. 23

[43] D. R. Gillingham and T. M. Antonsen. **Calculation of coherent synchrotron radiation in toroidal waveguides by paraxial wave equation**. *Phys. Rev. ST Accel. Beams*, **10**(5):054402, May 2007. 23, 27

[44] G. V. Stupakov and I. A. Kotelnikov. **Calculation of coherent synchrotron radiation impedance using the mode expansion method**. *Phys. Rev. ST Accel. Beams*, **12**(10):104401, Oct 2009. 23, 27, 33, 36, 39, 45, 46, 48, 137

[45] Gabriele Bassi, James A. Ellison, Klaus Heinemann, and Robert Warnock. **Microbunching instability in a chicane: Two-dimensional mean field treatment**. *Phys. Rev. ST Accel. Beams*, **12**:080704, Aug 2009. 23

[46] Gabriele Bassi, James A. Ellison, Klaus Heinemann, and Robert Warnock. **Transformation of phase space densities under the coordinate changes of accelerator physics**. *Phys. Rev. ST Accel. Beams*, **13**:104403, Oct 2010. 23

[47] Balša Terzić and Gabriele Bassi. **New density estimation methods for charged particle beams with applications to microbunching instability**. *Phys. Rev. ST Accel. Beams*, **14**:070701, Jul 2011. 23

[48] J.-L. Vay. **Noninvariance of Space- and Time-Scale Ranges under a Lorentz Transformation and the Implications for the Study of Relativistic Interactions**. *Phys. Rev. Lett.*, **98**:130405, Mar 2007. 23

[49] W. M. Fawley and J.-L. Vay. **Use of the Lorentz-Boosted Frame Transformation to Simulate Free-Electron Laser Amplifier Physics**. *AIP Conference Proceedings*, **1086**(1):346–350, 2009. 23

[50] W. M. Fawley and J. L. Vay. **Full Electromagnetic Simulation of Coherent Synchrotron Radiation via the Lorentz-Boosted Frame Approach**. In *Proceedings of the 1st International Particle Accelerator Conference*, page 1874, Kyoto, Japan, 2010. 23

[51] J.-L. Vay, C. G. R. Geddes, E. Cormier-Michel, and D. P. Grote. **Effects of hyperbolic rotation in Minkowski space on the modeling of plasma accelerators in a Lorentz boosted frame**. *Physics of Plasmas*, **18**(3):030701, 2011. 23

[52] M. Dohlus. **Modelling of Space Charge and CSR Effects in Bunch Compression Systems**. In *Proceedings of EPAC 2006*, page 1897, Edinburgh, Scotland, 2006. 23

[53] J. B. Murphy, S. Krinsky, and R. L. Gluckstern. **Longitudinal wakefield for an electron moving on a circular orbit**. *Part. Accel.*, **57**:9–64, 1997. 24

[54] John S. Nodvick and David S. Saxon. **Suppression of Coherent Radiation by Electrons in a Synchrotron**. *Phys. Rev.*, **96**:180–184, Oct 1954. 24

[55] King-Yuen Ng and Robert Warnock. **Reactive impedance of a smooth toroidal chamber below the resonance region**. *Phys. Rev. D*, **40**:231–243, Jul 1989. 24, 48

[56] K.-Y. Ng. **Resonant Impedance in a Toroidal Beam Pipe**. *Part. Accel.*, **25**:153, 1990. 24

[57] R. L. Warnock and P. Morton. **Fields Excited by a Beam in a Smooth Toroidal Chamber**. *Part. Accel.*, **25**:113, 1990. 24, 47

[58] Tomonori Agoh. **Steady fields of coherent synchrotron radiation in a rectangular pipe**. *Phys. Rev. ST Accel. Beams*, **12**(9):094402, Sep 2009. 24, 27, 33, 47, 48, 53, 57, 87, 99, 105, 108, 110, 115, 137

[59] E. L. Saldin, E. A. Schneidmiller, and M. V. Yurkov. **Klystron Instability of a Relativistic Electron Beam in a Bunch Compressor**. *Nucl. Instrum. Methods Phys. Res., Sect. A*, **490**:1, 2002. 24

[60] E. L. Saldin, E. A. Schneidmiller, and M. V. Yurkov. **On the coherent radiation of an electron bunch moving in an arc of a circle**. *Nuclear Instruments and Methods in Physics Research Section A: Accelerators, Spectrometers, Detectors and Associated Equipment*, **398**(2-3):373 – 394, 1997. 24, 25, 35

[61] G. Stupakov and P. Emma. **CSR Wake for a Short Magnet in Ultrarelativistic Limit**. In *Proceedings of EPAC 2002*, page 1479, Paris, Fance, 2002. see also LCLS-TN-01-12, December, 2001. 24, 26, 60

[62] Richard Talman. **Novel Relativistic Effect Important in Accelerators**. *Phys. Rev. Lett.*, **56**:1429–1432, Apr 1986. 25

[63] Y. S. Derbenev and V. D. Shiltsev. **Transverse Effects of Microbunch Radiative Interaction**. Technical Report SLAC-PUB-7181, also Fermilab-TM-1974, SLAC, 1996. 25

[64] Y. S. Derbenev, J. Rossbach, E. L. Saldin, and V. D. Shiltsev. **Microbunch Radiative Tail-Head Interaction**. Technical Report TESLA FEL-Report 1995-05, DESY, Hamburg, Germany, 1995. 25, 49, 50, 51, 111, 114

[65] Bruce E. Carlsten. **Calculation of the noninertial space-charge force and the coherent synchrotron radiation force for short electron bunches in circular motion using the retarded Green's function technique**. *Phys. Rev. E*, **54**:838–845, Jul 1996. 25

[66] M. Dohlus and T. Limberg. **Emittance growth due to wake fields on curved bunch trajectories**. *Nuclear Instruments and Methods in Physics Research Section A: Accelerators, Spectrometers, Detectors and Associated Equipment*, **393**(1-3):494 – 499, 1997. Free Electron Lasers 1996. 25

[67] R. Hajima. **Analysis of Emittance Growth and Complex Impedance for Coherent Synchrotron Radiation Shielded by Two Parallel Plate**. In *Proceedings of the 1998 International Computational Accelerator Physics Conference*, Monterey, California, 1998. 25

[68] Y. Shibata, T. Takahashi, K. Ishi, F. Arai, H. Mishiro, T. Ohsaka, M. Ikezawa, Y. Kondo, S. Urasawa, T. Nakazato, R. Kato, S. Niwano, and M. Oyamada. **Observation of interference between coherent synchrotron radiation from periodic bunches**. *Phys. Rev. A*, **44**:R3445–R3448, Sep 1991. 27

[69] L. Lewin, D. C. Chang, and E. F. Kuester. *Electromagnetic waves and curved structures*. IEE electromagnetic waves series. P. Peregrinus on behalf of the Institution of Electrical Engineers, 1977. 28

[70] A. Chao and M. Tigner. *Handbook of accelerator physics and engineering*. World Scientific, 1999. 3rd Printing. 29

[71] G. V. Stupakov and I. A. Kotelnikov. **Shielding and synchrotron radiation in toroidal waveguide**. *Phys. Rev. ST Accel. Beams*, **6**(3):034401, Mar 2003. 30, 33, 36, 47, 51

[72] K. Oide. **Issues on the Upgrade**. Talk presented to the 14th Accelerator KEKB Review Committee, KEK, 2009. 31

[73] K. Oide. **A calculation of CSR**. Talk at Mini CSR Workshop, KEK, nov 2010. 31, 49, 50

[74] M. Levy. *Parabolic equation methods for electromagnetic wave propagation*. IEE electromagnetic waves series. Institution of Electrical Engineers, 2000. 32

[75] Gennady Stupakov. **Using the parabolic equation for calculation of beam impedance**. *New Journal of Physics*, **8**(11):280, 2006. 32

[76] M. Bassetti and G. Erskine. **Closed Expression for the Electrical Field of a Two-Dimensional Gaussian charge**. Technical Report CERN-ISR-TH-80-06, CERN, 1980. 36

[77] Volker Ziemann. **Beyond Bassetti and Erskine: beam-beam deflections for non-Gaussian beams**. (SLAC-PUB-5582):7 p, Jun 1991. 37

[78] T. Agoh. *Dynamics of Coherent Synchrotron Radiation by Paraxial Approximation*. Ph.D. thesis, University of Tokyo, 2004. 37, 39, 42, 45

[79] R. Alves-Pires. **Conformal mapping for two dimensional electrostatic beam potential calculations**. Technical Report CERN-PS-87-66-AA, CERN, Geneva, 1987. 37

[80] W. H. Press. *Numerical recipes in Fortran 90: the art of parallel scientific computing*. FORTRAN Numerical Recipes. Cambridge University Press, 1996. 38

[81] Fenghua Zheng, Zhizhang Chen, and Jiazong Zhang. **Toward the development of a three-dimensional unconditionally stable finite-difference time-domain method**. *Microwave Theory and Techniques, IEEE Transactions on*, **48**(9):1550 –1558, sep 2000. 43

[82] F. Zheng and Z. Chen. **Numerical dispersion analysis of the unconditionally stable 3-D ADI-FDTD method**. *Microwave Theory and Techniques, IEEE Transactions on*, **49**(5):1006 –1009, may 2001. 43

[83] I. Ahmed, Eng-Kee Chua, Er-Ping Li, and Zhizhang Chen. **Development of the Three-Dimensional Unconditionally Stable LOD-FDTD Method**. *Antennas and Propagation, IEEE Transactions on*, **56**(11):3596 –3600, nov. 2008. 43

[84] G. L. Carr, S. L. Kramer, N. Jisrawi, L. Mihaly, and D. Talbayev. **Two-Beam Interference of Long Wavelength Synchrotron Radiation**. In *Proceedings of the 2001 Particle Accelerator Conference*, page 377, Chicago, USA, 2001. 49, 116, 136

[85] G. Stupakov, K. L. F. Bane, and I. Zagorodnov. **Optical approximation in the theory of geometric impedance**. *Phys. Rev. ST Accel. Beams*, **10**(5):054401, May 2007. 50

[86] M. Kikuchi, T. Abe, K. Egawa, H. Fukuma, K. Furukawa, N. Iida, H. Ikeda, T. Kamitani, K. Kanazawa, K. Ohmi, K. Oide, K. Shibata, M. Tawada, M. Tobiyama, and D. Zhou. **Design of Positron Damping Ring for SuperKEKB**. In *Proceedings of the 1st International Particle Accelerator Conference*, page 1641, Kyoto, Japan, 2010. 55, 131

[87] M. Kikuchi. **Reverse-bend FODO lattice applied to damping ring for SuperKEKB**. *Nucl. Instrum. Methods Phys. Res., Sect. A*, **556**(1):13, 2006. 55

[88] M. Shimada, K. Harada, Y. Kobayashi, T. Miyajima, N. Nakamura, and S. Sakanaka. **Approach to a Start-To-End Simulation of 2-Loop Compact Energy Recovery Linac**. In *Proceedings of the 2nd International Particle Accelerator Conference*, page 1909, San Sebastián, 2011. 57

[89] G. Stupakov and D. Zhou. **Longitudinal impedance due to coherent undulator radiation in a rectangular waveguide**. Technical Report KEK Preprint 2010-43, KEK, Tsukuba, 2010. see also SLAC-PUB-14332. 63, 65, 89

[90] Juhao Wu, Tor O. Raubenheimer, and Gennady V. Stupakov. **Calculation of the coherent synchrotron radiation impedance from a wiggler**. *Phys. Rev. ST Accel. Beams*, **6**(4):040701, Apr 2003. 66, 69

[91] Y. H. Chin. **Coherent Radiation in an Undulator**. LBL– 29981, LBL, 1990. 69, 77

[92] E. L. Saldin, E. A. Schneidmiller, and M. V. Yurkov. **Radiative interaction of electrons in a bunch moving in an undulator**. *Nuclear Instruments and Methods in Physics Research Section A: Accelerators, Spectrometers, Detectors and Associated Equipment*, **417**(1):158 – 168, 1998. 69

[93] Juhao Wu, G. V. Stupakov, T. O. Raubenheimer, and Zhirong Huang. **Impact of the wiggler coherent synchrotron radiation impedance on the beam instability and damping ring optimization**. *Phys. Rev. ST Accel. Beams*, **6**:104404, Oct 2003. 69

[94] H. Motz and M. Nakamura. **Radiation of an electron in an infinitely long waveguide**. *Annals of Physics*, **7**(1):84 – 131, 1959. 69, 74, 77, 78, 79

[95] Y. Rahmat-Samii. **On the Question of Computation of the Dyadic Green's Function at the Source Region in Waveguides and Cavities (Short Papers)**. *Microwave Theory and Techniques, IEEE Transactions on*, **23**(9):762 – 765, sep 1975. 69

[96] Hermann A. Haus and Mohammed N. Islam. **Synchrotron radiation of wiggled electron beam in rectangular waveguide**. *Journal of Applied Physics*, **54**(9):4784–4793, 1983. 69

[97] E. Sternbach. **Integral formulation for a waveguide FEL**. *Nuclear Instruments and Methods in Physics Research Section A: Accelerators, Spectrometers, Detectors and Associated Equipment*, **272**(1-2):323 – 325, 1988. 69

[98] G. Mishra, S.K. Chhotray, and K.P. Maheswari. **Undulator radiation in a parallel plate waveguide: Inclusion of off-axis motion and higher-order energy corrections**. *Nuclear Instruments and Methods in Physics Research Section A: Accelerators, Spectrometers, Detectors and Associated Equipment*, **416**(2-3):452 – 464, 1998. 69

[99] S. K. Chhotray and G. Mishra. **Analysis of longitudinal wiggler-undulator radiation in a parallel plate waveguide**. *Physics Letters A*, **268**(1-2):1 – 11, 2000. 69

[100] E. L. Saldin, E. A. Schneidmiller, and M. V. Yurkov. **Green's function of homogeneous overmoded waveguide with finite conductivity walls**. *Nuclear Instruments and Methods in Physics Research Section A: Accelerators, Spectrometers, Detectors and Associated Equipment*, **445**(1-3):40 – 44, 2000. 69

[101] Avner Amir, Ilario Boscolo, and Luis R. Elias. **Spontaneous emission in the waveguide free-electron laser**. *Phys. Rev. A*, **32**:2864–2878, Nov 1985. 69

[102] Gianluca Geloni, Evgeni Saldin, Evgeni Schneidmiller, and Mikhail Yurkov. **Longitudinal impedance and wake from XFEL undulators. Impact on current-enhanced SASE schemes**. *Nuclear Instruments and Methods in Physics Research Section A: Accelerators, Spectrometers, Detectors and Associated Equipment*, **583**(2-3):228 – 247, 2007. 69

[103] Gianluca Geloni, Evgeni Saldin, Evgeni Schneidmiller, and Mikhail Yurkov. **Undulator radiation in a waveguide**. *Nuclear Instruments and Methods in Physics Research Section A: Accelerators, Spectrometers, Detectors and Associated Equipment*, **584**(1):219 – 237, 2008. 69

[104] G. B. Arfken and H. J. Weber. *Mathematical methods for physicists*. Elsevier, 2005. 71, 72

[105] F. V. Hartemann. *High-Field Electrodynamics*. CRC Press, 2002. CRC series in pure and applied physics. 76

[106] Chen-To Tai. *Dyadic Green Functions in Electromagnetic Theory, Second Edition*, chapter 5. IEEE Press, Piscataway, NJ, 1994. 77

[107] Changbiao Wang and J. L. Hirshfield. **Theory for wakefields in a multizone dielectric lined waveguide**. *Phys. Rev. ST Accel. Beams*, **9**(3):031301, Mar 2006. 83, 84, 85, 87, 136, 137

[108] I. S. Gradshteyn, I. M. Ryzhik, and A. Jeffrey. *Table of integrals, series, and products*. Academic Press, 2000. 103

[109] Stephen Wolfram. *The Mathematica Book*. Wolfram Media, Incorporated, 5 edition, 2003. 107

[110] K. Oide and K. Yokoya. **Longitudinal Single-Bunch Instability in Electron Storage Rings**. KEK-preprint- 90-10, KEK, 1990. 111

[111] K. Oide. **Effects of the potential-well distortion on the longitudinal single-bunch instability**. *AIP Conference Proceedings*, **230**(1):266–275, 1991. 111

[112] N. Towne. **Longitudinal simulations and measurements of stretched bunches**. *Phys. Rev. ST Accel. Beams*, **4**:114401, Nov 2001. 111

[113] Yunhai Cai, J. Flanagan, H. Fukuma, Y. Funakoshi, T. Ieiri, K. Ohmi, K. Oide, Y. Suetsugu, and Jamal Rorie. **Potential-well distortion, microwave instability, and their effects with colliding beams at KEKB**. *Phys. Rev. ST Accel. Beams*, **12**(6):061002, Jun 2009. 111, 119, 121, 125, 135

[114] E. Ferlenghi. **Effect of the coherent radiation on the phase distribution of a relativistic bunch**. *Il Nuovo Cimento B (1965-1970)*, **48**:73–79, 1967. 10.1007/BF02712439. 111

[115] C. Pellegrini and Andrew M. Sessler. **Curvature effects and the shape of bunches in electron storage rings. oai:cds.cern.ch:296764**. Technical Report CERN-ISR-TH-67-40, CERN, Geneva, Aug 1967. 111

[116] A. G. Bonch-Osmolovskii and É. A. Perel'shtein. **Longitudinal instabilities in annular charged beams II. Radiative instability**. *Radiophysics and Quantum Electronics*, **13**:849–853, 1970. 10.1007/BF01031655. 111

[117] P. Goldreich and D. A. Keeley. **Coherent Synchrotron Radiation**. *Astrophysical Journal*, **170**:463–477, 1971. 111

[118] Bruce E. Carlsten and Tor O. Raubenheimer. **Emittance growth of bunched beams in bends**. *Phys. Rev. E*, **51**:1453–1470, Feb 1995. 111

[119] K. Bane, S. Krinsky, and J. B. Murphy. **Longitudinal potential well distortion due to the synchrotron radiation wakefield**. *AIP Conference Proceedings*, **367**(1):191–198, 1996. 111

[120] M. Venturini and R. Warnock. **Bursts of Coherent Synchrotron Radiation in Electron Storage Rings: A Dynamical Model**. *Phys. Rev. Lett.*, **89**:224802, Nov 2002. 111

[121] Marco Venturini, Robert Warnock, Ronald Ruth, and James A. Ellison. **Coherent synchrotron radiation and bunch stability in a compact storage ring**. *Phys. Rev. ST Accel. Beams*, **8**:014202, Jan 2005. 111

[122] Robert L. Warnock. **Study of bunch instabilities by the nonlinear Vlasov-FokkerPlanck equation**. *Nuclear Instruments and Methods in Physics Research Section A: Accelerators, Spectrometers, Detectors and Associated Equipment*, **561**(2):186 – 194, 2006. 111

[123] K. L. F. Bane, Y. Cai, and G. Stupakov. **Threshold studies of the microwave instability in electron storage rings**. *Phys. Rev. ST Accel. Beams*, **13**(10):104402, Oct 2010. 111, 129

[124] Yunhai Cai. **Linear theory of microwave instability in electron storage rings**. *Phys. Rev. ST Accel. Beams*, **14**:061002, Jun 2011. 111, 112

[125] G. Stupakov and R. Warnock. **Microbunch Instability Theory and Simulations**. *Beam Dynamics Newsletter*, **35**:39, 2004. 111

[126] M. Shimada, M. Katoh, M. Adachi, T. Tanikawa, S. Kimura, M. Hosaka, N. Yamamoto, Y. Takashima, and T. Takahashi. **Transverse-Longitudinal Coupling Effect in Laser Bunch Slicing**. *Phys. Rev. Lett.*, **103**:144802, Oct 2009. 111

[127] F. Zimmermann. **Estimates of CSR Instability Thresholds for Various Storage Rings**. Technical Report ATS-Note-2010-049 and CLIC-Note-861, CERN, December, 2010. 111

[128] Y. Cai. **Theory of Microwave Instability and Coherent Synchrotron Radiation in Electron Storage Rings**. In *Proceedings of the 2nd International Particle Accelerator Conference*, page 3774, San Sebastián, 2011. 111, 112, 113

[129] G. Stupakov and S. Heifets. **Beam instability and microbunching due to coherent synchrotron radiation**. *Phys. Rev. ST Accel. Beams*, **5**(5):054402, May 2002. 111, 112, 128, 129

[130] J. M. Byrd, W. P. Leemans, A. Loftsdottir, B. Marcelis, Michael C. Martin, W. R. McKinney, F. Sannibale, T. Scarvie, and C. Steier. **Observation of Broadband Self-Amplified Spontaneous Coherent Terahertz Synchrotron Radiation in a Storage Ring**. *Phys. Rev. Lett.*, **89**(22):224801, Nov 2002. 112

[131] F. Sannibale, J. M. Byrd, Á. Loftsdóttir, M. Venturini, M. Abo-Bakr, J. Feikes, K. Holldack, P. Kuske, G. Wüstefeld, H.-W. Hübers, and R. Warnock. **A Model Describing Stable Coherent Synchrotron Radiation in Storage Rings**. *Phys. Rev. Lett.*, **93**:094801, Aug 2004. 112

[132] G. L. Carr, S. L. Kramer, J. B. Murphy, R. P. S. M. Lobo, and D. B. Tanner. **Observation of coherent synchrotron radiation from the NSLS VUV ring**. *Nuclear Instruments and Methods in Physics Research Section A: Accelerators, Spectrometers, Detectors and Associated Equipment*, **463**(1-2):387 – 392, 2001. 116, 136

[133] R. Warnock and J. Bergstrom. **Coherent Radiation in Whispering Gallery Modes**. In *Proceedings of the 2011 Particle Accelerator Conference*, page 1710, New York, NY, USA, 2011. 116, 136

[134] Robert L. Warnock and James A. Ellison. **A general method for propagation of the phase space distribution, with application to the sawtooth instability**. 2000. SLAC-PUB-8404. 116

[135] S. I. Tzenov. *Contemporary Accelerator Physics*. World Scientific, Singapore, 2004. p. 217. 117

[136] W. Hundsdorfer and J.G. Verwer. *Numerical Solution of Time-Dependent Advection-Diffusion-Reaction Equations*. Springer–Verlag, Berllin, 2003. p. 325. 117

[137] D. J. Duffy. **A Critique of the Crank Nicolson Scheme Strengths and Weaknesses for Financial Instrument Pricing**. *Wilmott magazine*, July 2004. p. 68-76. 118, 119

[138] K. Oide. **KEKB B-Factory**. *Progress of Theoretical Physics*, **122**(1):69–80, 2009. 119

[139] K. Ohmi, M. Tawada, Y. Cai, S. Kamada, and J. Qiang. **Luminosity Limit due to the Beam-Beam Interactions With or Without Crossing Angle**. *Phys. Rev. ST Accel. Beams*, **7**:104401, 2004. 119

[140] D. Zhou, K. Ohmi, Y. Seimiya, Y. Ohnishi, A. Morita, and H. Koiso. **Simulations of beam-beam effect in the presence of general chromaticity**. *Phys. Rev. ST Accel. Beams*, **13**(2):021001, Feb 2010. 119

[141] http://www.gdfidl.de. 120

[142] T. Ieiri and H. Koiso. **Measurement of Longitudinal Impedance at KEKB**. In *Proc. of 14th Symposium on Accelerator Science and Technology*, page 443, KEK, Tsukuba, Japan, 2003. 120, 124, 125

[143] A. Novokhatski and M. Sullivan. **Loss Factor of the PEP-II Rings**. In proceedings of 11th European Particle Accelerator Conference (EPAC 08), Magazzini del Cotone, Genoa, Italy, 23-27 Jun 2008. 123

[144] D. Zhou. **Longitudinal Single-Bunch Instabilities in the LER of KEKB**. Talk at the Accelerator Physics Seminar, KEK, Jul. 23 2009. 123

[145] J. Haïssinski. **Exact Longitudinal Equilibrium Distribution of Stored Electrons in the Presence of Self-Fields**. *Il Nuovo Cimento*, **18B**(1):72–82, 1973. 123

[146] Yoshihiro Shobuda and Kohji Hirata. **The existence of a static solution for the Haissinski equation with purely inductive wake force**. *Part. Accel.*, **62**:165–177, 1999. 123

[147] Yoshihiro Shobuda and Kohji Hirata. **Proof of the existence and uniqueness of a solution for the Haissinski equation with a capacitive wake function**. *Phys. Rev. E*, **64**:067501, Nov 2001. 123

[148] Alex Chao, Private communication. 123

[149] T. Ieiri. **Measurement of Bunch Length Based on Beam Spectrum in the KEKB**. In *Proceedings of EPAC 2000*, page 1735, Vienna, Austria, 2000. 123

[150] H. Ikeda, J. W. Flanagan, H. Fukuma, T. Ieiri S. Hiramatsu, H. Koiso, T. Mimashi, and T. Mitsuhashi. **Negative Momentum Compaction at KEKB**. In *Proc. of Workshop on e^+e^- in the 1-2 GeV range: Physics and Accelerator Prospects*, Alghero (SS), Italy, September 2003. 124

[151] H. Fukuma, Private communication. 125

[152] G. Stupakov. **Theory and Observations of Microbunching Instability in Electron Machines**. In *Proceedings of the 2003 Particle Accelerator Conference*, page 102, Portland, Oregon, USA, 2003. 128

[153] S. Heifets and G. Stupakov. **Single-mode coherent synchrotron radiation instability**. *Phys. Rev. ST Accel. Beams*, **6**(6):064401, Jun 2003. 129

[154] E. Keil and W. Schnell. **Concerning longitudinal stability in the ISR**. Technical Report CERN Report No. CERN-ISR-TH-RF/69-48, CERN, Geneva, 1969. 129

[155] D. Boussard. **Observation of microwave longitudinal instability in the CPS**. Technical Report CERN Lab II/RF/Int./75-2, CERN, Geneva, 1975. 129

[156] K.-Y. Ng. **Microwave instability limits when driven by narrow resonances**. In R. Donalson and J. Marx, editors, *Proc. of 1986 Summer Study on Phys. of SSC*, page 590, 1986. 130

[157] J. E. Griffin and J. A. MacLachlan. **Direct Observation of Microwaves Excited in the Fermilab Beam Pipe by Very Narrow Bunches**. *IEEE Transactions on Nuclear Science*, **32**:2359, October 1985. 130

[158] H. Ikeda, T. Abe, M. Kikuchi, K. Oide, K. Shibata, M. Tobiyama, and D. Zhou. **Effect of Coherent Synchrotron Radiation at the SuperKEKB Damping Ring**. In *Proceedings of the 2nd International Particle Accelerator Conference*, page 3732, San Sebastián, 2011. 132

[159] Young Uk Jeong, Yoshiyuki Kawamura, Koichi Toyoda, Chang Hee Nam, and Sang Soo Lee. **Observation of coherent effect in undulator radiation**. *Phys. Rev. Lett.*, **68**:1140–1143, Feb 1992. 136

[160] H.-W. Hübers, A. Semenov, K. Holldack, U. Schade, G. Wüstefeld, and G. Gol'tsman. **Time domain analysis of coherent terahertz synchrotron radiation**. *Applied Physics Letters*, **87**(18):184103, 2005. 136

[161] J. M. Byrd, Z. Hao, M. C. Martin, D. S. Robin, F. Sannibale, R. W. Schoenlein, A. A. Zholents, and M. S. Zolotorev. **Tailored Terahertz Pulses from a Laser-Modulated Electron Beam**. *Phys. Rev. Lett.*, **96**:164801, Apr 2006. 136

[162] M. Klein, N. Hiller, A.-S. Mueller, K. G. Sonnad, and P. Tavares. **Analysis of THz spectra and bunch deformation caused by CSR at ANKA**. In *Proceedings of the 1st International Particle Accelerator Conference*, page 1925, Kyoto, Japan, 2010. 136

[163] N. Yamamoto, M. Shimada, M. Adachi, H. Zen, T. Tanikawa, Y. Taira, S. Kimura, M. Hosaka, Y. Takashima, T. Takahashi, and M. Katoh. **Ultrashort coherent terahertz radiation from ultra-short dips in electron bunches circulating in a storage ring**. *Nuclear Instruments and Methods in Physics Research Section A: Accelerators, Spectrometers, Detectors and Associated Equipment*, **637**(1, Supplement):S112 – S115, 2011. The International Workshop on Ultra-short Electron and Photon Beams: Techniques and Applications. 136

[164] Gianfelice Cinque, Mark Frogley, and Riccardo Bartolini. **Far-IR/THz spectral characterization of the coherent synchrotron radiation emission at diamond IR beamline B22**. *Rendiconti Lincei*, **22**:33–47, 2011. 136

[165] Nikolay Smolyakov, Hiroaki Yoshida, and Atsunari Hiraya. **Edge radiation and its potential to electron beam diagnostics at HiSOR**. *Nuclear Instruments and Methods in Physics Research Section A: Accelerators, Spectrometers, Detectors and Associated Equipment*, **448**(1-2):73 – 75, 2000. 136

[166] G. Andonian, A. Cook, M. Dunning, E. Hemsing, G. Marcus, A. Murokh, S. Reiche, D. Schiller, J. B. Rosenzweig, M. Babzien, K. Kusche, and V. Yakimenko. **Observation of coherent terahertz edge radiation from compressed electron beams**. *Phys. Rev. ST Accel. Beams*, **12**:030701, Mar 2009. 136

[167] Gianluca Geloni, Vitali Kocharyan, Evgeni Saldin, Evgeni Schneidmiller, and Mikhail Yurkov. **Theory of edge radiation. Part I: Foundations and basic applications**. *Nuclear Instruments and Methods in Physics Research Section A: Accelerators, Spectrometers, Detectors and Associated Equipment*, **605**(3):409 – 429, 2009. 136

[168] Gianluca Geloni, Vitali Kocharyan, Evgeni Saldin, Evgeni Schneidmiller, and Mikhail Yurkov. **Theory of edge radiation. Part II: Advanced applications**. *Nuclear Instruments and Methods in Physics Research Section A: Accelerators, Spectrometers, Detectors and Associated Equipment*, **607**(2):470 – 487, 2009. 136

[169] A.-S. Müller, I. Birkel, M. Fitterer, S. Hillenbrand, N. Hiller, A. Hofmann, E. Huttel, K. S. Ilin, V. Judin, M. Klein, S. Marsching, Y.-L. Mathis, P. Rieger, M. Siegel, N. Smale, K. G. Sonnad, P. F. Tavares, A. Semenov, and H.-W. Hübers. **Studies of Polarisaion of Coherent THz Edge Radiation at the ANKA Storage Ring**. In *Proceedings of the 1st International Particle Accelerator Conference*, page 2529, Kyoto, Japan, 2010. 136

[170] A. M. Cook. *Generation of Narrow-Band Terahertz Coherent Cherenkov Radiation in a Dielectric Wakefield Structure*. Ph.D. thesis, University of California, Los Angeles, 2009. 136

[171] A. H. Mohammadian. **Time-dependent dyadic Green's functions for rectangular and circular waveguides**. *Antennas and Propagation, IEEE Transactions on*, **36**(3):369 –375, Mar 1988. 137

Declaration

This thesis is a presentation of my original research work. Wherever contributions of others are involved, every effort is made to indicate this clearly, with due reference to the literature, and acknowledgement of collaborative research and discussions. The work was conducted from Oct. 2008 to Sep. 2011 under the supervision of Professor Kazuhito Ohmi, at the High Energy Accelerator Research Organization (KEK), Oho 1-1, Tsukuba, Japan.

Demin Zhou,